Beautiful Higgs Boson

Nicolas Morange

To cite this version:

Nicolas Morange. Beautiful Higgs Boson. Physics [physics]. Université Paris-Saclay, 2021. tel-03341303

HAL Id: tel-03341303
http://hal.in2p3.fr/tel-03341303
Submitted on 10 Sep 2021

Habilitation à diriger des recherches

Beautiful Higgs Boson

Habilitation à diriger des recherches de l'Université Paris-Saclay

Habilitation présentée et soutenue à Orsay le 9 juillet 2021, par

Nicolas MORANGE

Composition du jury:

Marie-Hélène Schune Directrice de recherche, CNRS/IJCLab	Présidente
Gustaaf Brooijmans Professeur, Université Columbia	Rapporteur
Pierre Savard Professeur, Universtié de Toronto	Rapporteur
Isabelle Wingerter-Seez Directrice de recherche, CNRS/CPPM	Rapporteuse
Gautier Hamel de Monchenault Directeur de recherche, CEA/IRFU	Examinateur
Laurent Vacavant Directeur de recherche, CNRS/IN2P3	Examinateur

Contents

Introduction

Higgs boson physics is one of the highlights of the physics programme at the Large hadron Collider (LHC) at CERN, that will remain for many years the only collider at which the electroweak symmetry breaking mechanism can be studied. It is therefore important to study this mechanism with the best precision possible, making the most out of the available data. This implies for the ATLAS and CMS collaborations a very wide portfolio of Higgs boson studies, in order to measure as many production modes and decay channels as possible and extract from there the most information on the Higgs boson properties and couplings.

One of the virtues of the Standard Model is its small number of parameters, so that once the Higgs boson mass was measured the theory became fully constrained. Each measurement concerning the Higgs boson is therefore a stringent consistency test of the Standard Model: all production cross-sections, branching ratios, and differential distributions can be predicted and compared to the measurements. Any deviation there would sign the presence of new physics beyond the Standard Model.

Being the heaviest particles with masses below half of that the the Higgs boson, b-quarks make up about 60% of the Higgs boson decays. The observation and the precise measurement of those decays are thus very important, not only as the only Higgs boson coupling to down-quark type accessible at the LHC, but also as a key term in the total width of the boson.

However, the hadronic final state consisting of two b-tagged jets makes the observation of these decays notoriously difficult at hadron colliders, where the main sensitivity comes from the search of associated production modes, in weak boson fusion, associated production with a top-quark pair, or associated production with a weak vector boson. The latter process actually dominates the sensitivity, being a good compromise of an acceptable cross-section and a decent signal-over-background ratio, thanks to the leptonic decays of the weak boson that reduce significantly the multijet backgrounds.

Following a mild evidence in this channel at the Tevatron, it has taken six years since the Higgs boson discovery in 2012 and the analysis of about 80 $\text{fb}^{-1}$of 13 TeV data for the ATLAS and CMS collaborations to each observe independently the b-quarks decays of the Higgs boson in 2018.

This document presents the analysis that led to the first observation of the Higgs boson decays to b-quarks and of the associated production of the Higgs boson with a weak vector boson (referred to as the *VH* process in the following) by the ATLAS experiment [1], followed by differential cross-section measurements of this process and their interpretation in an effective field theory framework [2]. Those measurements were made using about 30 $\text{fb}^{-1}$of data collected in the Run-1 and 80 $\text{fb}^{-1}$of data collected in the Run-2 of the LHC.

After the completion of my PhD in 2012, I began my involvement in this research topic with the analysis of the Run-1 data, initially thinking that it would be a 2-years project to obtain a first evidence of the Higgs decays to b-quarks. It actually took 5 years to get an evidence, one more to obtain an observation, and I kept participating in the analysis all this time. Setting aside a significant involvement in the ATLAS Liquid Argon Calorimeter upgrade projects, the search for the $VH(b\bar{b})$ process has therefore been my main research project since late 2012. This search has been a major topic of the physics interests of the LAL ATLAS group throughout Run-2, with the involvement of a number of colleagues (Jean-François Grivaz, Jean-Baptiste de Vivie, Marumi Kado, Luc Poggioli). I therefore had the opportunity to work with two post-docs (Camilla Maiani, then Arthur Chomont) and many PhD students: I shared the supervision of David Delgove, participated in the supervision of Charles Delporte, Yanhui Ma and Tasneem Saleem, and finally supervised the PhD of Konie Al Khoury.

The goal of this document is therefore not to simply repeat the description of the analysis as it is in the two publications mentioned above, but to put all aspects of the design of the analysis in perspective and try to justify with physics all decisions taken on the general design, on the selections, on the systematic uncertainties, and in the statistical analysis of the results. To that end, information not present in the publications but publicly available in the theses defended mostly at LAL will be used when appropriate.

The results of this analysis have been recently superceded by newer measurements in the $VH(b\bar{b})$ channel using the full Run-2 luminosity [3]. I decided to keep this document based on the 2018 analyses partly because the writing was started before the 2020 analysis became public, and mostly because all the reasoning that justify the design of the analysis stayed basically the same. Some of the major changes in the latest analysis will however be briefly discussed as they answer some of the limitations found in the 2018 analyses. The reader interested in the details of the analysis with the full Run-2 luminosity can refer to Konie Al Khoury's PhD thesis [4].

It is assumed that the reader is familiar with the LHC as a proton-proton collider with a center-of-mass energy of 13 TeV. In case of any doubt, one may consult [5]. The analysis described in this document is realized using data recorded with the ATLAS detector which is presented in details in [6]. For brevity no description is included in this document, and details on its conception are mentioned only when appropriate.

This document is structured as follows. Chapter 1 summarises briefly the phenomenology of the Higgs boson at the LHC, the main results obtained and their interpretations. The $VH(b\bar{b})$ process is described more thoroughly, with details given in particular on the uncertainties in the predictions of its differential distributions, and on the interpretation of its measurement in effective field theories. The chapter 2 describes in details the analysis of 80 $\text{fb}^{-1}$of Run-2 data, and attempts to motivate all choices made on the general design of the analysis, on the event selections, on the systematic uncertainties, and on the statistical analysis of the data. The combinations of these results with those of other analyses that led to the observation of the Higgs boson decays into b-quarks and of the VH production are presented in chapter 3, followed by the first differential measurements performed in the $VH(b\bar{b})$ channel and their interpretation in an effective Lagrangian. The conclusions and a discussion on the perspectives of this analysis are found in chapter 4.

Chapter 1

Phenomenology of the $VH(b\bar{b})$ process

The physics of the Higgs boson is discussed in details in numerous papers, for instance [7–12]. The aim of this chapter is therefore not to write another review, but to give the reader enough information to put the importance of the $VH(b\bar{b})$ process in perspective, as well as giving sufficient details on the $VH(b\bar{b})$ process itself to understand the analysis presented in the next chapters. Therefore, section 1.1 gives a brief reminder of the Higgs boson phenomenology at the LHC, focusing on its production modes and decay channels. In section 1.2 different frameworks are discussed, in which the Higgs boson measurements are interpreted. Section 1.3 describes the motivations for the search of the Higgs boson decays into b-quark pairs, and summarizes the searches conducted in the various production modes. Finally, section 1.4 is dedicated to the $VH(b\bar{b})$ process, with details on the prediction of its production and decay, of its differential distributions, and a description of an effective lagrangian framework that can be used to interpret the measurements in this channel.

1.1 The Higgs boson at the LHC

In the Standard Model (SM), the Higgs mechanism was first introduced by Brout and Englert [11], and Higgs [12] to realize the electroweak symmetry breaking and generate masses for the weak gauge bosons. The use of a complex scalar field, $SU(2)$ doublet, with the well-known 'Mexican hat' potential $V(\phi) = \mu^2|\phi|^2 + \lambda|\phi|^4$ is the simplest way to trigger spontaneous symmetry breaking: in the case of $\mu^2 < 0$ the Higgs field takes a vacuum expectation value

$$v = \sqrt{-\frac{\mu^2}{\lambda}} \neq 0. \tag{1.1}$$

The Higgs boson arises after symmetry breaking as the only degree of freedom of the scalar field left after the W and Z bosons have acquired mass. It is therefore a scalar boson (the only fundamental scalar in the SM !), CP-even. In addition to giving mass to the weak bosons, it also helps to keep the unitarity of the triple weak gauge couplings up to very high energies.

It is somehow a wonder that the electroweak symmetry breaking mechanism, which was introduced to solve the origin of mass in the gauge sector, can also give mass to the fermions by introducing the simple Yukawa terms, whose schematic form is:

$$\mathscr{L}_Y = -y_f\bar{\psi}\phi\psi + h.c. \tag{1.2}$$

The electroweak symmetry breaking where the Higgs field takes a v.e.v v therefore generates a mass term with $m_f = y_f v/\sqrt{2}$.

As a result, the Higgs boson couples at tree-level to all massive particles in the Standard Model, with an interaction term of $-i\frac{m_f}{v}$ for the fermions and $-ig^{\mu\nu}\frac{2m^2_{W/Z}}{v}$ for the W and Z bosons. It also couples to gluons and photons through loops. The consequence is an extremely rich phenomenology for Higgs boson studies at the LHC, both in terms of production modes and of decay channels.

The value of $v = 246\,\text{GeV}$ is known from G_F measurements [13]. Hence all Higgs couplings, and therefore all branching fractions and production cross-sections can be computed once the mass of the Higgs boson is known.

The mass has been measured to be $m_H = 125.09 \pm 0.21\,(\text{stat.}) \pm 0.11\,(\text{syst.})\,\text{GeV}$ from a combination of the measurements in the $ZZ^* \to 4\ell$ and $\gamma\gamma$ channels by ATLAS and CMS using the LHC Run-1 data [14]. Newer measurements using Run-2 data show compatible values: $m_H = 124.97 \pm 0.24\,\text{GeV}$ at ATLAS [15], $m_H = 125.38 \pm 0.14\,\text{GeV}$ at CMS [16]

The branching fractions for a mass of 125 GeV are shown in fig. 1.1. A few comments can be made on this figure. As shown previously, the partial widths to fermions are (at first order) proportional to the squared mass of the fermions. That explains the dominant role of $H \to b\bar{b}$ decays, followed by significant contributions of decays to pairs of τ leptons and c-quarks. Although $m_H < 2m_W$ and $m_H < 2m_Z$, the branching fractions to vector boson pairs are still significant, with typically one boson on-shell and the other one significantly off-shell. The partial width into gluons is significant despite appearing at one-loop level, due to the size of the coupling to top-quarks and to the strength of the QCD coupling constant.

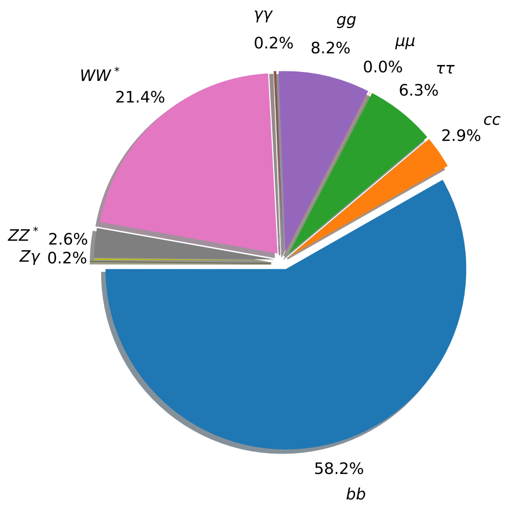

Figure 1.1: Main branching fractions for a Higgs boson at a mass of 125 GeV.

Decays into boson pairs ($\gamma\gamma$, ZZ^* and WW^*) have clear signatures, good signal-over-background (S/B) ratio and/or excellent invariant mass resolution, and as such were the first ones observed, using Run-1 data, at the time of the discovery of the Higgs boson [17–19]. The decays into τ pairs, that provided the first evidence of the Yukawa couplings, were first observed in the combination of the ATLAS and CMS results using the Run-1 dataset [20], then by each experiment separately in the Run-2 data [21, 22]. Finally the decays into b-quark pairs, which are the subject of this manuscript, were observed by ATLAS and CMS using up to 80 fb^{-1} of Run-2 data [1, 23]. Given its excellent invariant mass resolution and despite its very low branching ratio and S/B, the observation of the decays into muon pairs is expected at the HL-LHC ; the available data has still low sensitivity in this channel [24, 25]. Searches are also conducted in the $Z\gamma$ and $c\bar{c}$ final states, with low sensitivity so far [26–29].

The production modes of the Higgs boson at the LHC are illustrated on fig. 1.2. The main production channel is gluon fusion (ggF), that goes through a loop of heavy quarks (mostly top, with some contribution from b), and that was the first mode observed at the time of the Higgs boson discovery. The weak vector boson fusion (VBF) represents roughly 10% of the cross-section at $\sqrt{s} = 13$ TeV. It was observed first in the combination of the ATLAS and CMS results using the Run-1 dataset [20], then individually by each experiment using Run-2 data [30, 31]. The associated production with a vector boson (*VH*), or Higgsstrahlung, accounts for about 2% of the production for WH and 1% for ZH. It has been observed in the analysis of the Run-2 dataset by ATLAS [1] and CMS [31], and will be described in greater details in section 1.4 below. The top-associated production (ttH), which is the only direct probe of the coupling between the Higgs boson and the top quark, amounts to 1% of the cross-section, and has been observed during Run-2 [32, 33]. The small b-associated production is experimentally virtually impossible to separate from the gluon fusion process. The cross-sections of the production processes are shown as function of the center-of-mass energy in fig. 1.3.

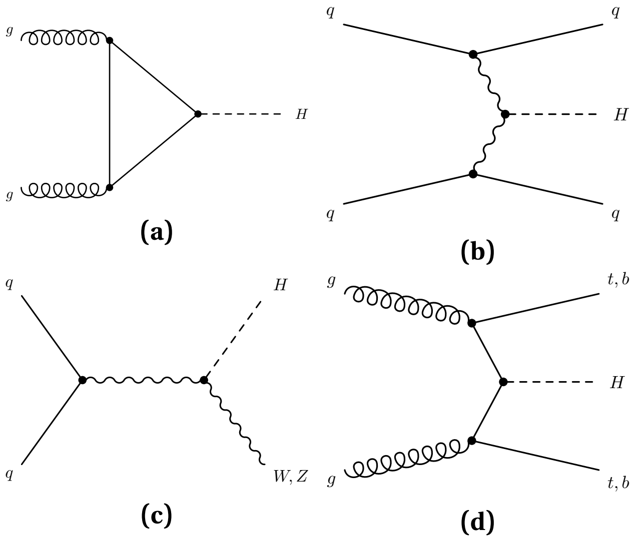

(a) (b) (c) (d)

Figure 1.2: Illustrative leading-order diagrams for the main Higgs boson production modes at the LHC. (a) gluon fusion. (b) vector boson fusion. (c) Higgsstrahlung. (d) top- or bottom-associated production.

The phenomenology of the Higgs boson at the LHC is by far not limited to its variety of production modes and decay channels. A lot of additional information can be extracted, but is of lesser relevance for the main topic of this document and only a few examples are therefore listed. The spin and parity of the Higgs boson have been investigated in the vector boson decay channels [34]: an excellent agreement with the SM prediction is observed, and alternative models are strongly excluded. The off-shell couplings of the Higgs boson can be studied in the ZZ^* decays [35], which under the assumption that on-shell and off-shell couplings are the same allows to set a constraint on the Higgs boson total width, with an observed limit at 95 % confidence level of 14.4 MeV. The simultaneous production of two Higgs bosons is actively searched for in many decay channels, such as $bb\gamma\gamma$ [36] or $bb\tau\tau$ [37], as it allows to set constraints on the Higgs self-coupling, with an exclusion at 95 % CL outside the interval $-2.3 < \lambda_{HHH}/\lambda_{HHH}^{\mathrm{SM}} < 10.3$ [38].

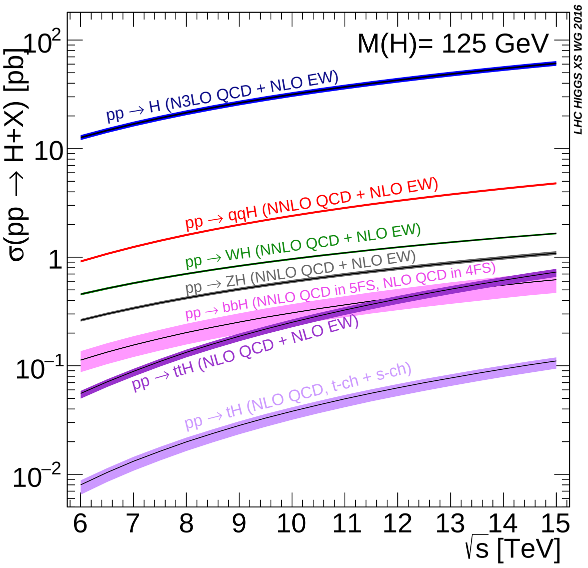

Figure 1.3: Cross-sections of the Higgs boson production processes at the LHC as function of the center-of-mass energy [10].

1.2 Interpretations of Higgs boson measurements

The observation of the Higgs boson has opened the exploration of a whole new sector of the SM Lagrangian. This justifies the searches and the measurements of the SM Higgs boson in as many channels as possible, and motivates searches for new particles, typically of high mass, where the Higgs boson is part of the decay chain, such as for instance heavy Higgses in two Higgs doublet models [39].

Restricting the discussion to SM Higgs measurements, the two main questions that should be answered are:

Are the Higgs boson couplings as in the Standard Model ? The answer to this question resides in the measurement of production cross-sections and branching fractions. A simple way to look for deviations from the SM is to parametrize each production mode and decay channel as function of the Higgs boson couplings, and introduce coupling modifiers (κ). For a given measurement of the Higgs boson in a production mode i and in some decay channel f, this yields:

$$\sigma_i.B_f = \kappa_i^2 \sigma_i^{\mathrm{SM}} \frac{\kappa_f^2 \Gamma_f^{\mathrm{SM}}}{\kappa_H^2 \Gamma_H^{\mathrm{SM}}}. \tag{1.3}$$

This equation makes the caveat of this parameterization clear: κ_H is always present, and as there is no direct measurement of the Higgs boson width possible at the LHC this set of equations will always be underconstrained. Additional hypotheses are therefore needed to make this couplings interpretation meaningful, the simplest one being that there are no Higgs boson decays to BSM particles, and that all invisible or undetected decays behave as in the SM.

This framework to interpret the combination of Higgs boson results is nonetheless very useful, as it allows to easily test the couplings under various hypotheses, for instance that of a universal coupling modifier for boson couplings, and of another one for fermion couplings, see fig. 1.4. No significant deviations from the SM have been observed so far.

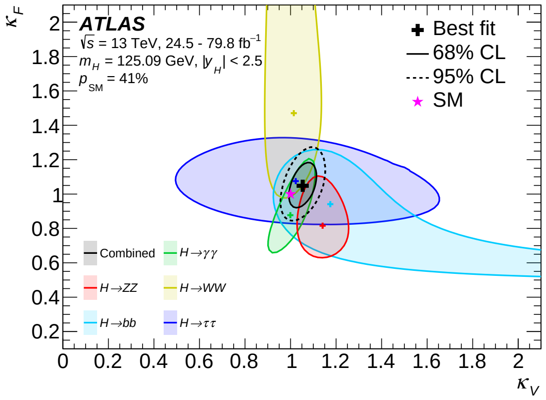

Figure 1.4: Negative log-likelihood contours at 68% and 95% CL in the (κ_V, κ_f) plane for the individual decay modes and their combination (in black) assuming the coupling strengths to fermions and vector bosons to be positive [30]

Another well-know result from this interpretation framework is the check of the scaling of the couplings versus the particles masses, as shown on fig. 1.5. Here also an excellent agreement with the Standard Model is observed.

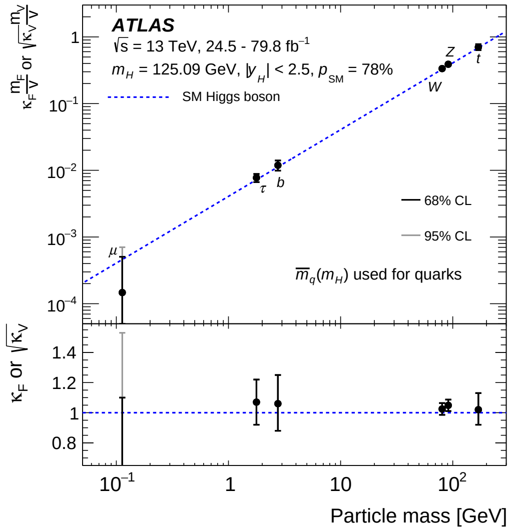

Figure 1.5: Reduced coupling-strength modifiers $\kappa_F m_F / v$ for fermions $(F = t, b, \tau, \mu)$ and $\sqrt{\kappa_V} m_V / v$ for weak gauge bosons $(V = W, Z)$ as a function of their masses m_F and m_V, respectively, and the vacuum expectation value of the Higgs field $v = 246\,\text{GeV}$. For κ_μ the light error bars indicate the 95% CL interval. The coupling modifiers κ_F and κ_V are measured assuming no BSM contributions to the Higgs boson decays, and the SM structure of loop processes such as $gg \rightarrow H$, $H \rightarrow \gamma\gamma$ and $H \rightarrow gg$ [30].

Is the structure of the Lagrangian the correct one ? The interpretation of Higgs boson measurements in terms of couplings measurements assumes that the only terms in the Lagrangian that involve the Higgs boson are the SM ones, and that only coupling constants may be different. However new physics may be present by additional terms in the Lagrangian, in a way that changes only minimally the effective coupling when measured inclusively, but that could induce much larger changes at higher scales.

As the Higgs boson decays always involve the scale $Q^2 = m_H^2$, it is expected that new physics contributions will mostly impact the production kinematics, that can involve much higher Q^2. It is therefore crucial to make differential measurements of the Higgs boson kinematics in the various production modes.

An agreement has been found between the ATLAS and CMS collaborations and the theory community to define common phase space regions to measure for each production mode. This Higgs Simplified Template Cross-Section (STXS) framework [10, 40] may not be optimal to probe for a particular BSM model, but it provides a relatively model-independent framework[1] in which the measurements performed independently in various decay channels and by ATLAS and CMS can be easily combined, and from which various BSM interpretations can be made. This common definition also facilitates the calculation of the uncertainties in the Higgs theory predictions, that have to be done only once.

The definitions of the truth-level categories are optimised for each production mode separately, and are the result of a compromise between sensitivity to new physics scenarios (using typically bins with large momentum), minimization of the dependence on theoretical uncertainties, and experimental sensitivity (available statistics and correlations between categories). The definitions are also meant to evolve, with several 'stages' of increased granularity that have been defined to match the increase of the experimental sensitivity with the accumulation of integrated luminosity. Changes in the categorization can also happen to reduce the model dependence in the extrapolation by adapting the truth level selections to better match the analysis phase space. The definitions for the associated production with a vector boson will be detailed in section 1.4.

A generic method to interpret the STXS measurements in terms of possible new physics is to use an effective Lagrangian approach [41]. Additional terms of the form $c_i^{(D)}\mathcal{O}_i^{(D)}/\Lambda^{(D-4)}$ are added to the SM Lagrangian, with Λ being the energy scale of new physics, $\mathcal{O}_i^{(D)}$ the dimension-D operators, and $c_i^{(D)}$ the corresponding (Wilson) coefficients. As this is an effective Lagrangian where the new physics is hidden above the scale Λ, the operators $\mathcal{O}^{(D)}$ act only on SM fields, and must be compatible with the SM gauge symmetries.

The counterpart of the genericity of this Effective Field Theory (EFT) approach is that the number of possible additional terms in the Lagrangian is gigantic. Strong hypotheses must be introduced in order to make this interpretation manageable. First, dimension 5 operators (and other odd-dimension operators in general) are rejected as they violate lepton or baryon number conservation. Dimension $D = 6$ is therefore the lowest order in the perturbative expansion, and higher-order terms are ignored as they are suppressed by powers of the large Λ scale (typically 1 TeV). Even counting only dimension-6 operators, there are about 2500 possibilities. The use of flavour symmetries allows to reduce this to a manageable number of 59 independent operators [42]. In practice, a given Higgs analysis is sensitive to only a few parameters, and some others are constrained from precision electroweak measurements. This makes it possible to perform meaningful EFT interpretations of STXS measurements of Higgs analyses. There are actually several different ways to parameterise the additional terms in the Lagrangian, leading to equivalent bases in the operators space that can be transformed into one another [43].

The Lagrangian for an effective field theory including dimension-6 operators can be written as

---

[1] ↑It is not as model-independent as a dedicated differential measurement as there are some phase-space extrapolations in the unfolding to the truth-level regions, that may be sizable for some analysis categories.

$\mathscr{L} = \mathscr{L}^{\text{SM}}_{(D=4)} + \mathscr{L}^{\text{EFT}}_{(D=6)}$. The calculation of the cross-section of a process $pp \to X$ becomes:

$$\begin{aligned}\sigma(pp \to X) &= \left|\mathscr{M}_{(D=4)}\right|^2 + 2\,\text{Re}\left(\mathscr{M}_{(D=4)}\mathscr{M}^*_{(D=6)}\right) + \left|\mathscr{M}_{(D=6)}\right|^2 \\ &\equiv \sigma_{\text{SM}} + \sigma_{\text{int}} + \sigma_{\text{BSM}}.\end{aligned} \tag{1.4}$$

Therefore the cross-section can be split into the usual SM term, an interference term of order $1/\Lambda^2$ and a BSM term of order $1/\Lambda^4$. The EFT interpretations at the lowest order thus only add the interference term to the SM contribution. The BSM term is of the same order in $1/\Lambda$ as the interference between SM terms and dimension-8 operators. However in practice, this interference with dimension-8 operators is usually small compared to the BSM term as defined in eq. (1.4). Both the interference term (linear in the Wilson coefficients) and the BSM term (quadratic in the Wilson coefficients) can therefore be used as leading terms in an interpretation of the STXS measurements as constraints on the Wilson coefficients.

1.3 Searching for Higgs boson decays into b-quarks

1.3.1 Motivations

The first physics motivation to observe and measure as precisely as possible the $H \to b\bar{b}$ decays at the LHC is trivial: the observation of these decays allow a direct measurement of the coupling of the b-quark to the Higgs boson, which is interesting in itself and helps verifying the linear relation between the Yukawa couplings and the fermion masses, as shown on fig. 1.5. Furthermore it is the only down-type quark whose coupling with the Higgs boson can be measured at the LHC.

This coupling is also of particular importance since it dominates the total Higgs boson width. As was discussed with eq. (1.3), in the absence of a direct measurement of the total Higgs boson width at the LHC, hypotheses have to be taken on it. The standard assumptions imply that barring BSM contributions to invisible and undetected decays, it is the sum of all visible partial widths. In such scenarios, the signal strength measured for $H \to b\bar{b}$ decays directly impacts all coupling modifiers. This can be seen in the combined Higgs results of the ATLAS Run-1 dataset [44], as shown in fig. 1.6. The signal strength for $H \to b\bar{b}$ was measured to be 0.63, while most others where measured to be larger than 1. When interpreted as coupling modifiers under the assumptions explained above, all of them were measured to be lower than 1 as a result of the low Γ_b in the denominator of eq. (1.3).

The understanding of the $H \to b\bar{b}$ decays is also particularly important for other search channels: due to its large branching fraction, it is the privileged channel to look for high mass resonances decaying into $H + X$ [39, 45, 46], and it is used in basically all searches for di-Higgs production, $bb\gamma\gamma$ [36], $bb\tau\tau$ [37], $bb\ell\nu\ell\nu$ [47], $bbbb$ [48].

1.3.2 Summary of the conducted searches

The search for $H \to b\bar{b}$ decays is notoriously difficult due to its hadronic final state. As shown in fig. 1.7, the Higgs boson production cross-section is about 7 orders of magnitude smaller than the b-jets pair production. An inclusive search of the dominant gluon fusion production is basically impossible, given that most of these events will not pass even the first level of hardware triggers. Associated production modes are therefore targeted, as they provide ways to improve the trigger efficiency, and generally increase the signal-over-background ratio.

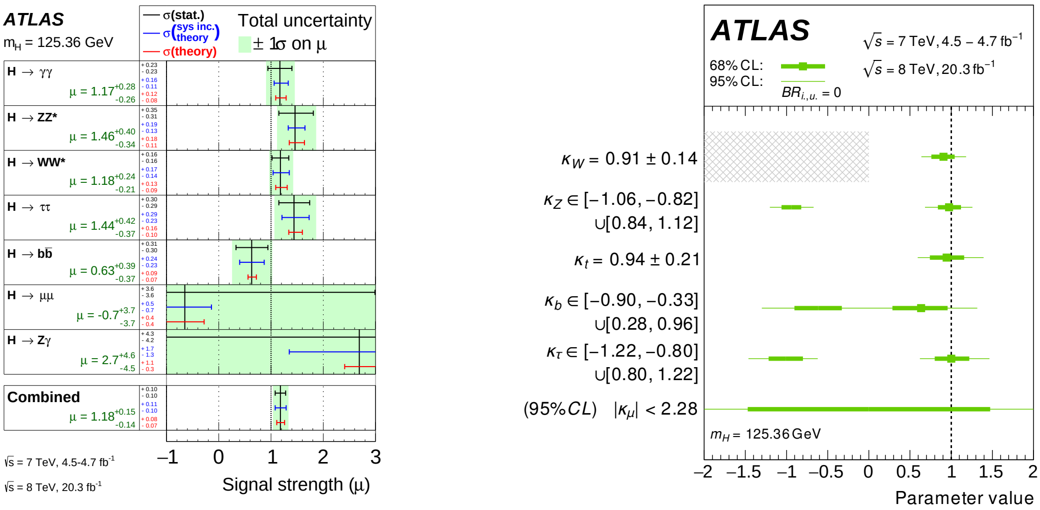

(a)

(b)

Figure 1.6: The observed signal strengths and uncertainties for different Higgs boson decay channels and their combination (a), and best-fit values for the coupling modifiers under the assumption that only SM particles are considered in loops and no invisible or undetected Higgs boson decays are allowed (b), as measured in the Run-1 dataset [44]. The weight of the partial width to b-quarks in the total Higgs width and the low signal strength measured for $H \to b\bar{b}$ explain why, from signal strengths all above 1 for $H \to \gamma\gamma$, $H \to WW^*$, $H \to ZZ^*$ and $H \to \tau\tau$, the coupling modifers to W, Z, t and τ all end up being lower than 1.

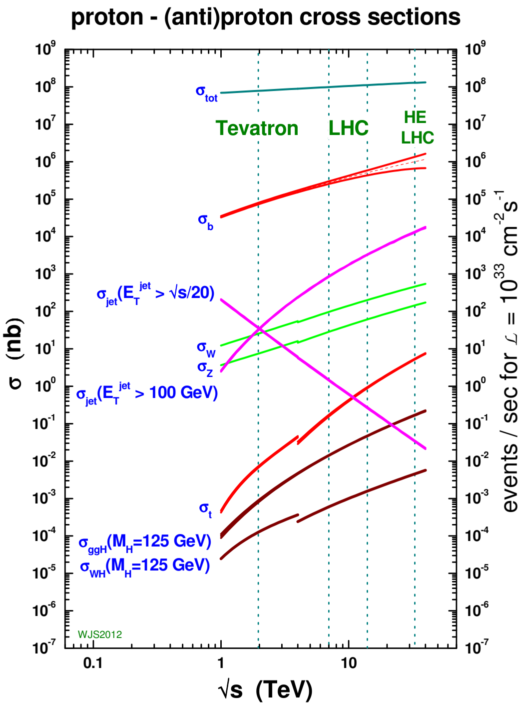

Figure 1.7: Cross-sections of a few typical processes as a function of center-of-mass energies for pp and $p\bar{p}$ collisions [49].

$H \to b\bar{b}$ decays were searched at the Tevatron, where $VH(b\bar{b})$ was the most sensitive channel for low mass Higgs. The combination of the measurements by the CDF and D0 collaborations yielded a global excess of 3.1 standard deviations in the full mass range, with a local significance of 2.8 standard deviations at 125 GeV [50].

At the LHC, these decays were searched in all production modes by the ATLAS and CMS collaborations.

The most sensitive channel is by far $VH(b\bar{b})$, where leptonic decays of the associated vector boson provide an efficient signature for triggering. The background is very significantly reduced compared to an inclusive search, as it is typically $V + b$-jets instead of inclusive b-jets production. This easily overcomes the reduced Higgs production cross-section and yields a more manageable signal-to-background ratio. The combination of the searches in the Run-1 data by the ATLAS and CMS collaborations [51, 52] showed an excess of 2.6 standard deviations, for 3.7 expected [20]. Analysing the 2015 and 2016 data, and combining with the Run-1 results, both collaborations reported an evidence for Higgs boson production and decay in this channel, with observed (expected) significances of 3.6 (4.0) and 3.8 (3.8) standard deviations, respectively [53, 54]. The analysis of the first three years of Run-2 data, which is presented in this manuscript for ATLAS, combined with the Run-1 searches, yielded observed (expected) excesses at the level of 4.9 (5.1) and 4.8 (4.9) standard deviations for ATLAS and CMS, respectively. Those results, once combined with the $H \to b\bar{b}$ searches in the other production modes, allowed to achieve the observation of the Higgs boson decays into b-quarks with signifiances of 5.4 standard deviations for ATLAS [1], and 5.6 standard deviations for CMS [23]. ATLAS then performed a differential measurement of the VH production mode in this channel in the STXS framework [2]. First results of the analysis of the full Run-2 datasets were released during the writing of this manuscript, showing that this channel is entering a phase of precision measurements [3], but will not be discussed further here.

The vector boson fusion production yields a quite typical topology, with forward jets and a rapidity gap in which only the Higgs boson decays centrally. This allows the setup of dedicated trigger chains for this hadronic final state, that achieve a decent efficiency for events with a large Higgs boson transverse momentum. It still remains a challenging final state, whose analysis is more difficult at 13 TeV than at 8 TeV, due to the larger increase of the gg-induced backgrounds cross-sections than the qq-induced signal cross-section, and is more difficult at higher pile-up levels due to raising trigger thresholds. Searches in the Run-1 data have been performed by the ATLAS and CMS collaborations, with observed (expected) limits of 4.4 (5.4) and 5.5 (2.5) times the Standard Model prediction, respectively [55, 56]. In the 2015 and 2016 datasets, ATLAS investigated in addition the exclusive final state with an additional photon. This additional requirement significantly suppresses the gluon-rich dominant $bbjj$ background, and improves the trigger efficiency, at the cost of a reduced cross-section. The sensitivity of this final state is similar to that of the inclusive VBF search, and their combination yielded an observed signifiance of 1.9 standard deviations, for 0.8 expected [57]. Significant progress in the inclusive VBF search have recently been achieved in the analysis of the full Run-2 dataset, including a better separation between signal and multijet backgrounds and a precise data-driven estimation of the $Z \to b\bar{b}$ background. Combined with the search in the photon-tagged channel [58] this yields an evidence at the level of 2.9 standard deviations for 2.9 expected [59].

The associated production with a top quark pair is characterized by very busy final states, with a minimum of four b-jets, and additional jets or leptons, depending on the decays of the W bosons coming from the top quarks. Semi-leptonic and di-leptonic decays are easy to trigger on, and the ratio between the signal and the dominant $t\bar{t}b\bar{b}$ background is reasonable (a few percent in the main signal regions). However the large combinatorics and the reconstruction inefficiencies in such busy events decrease the efficiency in the high purity analysis regions, and the analyses are significantly affected by the large uncertainties in the modelling of this difficult $t\bar{t}b\bar{b}$ background. Searches have been conducted by the ATLAS and CMS collaborations in the leptonic decay modes in the Run-1 and Run-2 data. Using the Run-1 dataset, the observed (expected) limits in the absence of signal were 3.4 (2.2) and 4.2 (3.3) times the Standard Model cross-section for ATLAS and CMS respectively [60, 61]. The analysis of about 36 $\text{fb}^{-1}$of Run-2 data yielded observed (expected) significances of 1.4 (1.6) and 1.6 (2.2) standard deviations for ATLAS and CMS respectively [62, 63]. A recent preliminary analysis of the complete Run-2 dataset by ATLAS led to an observed (expected) significance of 1.3 (3.0) standard deviations, and measured the first differential Higgs boson transverse momentum spectrum in this channel [64]. Searches were also conducted in the all-hadronic final state by the ATLAS collaboration using Run-1 data [65], and by the CMS collaboration in the data collected in 2016 [66], but resulted in much lower sensitivities.

In the past few years, the possibility for an inclusive search of the $H \to b\bar{b}$ decays was re-assessed in the very high momentum regime, where the Higgs boson is mostly recoiling against a jet from initial state radiation. A good trigger efficiency can be achieved at transverse momenta above several hundreds of GeV, where the Higgs boson decay products are all merged in a single large-R jet. The use of jet substructure techniques and the requirement of 2 b-tags inside the large-R jet allow to reduce the multijet background down to a level where some sensitivity to the Higgs boson is achievable. This search has been first performed by the CMS collaboration in the 2016 data, with an observed (expected) significance of 1.5 (0.7) standard deviations [67]. Using 136 $\text{fb}^{-1}$of data, a similar search in ATLAS observes a signal strength compatible with the Standard Model predictions, both inclusively and in p_{T}^{H} bins [68]. Even if the sensitivities are low, these searches probe a very unique momentum range for the Higgs boson (above ~ 500 GeV) where the impact of new physics could be significant, as shown for instance in the combined Higgs boson differential cross-section measurements performed by CMS [69].

In conclusion to this section, table 1.1 summarizes the results of the analyses performed on the Run-2 dataset described above. As it is usually the case, the sensitivities of the searches performed by the ATLAS and CMS collaborations are relatively close.

Table 1.1: Summary of the observed and expected sensitivities (in standard deviations) and measured signal strengths of the searches of $H \to b\bar{b}$ decays performed using Run-2 data. References are listed in the text.

Channel	Experiment	Luminosity (fb^{-1})	Observed signif. (s.d)	Expected signif. (s.d)	Signal strength
VH	ATLAS	80	4.9	4.3	$1.16^{+0.27}_{-0.15}$
	CMS	77	4.4	4.2	1.06 ± 0.26
VBF	ATLAS	126	2.9	2.9	$0.99^{+0.36}_{-0.34}$
ttH	ATLAS	139	1.3	3.0	$0.43^{+0.36}_{-0.33}$
	CMS	36	1.6	2.2	0.72 ± 0.45
$H + j$	ATLAS	136	-	-	1.1 ± 3.6
	CMS	36	1.5	0.7	$2.3^{+1.8}_{-1.6}$

1.4 The $VH(b\bar{b})$ process

1.4.1 Production and decay

The search for $H \to b\bar{b}$ decays in associated production with a vector boson is performed by looking for leptonic decays of the vector boson, as the sensitivity to hadronic decays would be much lower (starting with very low trigger efficiency). The cross-section of the *VH* production with leptonic dedays has been computed at next-to-next-to-leading order (NNLO) accuracy in QCD, and next-to-leading order (NLO) accuracy in EW [70–76]. The NLO EW corrections have sizable effects both on the inclusive and on the differential cross-section, in particular at large transverse momentum, as shown on fig. 1.8. These NLO EW distributions have been computed with HAWK [77, 78].

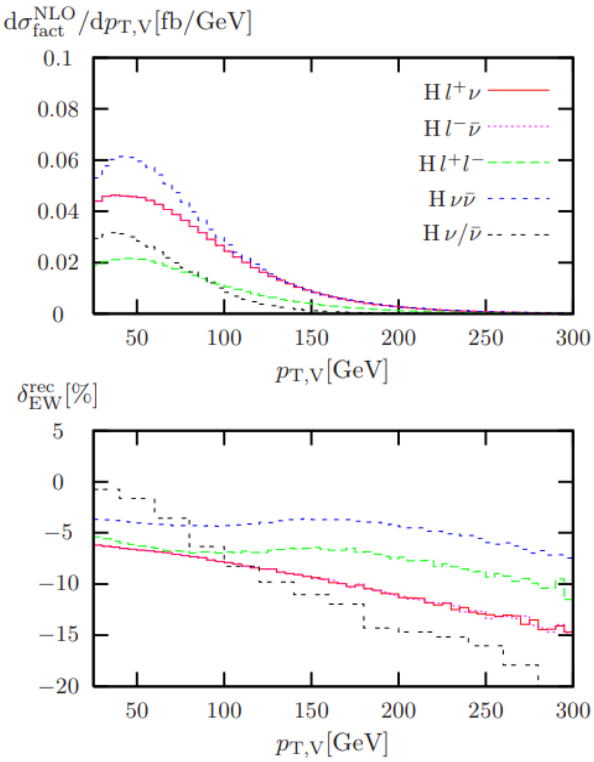

Figure 1.8: Differential cross-section of the Higgs boson transverse momentum (top) and contribution from the NLO EW corrections (bottom). The distributions are calculated for the Tevatron but their shapes are very similar at the LHC [77].

New types of diagrams with respect to the leading order Drell-Yan production open up at higher orders. A photon-induced contribution is responsible for an increase of the cross-section by about 5% for the WH process and much lower for ZH [79]. Of greater importance is the loop-induced $gg \to ZH$ contribution to the ZH process. Figure 1.9 shows representative diagrams of these processes. Even if it appears only at NNLO in QCD, the $gg \to ZH$ contribution accounts for about 10% of the ZH cross-section thanks to the large gluon luminosity at the LHC. Furthermore, the Higgs boson transverse momentum distribution peaks at a much larger value (about 150 GeV) than the Drell-Yan contribution, as shown in fig. 1.10, because of the large scales appearing in these diagrams. Since most of the sensitivity of the *VH*$(b\bar{b})$ analysis comes from such high transverse momentum regions, the contribution of the $gg \to ZH$ process in the analysis phase space is roughly 20%. Its cross-section has been calculated at NLO with next-to-leading log resummation (NLL) [80–84].

Table 1.2 summarizes the state-of-the-art of the predicted cross-sections of the *VH* processes as well as their uncertainties [7–9, 84]. The uncertainties are quite small, at the level of a couple of

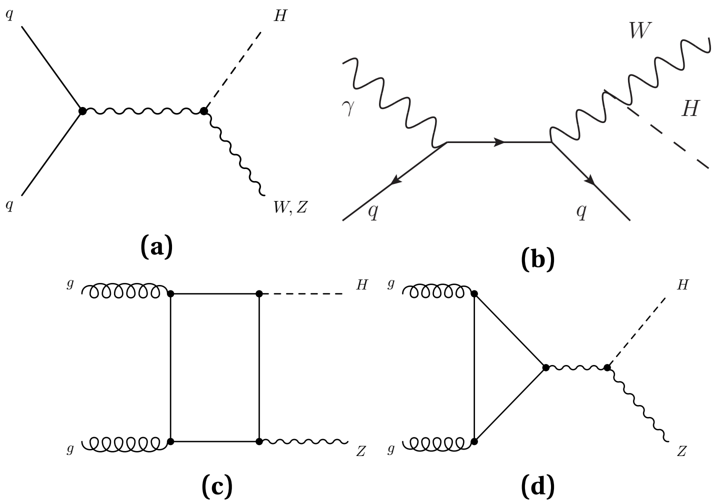

Figure 1.9: Leading-order diagram for the associated production with a vector boson in the quark-initiated Drell-Yan case (a), photon-induced contribution of WH (b), and leading diagrams for the gluon-gluon initial state that opens at higher order in QCD (NNLO) for the ZH production only (c) and (d).

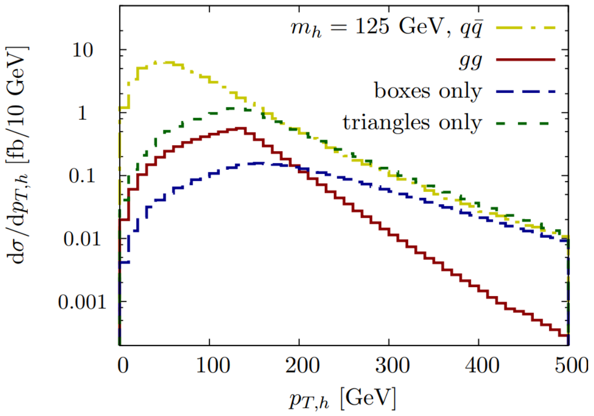

Figure 1.10: Higgs boson transverse momentum distribution for the different ZH production mechanisms [85].

percents, especially when compared to the uncertainties on the gluon-fusion production which are typically twice larger. This is of course due to the simplicity of the Higgsstrahlung diagrams: indeed the only important exception is the scale uncertainties on the loop-induced $gg \to ZH$ process, which amount to over 20%.

Table 1.2: Predicted cross-sections for the leptonic *VH* processes and their uncertainties at $\sqrt{s} = 13\,\text{TeV}$, for a Higgs boson mass of 125 GeV. The $Z \to \ell\ell$ and $W \to \ell\nu$ cross-sections are per lepton flavour, while the $Z \to \nu\nu$ cross-section stands for all neutrino flavours. The $gg \to ZH$ process is included in the $pp \to ZH$ calculations, but is also shown separately for reference as it dominates the scale uncertainties of the ZH process.

Process	σ [fb]	Uncertainties [%]		
		QCD Scale	PDF	α_S
$pp \to W^+H \to \ell^+\nu H$	94.3	$^{+0.5}_{-0.7}$	1.6	0.9
$pp \to W^-H \to \ell^-\nu H$	59.8	$^{+0.4}_{-0.7}$	1.8	0.8
$pp \to ZH \to \nu\nu H$	178	$^{+3.8}_{-3.1}$	1.3	0.9
$gg \to ZH \to \nu\nu H$	24.6	$^{+25.1}_{-18.9}$	1.8	1.6
$pp \to ZH \to \ell^+\ell^-H$	29.8	$^{+3.8}_{-3.1}$	1.3	0.9
$gg \to ZH \to \ell^+\ell^-H$	4.1	$^{+25.1}_{-18.9}$	1.8	1.6

The branching fraction into $b\bar{b}$ for a Higgs boson at a mass of 125 GeV is predicted to be 58.2% with a relative uncertainty of 1.7%, split almost evenly between higher order effects, uncertainties in the quark masses, and uncertainties in α_S.

The *VH*($b\bar{b}$) process has a relatively simple experimental topology, especially at large transverse momentum, with two b-jets recoiling against a leptonically-decaying vector boson. The latter can be reconstructed using a pair of charged leptons ($Z \to \ell\ell$ decays), high missing transverse energy ($Z \to \nu\nu$ decays), or a charged lepton and missing transverse energy ($W \to \ell\nu$ decays). Additional jets may of course be present, that blur a bit this picture.

1.4.2 Considerations for differential measurements

As discussed in section 1.2, the exploration of the Higgs sector of the Standard Model beyond the measurement of inclusive production modes and branching fractions relies on differential measurements mostly performed in the STXS framework. For the VH processes with leptonic decays of the vector bosons, the variable of interest chosen as a proxy to the Q^2 of the interaction is the transverse momentum of the vector boson p_T^V. This choice came naturally due to the good resolution on this variable (especially for $Z \to \ell\ell$ and $W \to \ell\nu$ decays) compared to the resolution on p_T^H, and mostly because it is that variable that the ATLAS and CMS analyses are using to categorise their events.

The *VH*($b\bar{b}$) analysis drives the sensitivity to the VH process compared to other decay channels such as $\gamma\gamma$ and $ZZ^* \to 3\ell$, and has the bulk of its sensitivity at a relatively large transverse momentum, roughly between 150 GeV and 300 GeV. This justifies the definition of the STXS categories as presented on fig. 1.11. The main separation is along p_T^V, with splits at 75, 150 and 250 GeV. There is a further split at 400 GeV, added as it can carry significant sensitivity to BSM effects, and as it is important to correctly estimate the signal uncertainties as will be discussed below. The number of additional jets in the events is obviously also a very important variable from an experimental perspective, and is taken into account in the STXS bins definition. In the simulation, these particle-level jets are built by clustering all generated stable particles ($c\tau > 10\,\text{mm}$) excluding the decay products of the Higgs boson as well as the neutrinos and charged leptons from the decays of the weak gauge boson, using the anti-k_t clustering algorithm [86] with a radius parameter $R = 0.4$. They are required to have a transverse momentum $p_\mathrm{T} > 30\,\mathrm{GeV}$. Finally, the $gg \to ZH$ process is separated from $qq \to ZH$ as the diagrams and therefore the theory uncertainties are quite different. However, there is no good experimental handle between these two processes once they are measured differentially in p_T^V and in number of additional jets. They will be therefore always merged together when performing the measurements. Not shown on the figure is a fiducial requirement $|y_H| \leq 2.5$ common to all production modes.

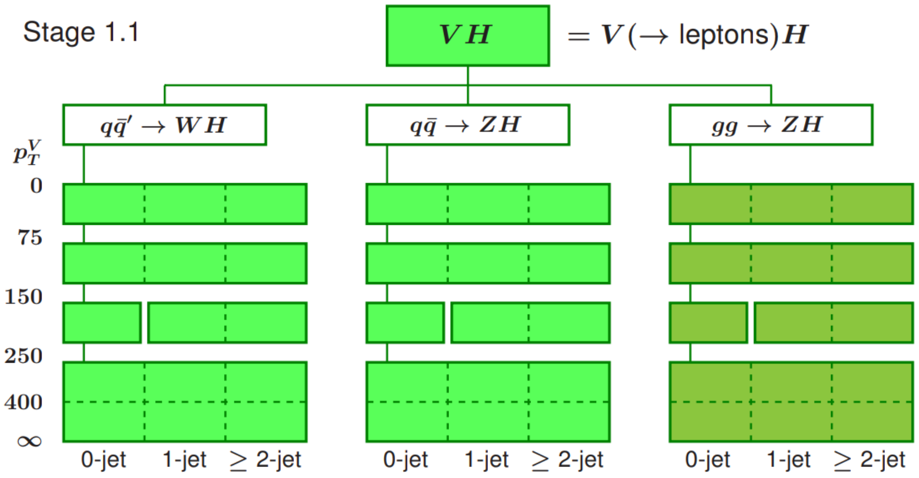

Figure 1.11: Definition of the STXS bins for the VH processes with leptonic decays of the vector bosons. Dashed boundaries indicate bins which should be split for an accurate estimation of the theory uncertainties in the predictions, but cannot be measured separately in the near future.

Some of the bin separations, represented as dashed lines on the figure, are not meant to be measured separately in the near future, but are important for an accurate estimation of the residual theory uncertainties in the acceptances of the bins. Indeed, even if the STXS categories are defined in close relation to the experimental categorization performed in the ATLAS and CMS analyses in order to reduce the dependence of the cross-section measurements on theoretical uncertainties in the SM prediction, this dependence cannot be completely eliminated in practice.

It manifests itself whenever the experimental acceptance of an analysis varies significantly inside a STXS category, or when an extrapolation is necessary between the phase space of the measurement and the STXS category. Cases where the experimental sensitivity is not enough to perform accurate measurements at the defined STXS granularity, and where sums of categories are then measured together, also lead to sizable residual theory uncertainties in the measurement.

This statement can be clarified by examining a simplified example of a single measurement performed over a sum of two STXS categories 1 and 2. One can write:

$$N_\mathrm{obs} = \mu(\epsilon_1\sigma_1 + \epsilon_2\sigma_2)\mathscr{L}, \tag{1.5}$$

where N_obs is the number of observed signal events, $\mathscr{L}$ the luminosity, μ the signal strength, $\sigma_{1,2}$ the predicted SM cross-sections in the categories 1 and 2, and $\epsilon_{1,2}$ the experimental acceptances, i.e the efficiencies for events from categories 1 or 2 to pass analysis selections. The measured cross-section for the sum of categories 1 and 2 is then obtained with:

$$\begin{aligned}\sigma_{\text{obs}} &= \mu(\sigma_1+\sigma_2)\\ &= \frac{N_{\text{obs}}}{\mathscr{L}}\left(\epsilon_1\frac{\sigma_1}{\sigma_1+\sigma_2}+\epsilon_2\frac{\sigma_2}{\sigma_1+\sigma_2}\right)^{-1}\\ &= \frac{N_{\text{obs}}}{\mathscr{L}}\left(\epsilon_1+(\epsilon_2-\epsilon_1)\frac{\sigma_2}{\sigma_1+\sigma_2}\right)^{-1}.\end{aligned} \tag{1.6}$$

The last form makes it clear that even without taking into account any extrapolation to a fiducial volume, as long as the experimental acceptances for the categories 1 and 2 are different ($\epsilon_2-\epsilon_1\neq 0$) the cross-section measurement is sensitive to any theory uncertainty in the truth acceptances for the categories ($\frac{\sigma_2}{\sigma_1+\sigma_2}$).

This reasoning applies to several aspects of the measurements in the STXS framework in the *VH*($b\bar{b}$) analysis. As will be shown in chapter 2, experimental categories are defined with 0-jet and 1-jet for WH, and with 0-jet and ≥ 1-jet for ZH. In the meantime, the experimental sensitivity allows to measure the cross-sections only inclusively in the number of jets. Therefore, the WH measurement has to be extrapolated to the ≥ 2-jet events, and both measurements have experimental acceptances that are different for 0-jet, 1-jet and ≥ 2-jet (for ZH) events. The uncertainties in the SM cross-sections in the jet STXS categories thus do matter in the measurement of the cross-section inclusive in the number of jets and have to be evaluated. Along p_{T}^{V}, the experimental selections at 75 GeV or 150 GeV match the STXS boundaries. However, the acceptances of the STXS categories in the experimental $p_{\mathrm{T}}^{V} > 150\,\text{GeV}$ region are quite different. In particular, b-jets from Higgs decays in signal events with p_{T}^{V} >400 GeV tend to be very close-by (boosted topology), resulting in a decreased experimental acceptance as two resolved b-jets are required. In this case as well, it is crucial that theory uncertainties in the signal acceptances are well defined.

The evaluation of these uncertainties for the VH process is described in detail in [87]. In addition to the overall cross-section uncertainties that have been presented in table 1.2, uncertainties are defined on the STXS categories in the form of migration systematics, that change yields in categories while preserving the overall normalization. The evaluations are performed with a sample generated using the POWHEG v2 generator with the `MiNLO` (Multiscale Improved NLO) procedure [88], interfaced to the PYTHIA 8 MC generator [89] applying the AZNLO tune [90] for the Drell-Yan processes. For the $gg \to ZH$ process, a sample generated using POWHEG at LO in QCD and interfaced with PYTHIA 8 is used instead.

The parton distribution function (PDF) uncertainties have been evaluated following the PDF4LHC recommendations for LHC Run II [91], using 30 PDF Hessian uncertainty variations and an α_S variation, present in the `PDF4LHC15_30` PDF set. The impact of each variation is simply evaluated in each STXS category. Each variation is considered a well-defined uncertainty source, whose effect is correlated across the full phase space. These PDF uncertainties are quite small, with a sum in quadrature of their contributions ranging from 1% to 3% for the Drell-Yan processes, and ranging from 2% to 5% for the $gg \to ZH$ process.

Uncertainties from missing higher orders in the QCD calculations have been, as usual, evaluated using variations of the renormalization and factorization scales. However, contrary to the PDF uncertainties, the variations of the scales are not considered as well-defined uncertainty sources, and are mere proxys to estimate the QCD uncertainty. A procedure is then needed to correctly estimate the uncertainty in each exclusive STXS category, and to define reasonable correlations between the uncertainties across the STXS categories. They are implemented as uncertainties across the p_{T}^{V} categories (estimated inclusively in the number of jets), and as uncertainties in the three jet bins (estimated inclusively in p_{T}^{V}).

Six pairs of renormalization and factorization pairs are considered, varying by factors of 2 around their nominal value:

$$[\mu_R/\mu_R^{nom}, \mu_F/\mu_F^{nom}] : [1/2,1][1,1/2][2,1][1,2][1/2,1/2][2,2].$$

First, total relative uncertainties are computed in each inclusive p_{T}^{V} or n_{jet} region as the maximum deviation obtained in the set of renormalization and factorization pairs: there is therefore an uncertainty for $p_{\mathrm{T}}^{V} > 75\,\mathrm{GeV}$, another one for $p_{\mathrm{T}}^{V} > 150\,\mathrm{GeV}$, etc... Absolute cross-section uncertainties are derived from this relative variations: Δ_{75}, Δ_{150}, Δ_{250} and Δ_{400} for the p_{T}^{V} categories, Δ^1 and Δ^2 for the jet categories.

A migration uncertainty is then defined along each category boundary by an anticorrelated variation of Δ_X for $p_{\mathrm{T}}^{V} > X$ and $-\Delta_X$ for $p_{\mathrm{T}}^{V} < X$, and similarly for the jet categories. The variation Δ_X is distributed across the full spectrum above the boundary X so that the relative uncertainty is the same in each exclusive category. The variation $-\Delta_X$ is applied to the category just below the boundary. This procedure follows the philosophy of the Stewart-Tackmann prescription for the treatment of scale uncertainties in exclusive categories [92]. Taking the category $75\,\mathrm{GeV} < p_{\mathrm{T}}^{V} < 150\,\mathrm{GeV}$ as an example: it will by affected by the Δ_{75} uncertainty (estimated from $p_{\mathrm{T}}^{V} > 75\,\mathrm{GeV}$), and by the $-\Delta_{150}$ uncertainty, and the effective total uncertainty is the sum in quadrature of these two terms. However, this procedure is quite conservative for the categories at high p_{T}^{V}, which are by construction affected by all the uncertainties associated to each boundary below them. To mitigate this effect, the uncertainties Δ_{150}, Δ_{250} and Δ_{400} are scaled by a factor 0.5, which was tuned by comparing the total uncertainty in inclusive regions, computed as the quadratic sum of the relevant Δ, to the maximum of the scale variations that was used as an input, and making sure the result is not too conservative.

Figure 1.12 presents the relative QCD uncertainties related to the p_{T}^{V} boundaries as computed by this procedure for the WH, $q\bar{q} \to ZH$ and $gg \to ZH$ processes, along with their quadratic sum. They amount to 3-4% for the Drell-Yan processes, but are as large as 40% for the $gg \to ZH$ production. Figure 1.13 shows similar information but for the QCD uncertainties related to the n_{jet} splitting, along with the total sum of QCD uncertainties. The Δ^1 and Δ^2 migration uncertainties have typically a larger impact than the p_{T}^{V} ones, of the order of 7% in the 1-jet categories, and 10% in the $\geq$ 2-jet categories.

Finally, table 1.3 displays a summary of these uncertainties, inclusively in the number of jets, and in the p_{T}^{V} categories that will be used for the measurement in the VH($b\bar{b}$) channel that will be presented in the next chapters. The cross-section in each category is shown as well for reference.

1.4.3 Constraining anomalous Higgs boson interactions with the $VH, H \to b\bar{b}$ process

As explained in section 1.2 differential measurements of the Higgs boson processes can be interpreted in the context of effective field theories to probe the strength and tensor structure of the Higgs boson interactions. The formalism used in the VH($b\bar{b}$) analysis is that of the *Strongly Interacting Little Higgs* (SILH) [93, 94] that is defined as the effective theory of a strongly interacting sector in which a light composite Higgs boson arises as a pseudo Goldstone boson and is responsible for EW symmetry breaking. Among the operators defined in this formulation, four directly affect the VH production cross-sections as they introduce new terms in the interactions of the Higgs boson with the electroweak

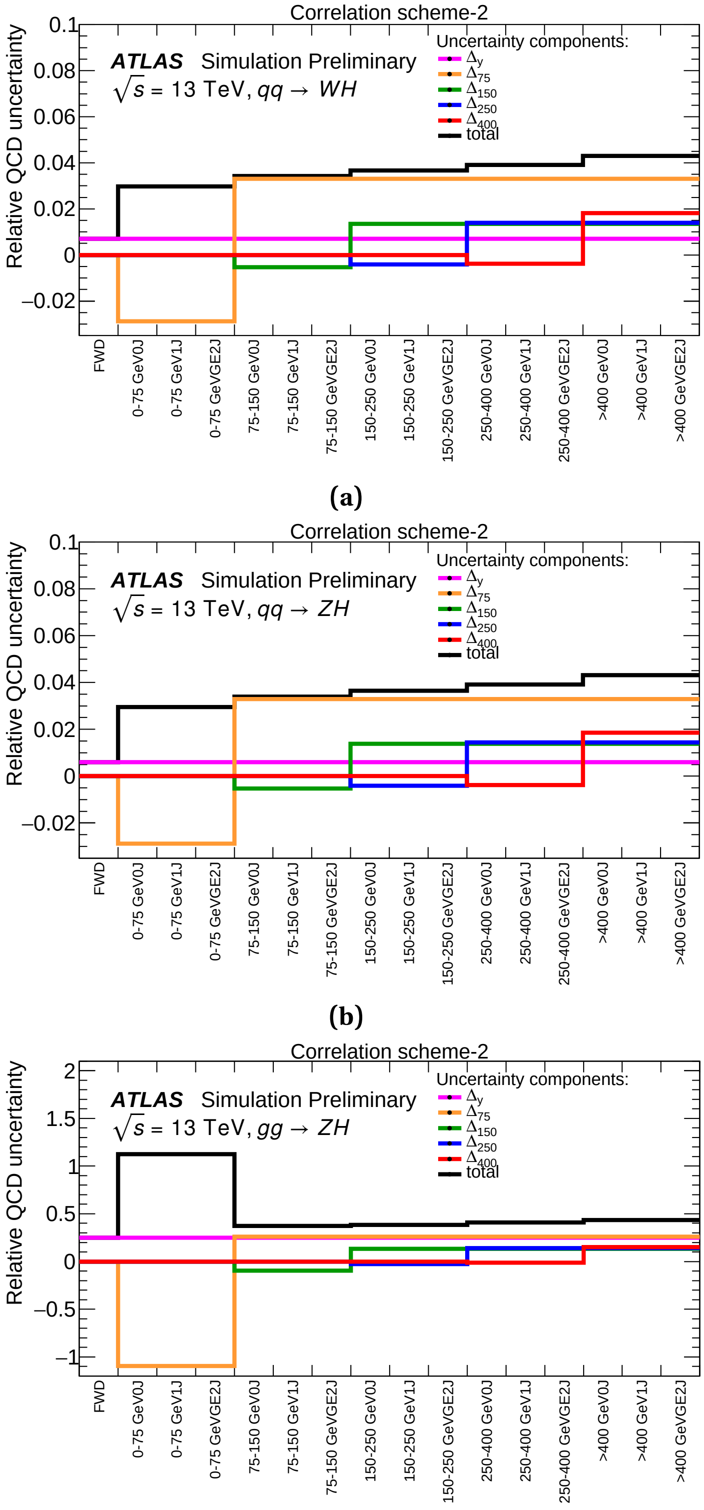

(a)

(b)

(c)

Figure 1.12: Relative QCD uncertainties related to the p_{T}^{V} boundaries and overall uncertainty in the STXS categories for (a) WH, (b) $q\bar{q} \to ZH$, and (c) $gg \to ZH$. Δ_{75}, Δ_{150}, Δ_{250} and Δ_{400} are the four migration uncertainties, Δ_y is the overall scale uncertainty on the cross section described in section 1.4.1. The black line is the quadrature sum of all the represented scale uncertainties. The x-axis labeling indicates the p_{T}^{V} boundaries in GeV, the njet multiplicity (0, 1 and ≥ 2 jets, as `0J`, `1J` and `GE2J`). The `FWD` bin includes all contributions from the forward Higgs region ($|y_H| > 2.5$).

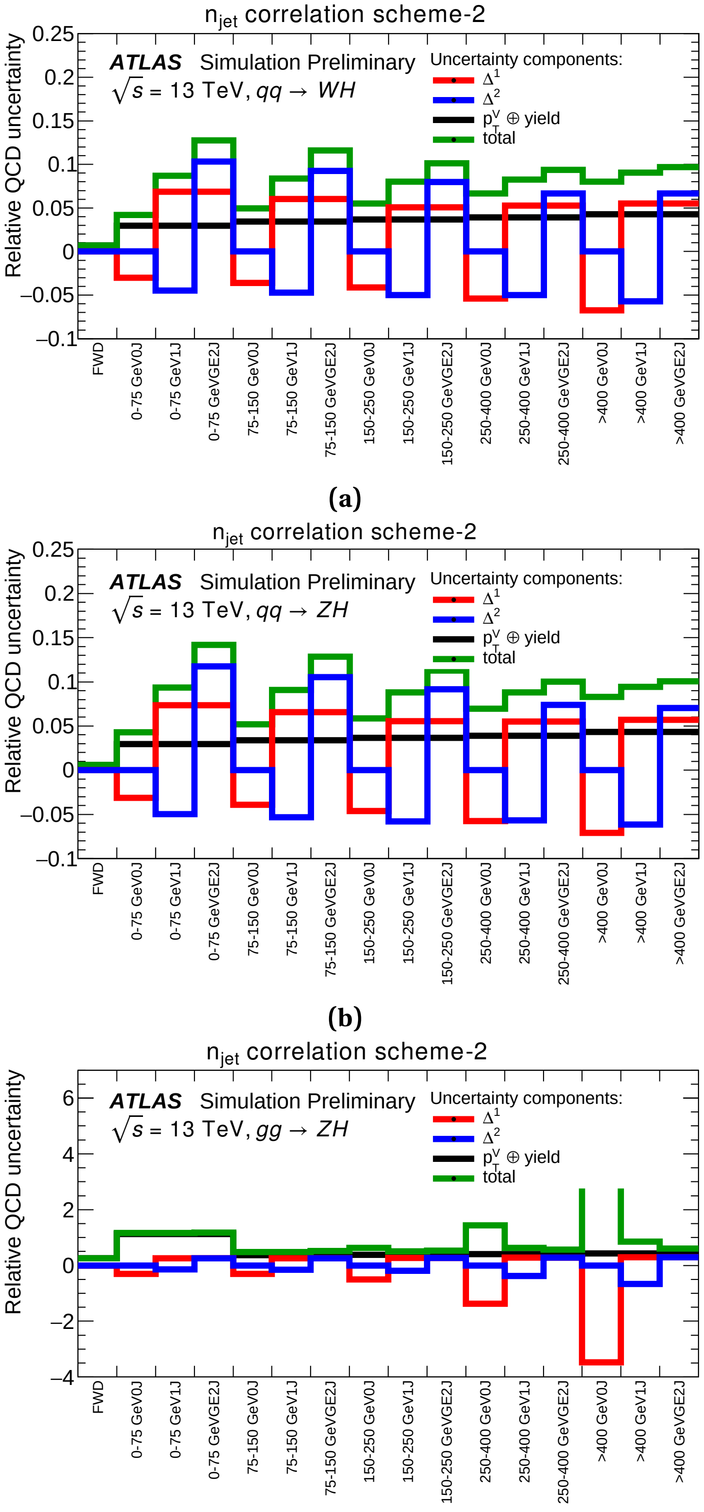

Figure 1.13: Relative QCD uncertainties related to the n_{jet} splitting (Δ^1 and Δ^2), along with the total impact of p_T^V migration uncertainties (black) and the quadrature sum of all uncertainties in each STXS category (green) including overall cross section uncertainties, for (a) WH, (b) $q\bar{q} \to ZH$, and (c) $gg \to ZH$. The x-axis labeling indicates the p_T^V boundaries in GeV, the njet multiplicity (0, 1 and ≥ 2 jets, as `0J`, `1J` and `GE2J`). The `FWD` bin includes all contributions from the forward Higgs region ($|y_H| > 2.5$).

Table 1.3: Cross-section predictions and uncertainties, estimated inclusively in the number of jets, and in the p_{T}^{V} categorization that will be used for the *VH*$(b\bar{b})$ analysis presented in the next chapters. The total uncertainty is the quadrature sum of the QCD and PDF+α_S uncertainties. The cross-sections include the branching ratios for leptonic decays of the W and for decays into charged leptons of the Z. The ZH lines include both the Drell-Yan contribution and the $gg \to ZH$ process.

Process	p_{T}^{V} Boundaries [GeV]	Cross-section [fb]	PDF+α_S unc. [%]	QCD unc. [%]	Total unc. [%]
WH	$[0,75[$	216.4	1.9	3.0	3.5
WH	$[75,150[$	135.0	2.2	3.4	4.0
WH	$[150,250[$	41.24	1.8	3.6	4.1
WH	$[250,\infty[$	12.16	2.2	3.9	4.4
ZH	$[0,75[$	112.4	1.7	6.7	6.9
ZH	$[75,150[$	87.0	1.4	7.8	7.9
ZH	$[150,250[$	32.3	1.4	12	12
ZH	$[250,\infty[$	8.33	1.7	10	10
$gg \to ZH$	$[0,75[$	6.7	2.6	100	100
$gg \to ZH$	$[75,150[$	17.0	2.7	37	37
$gg \to ZH$	$[150,250[$	10.2	2.9	38	38
$gg \to ZH$	$[250,\infty[$	1.94	3.3	41	41

W and B fields, and therefore with the W and Z bosons:

$$\begin{aligned}
\mathcal{O}_{HW} &= i\left(D^{\mu}H\right)^{\dagger}\sigma^{a}\left(D^{\nu}H\right)W^{a}_{\mu\nu} \\
\mathcal{O}_{HB} &= i\left(D^{\mu}H\right)^{\dagger}\left(D^{\nu}H\right)B_{\mu\nu} \\
\mathcal{O}_{W} &= \frac{i}{2}\left(H^{\dagger}\sigma^{a}\overleftrightarrow{D}^{\mu}H\right)D^{\nu}W^{a}_{\mu\nu} \\
\mathcal{O}_{B} &= \frac{i}{2}\left(H^{\dagger}\overleftrightarrow{D}^{\mu}H\right)\partial^{\nu}B_{\mu\nu}
\end{aligned}$$

The corresponding CP-odd operators $\tilde{\mathcal{O}}_{HW}$, $\tilde{\mathcal{O}}_{HB}$, $\tilde{\mathcal{O}}_{W}$, and $\tilde{\mathcal{O}}_{B}$, are not considered.

Because of the loops involved in this process, the anomalous contributions to the $gg \to ZH$ production appear in this formalism either through higher-dimension ($D \geq 8$) operators, or through corrections that are formally at NNLO in QCD and were not available at the time the analysis was made [95]. The $gg \to ZH$ production cross-section is therefore fixed to the SM prediction in this interpretation.

The coupling between the Higgs boson and the down-type quarks is modified through the operator $\mathcal{O}_d = y_d|H|^2\bar{Q}_{\mathrm{L}}Hd_{\mathrm{R}}$ (plus Hermitian conjugate) with Yukawa coupling strength y_d. The partial width Γ_H^{bb} and the total width Γ_H are therefore affected, inducing a variation in the $H \to b\bar{b}$ branching fraction.

The *Higgs Effective Lagrangian* (HEL) implementation [96] of the SILH formalism is used to set constraints on the coefficients of the operators affecting the *VH*$(b\bar{b})$ process as the relations between these coefficients and the cross-sections in the STXS framework have been computed [97], including both the interference and the BSM terms as defined in section 1.2. In the HEL implementation, the coefficients of interest are reparametrized into dimensionless ones:

$$\bar{c}_{HW} = \frac{m_W^2}{g}\frac{c_{HW}}{\Lambda^2}, \quad \bar{c}_{HB} = \frac{m_W^2}{g'}\frac{c_{HB}}{\Lambda^2}, \quad \bar{c}_{W} = \frac{m_W^2}{g}\frac{c_{W}}{\Lambda^2}, \quad \bar{c}_{B} = \frac{m_W^2}{g'}\frac{c_{B}}{\Lambda^2}, \quad \bar{c}_{d} = v^2\frac{c_{d}}{\Lambda^2}, \tag{1.7}$$

where g and g' are the $SU(2)$ and $U(1)$ SM gauge couplings and v is the vacuum expectation value of the Higgs boson field. The sum $\bar{c}_W + \bar{c}_B$ is strongly constrained by precision EW data [98] as it is directly related to the oblique parameter ΔS [99] by $\alpha \Delta S = 4\sin^2\theta_W(\bar{c}_W + \bar{c}_B)$. It can thus assumed to be zero, so that the measurements in the $VH(b\bar{b})$ channel are used to set constraints on $\bar{c}_{HW}$, $\bar{c}_{HB}$, $\bar{c}_W - \bar{c}_B$ and $\bar{c}_d$.

Chapter 2

Search for the Higgs boson in the $VH(b\bar{b})$ channel using 80 fb^{-1} of 13 TeV data

The search for the Higgs boson in its decay to b-quarks and produced in association with a vector boson is a relatively complex analysis because of the large phase space studied, of the low signal-to-background ratio and of the diversity of background processes to consider, which all contribute to make the impact of systematic uncertainties significant. This chapter reports in detail the analysis performed using 80 fb^{-1}of 13 TeV data collected during the first three years of the Run-2 of the LHC. Section 2.1 aims at providing a general overview of the analysis as well as justifying some important design choices. The dataset and the simulated samples used are described in section 2.2. In section 2.3 the selections applied to the physics objects are listed, then the event selections are described. The data-driven estimation of the multi-jet backgrounds is presented in section 2.4. The estimation of the many systematic uncertainties is reported in section 2.5. The statistical analysis is described in detail in section 2.6, and its results are presented in section 2.7.

2.1 Introduction to the analysis

The goal of the $VH(b\bar{b})$ analysis is – obviously – to maximize the sensitivity to this process. As mentioned in section 1.4, the topology of the $VH(b\bar{b})$ events is rather simple, with two b-jets coming from the Higgs boson decay, two leptons from the vector boson decay, and possible additional jets from initial or final state radiation.

Therefore three channels are considered, with 0, 1 or 2 charged leptons in the final state to target the $Z \to \nu\nu$, $W \to \ell\nu$ or $Z \to \ell\ell$ decays respectively. Among the charged leptons, only electrons and muons are considered: the much lower purity achieved in the hadronic τ reconstruction makes their use a high-effort, low-reward task.

Straightforward selections on the charged leptons and on the missing transverse energy allow to reduce significantly multi-jet backgrounds, so that in all channels the signal has to be discriminated against backgrounds involving W or Z bosons. As the goal is to reconstruct the $H \to b\bar{b}$ decay, two b-tagged jets are required in the events. This reduces the backgrounds further, but many different ones still have significant contributions: processes with vector bosons and heavy flavour jets ($V+$hf), QCD and electroweak production of top-quarks (both $t\bar{t}$ pairs and single-top events), and diboson processes (WZ, ZZ).

It is worth pointing out how crucial a high-performance b-tagging algorithm is for this analysis, with a high efficiency for b-jet identification and a large rejection of both light and c-jets. Whenever the rejection is worsened, the composition of the $V+$jets backgrounds change drastically, with a larger contamination from the higher cross-section V+light-flavour jets and $V+c$ processes. That degrades the signal over background ratio of the analysis, and makes it more difficult to control precisely the uncertainties in the modelling of the V+jets process, which is a key aspect of the analysis.

The events kinematics are then used used to improve the discrimination between signal and backgrounds, the most useful variables being the dijet invariant mass, the transverse momentum of the vector boson (p_{T}^{V}), and the number of additional jets. The application of specific techniques to improve the b-jet energy scale makes the signal invariant mass peak narrower and therefore increases further the importance of this variable. The harder p_{T}^{V} spectrum for the signal and the differences in the number of additional jets are exploited by the creation of categories to classify the events according to them. The bulk of the sensitivity of the analysis therefore lies in the high-p_{T}regime, broadly around 200 GeV. In the 0- and 1-lepton channels, the background composition (in particular the presence of semi-leptonic $t\bar{t}$ decays) makes the categories without any additional jets much more sensitive than the ones with such jets.

Three analyses are actually performed.

In the main analysis, a multivariate classifier is trained inside each analysis category to improve the separation between the signal and the backgrounds. The binned outputs of the classifiers are fitted simultaneously to extract the signal strength and perform the statistical analysis of the data.

A validation analysis is performed by extracting the signal strength of the diboson ($VZ, Z \rightarrow b\bar{b}$) process using similar classifiers, but trained to discriminate the diboson from the rest of the backgrounds. This validation is actually done before the unblinding of the Higgs results, and is a powerful tool to validate the whole analysis given the proximity of the VZ and VH processes.

Finally, the main result is cross-checked by a dijet-mass analysis, in which the dijet invariant mass is used in the statistical analysis instead of the multivariate classifier output. Additional selections on the angular separation between the b-tagged jets, optimized in each p_{T}^{V} category, are applied to improve the sensitivity of this cross-check.

In all cases, systematic uncertainties have a significant impact on the results. Thus they need to be evaluated very carefully, in particular the ones concerning the modelling of the signal and of the backgrounds by the Monte Carlo generators. As all analysis categories are fitted together in a global profile likelihood, the large amount of data in some categories constrain some uncertainties, and the propagation of such constraints across the phase space must be well controlled to avoid biased or over-optimistic results. The validity of the uncertainties model implemented in the statistical analysis, and in particular that of the background uncertainties model, is one of the key and time-consuming aspects of the analysis.

2.2 Dataset, signal and backgrounds

2.2.1 Recorded data

The analysis uses data recorded in the first three years of the Run-2 of the LHC, i.e between 2015 and 2017. The events are selected for the analysis only if they were recorded when all ATLAS subdetectors have been in good operating conditions, and if they are of good quality. This basic data quality selection has an efficiency of about 94%, which corresponds to a useful integrated luminosity of

79.8 ± 1.6 fb^{-1} [100, 101]. The average number of inelastic interactions per bunch-crossing (pile-up) varied significantly between the data periods, from about 13 to 56, with an average of 32.

2.2.2 Simulated samples

The signal and SM background processes are simulated using events from Monte Carlo (MC) generators, with the exception of the multi-jet background which is estimated using data-driven techniques. The simulated datasets are normalised using the most accurate theoretical cross-sections available, and were generated with at least NLO accuracy (with one exception).

The $qq \to ZH$ and $qq \to WH$ samples were generated in the POWHEG-BOX v2 framework [102] using the GOSAM algorithm [103] and the MINLO procedure [88, 104] for merging correctly the jet multiplicities. The loop-induced $gg \to ZH$ events were generated at LO using POWHEG-BOX v2. All signal samples were interfaced with PYTHIA 8.212 [89] for parton showering and hadronization, and using the AZNLO tune [90] of the underlying event. They were generated using the first PDF in the NNPDF3.0NLO set [105] and then reweighted to the PDF4LHC15NLO set [91] using the algorithm implemented in POWEHEG-BOX v2. The lack of NLO EW corrections to the $qq \to VH$ processes in the generators is partially accounted by a reweighting of the events as function of the transverse momentum of the vector boson according to the differential cross-section computed with HAWK [77, 78]. The signal samples are normalised using the cross-section computations discussed in section 1.4.1.

The different production modes of top-quarks, through QCD and electroweak processes, were generated in POWHEG-BOX v2 [106–108], interfaced to PYTHIA 8.230 for parton showering and hadronization, and using the A14 tune [109]. They used the NNPDF3.0NLO set. The samples are normalised using cross-sections computed at NNLO+NNLL accuracy for the top-quark pair production [110], at NLO accuracy for the s-channel and t-channel processes [111, 112] and at an approximate NNLO accuracy for the Wt process [113].

The background samples of vector bosons with additional jets, $W \to \ell\nu$, $Z/\gamma^* \to \ell\ell$ and $Z \to \nu\nu$, were generated using SHERPA 2.2.1 [114–118] for both matrix-element and parton-shower, with the default SHERPA tune for the underlying event. The NNPDF3.0NNLO set was used. The cross-sections to which the samples are normalised are computed at NNLO accuracy [119]. These V+jets samples are a great example to show the importance of accurate, high-order MC simulations in a VH($b\bar{b}$) analysis where background modelling systematic uncertainties have a large impact. Figure 2.1a shows a distribution of the azimuthal angle between the jets in W+2-jets events in the Run-1 VH($b\bar{b}$) analysis, which relied on an earlier version of SHERPA where such events were simulated at LO accuracy. The significant disagreement with the data was treated with an ad-hoc correction, to which a sizable systematic uncertainty was then associated. Huge progress in Monte Carlo generators was achieved in the last 5-10 years, with the development of techniques such as MEPS@NLO that allows to generate W + 2-jets at NLO accuracy thanks to a proper matching of the W + n-partons matrix element calculations at higher orders with parton showers. This improves significantly the agreement with the data, as shown on fig. 2.1b, and in turns contributes to the reduction of the background modelling systematic uncertainties.

Diboson production (WW, WZ and ZZ) was simulated using SHERPA 2.2.1 for matrix element and parton-shower, with the exception of the loop-induced $gg \to VV$ processes which were made using SHERPA 2.2.2. The NNPDF3.0NNLO was used in all cases, and the samples were normalised to cross-sections computed at NLO accuracy.

Table 2.1 summarises the generators used for the simulation of the signal and background

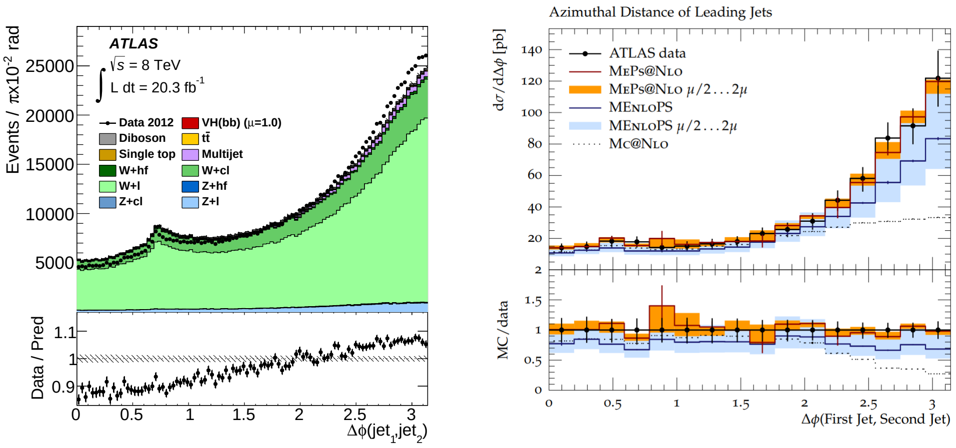

(a) **(b)**

Figure 2.1: (a) Distribution of the azimuthal angle between the jets in $W+2$-jets events in the 1-lepton, 0-tag, 2-jet category of the Run-1 $VH(b\bar{b})$ analysis [51]. A clear shape difference between the data (black dots) and the simulation made using Sherpa 1.4.1 (green colors) is observed. (b) Same distribution, comparing unfolded ATLAS 7 TeV data [120] (black dots) with predictions using the MEPs@Nlo matching technique as implemented in recent Sherpa versions such as 2.2.1 [118] (red line). The use of higher-order terms improves significantly the agreement with the data.

Table 2.1: The generators used for the simulation of the signal and background processes. If not specified, the order of the cross-section calculation refers to the expansion in the strong coupling constant (α_S). The acronyms ME, PS and UE stand for matrix element, parton shower and underlying event, respectively.

Process	ME generator	ME PDF	PS and Hadronisation	UE model tune	Cross-section order
Signal, mass set to 125 GeV and $b\bar{b}$ branching fraction to 58%					
$qq \to WH$ $\to \ell\nu b\bar{b}$	Powheg-Box v2 [102] + GoSam [103] + MiNLO [88, 123]	NNPDF3.0NLO [105]	Pythia 8.212 [121]	AZNLO [122]	NNLO(QCD)+ NLO(EW) [70–76]
$qq \to ZH$ $\to \nu\nu b\bar{b}/\ell\ell b\bar{b}$	Powheg-Box v2 + GoSam + MiNLO	NNPDF3.0NLO	Pythia 8.212	AZNLO	NNLO(QCD)+ NLO(EW)
$gg \to ZH$ $\to \nu\nu b\bar{b}/\ell\ell b\bar{b}$	Powheg-Box v2	NNPDF3.0NLO	Pythia 8.212	AZNLO	NLO+ NLL [80–84]
Top quark, mass set to 172.5 GeV					
$t\bar{t}$	Powheg-Box v2 [106]	NNPDF3.0NLO	Pythia 8.230	A14 [109]	NNLO+NNLL [110]
s-channel	Powheg-Box v2 [107]	NNPDF3.0NLO	Pythia 8.230	A14	NLO [112]
t-channel	Powheg-Box v2 [107]	NNPDF3.0NLO	Pythia 8.230	A14	NLO [111]
Wt	Powheg-Box v2 [108]	NNPDF3.0NLO	Pythia 8.230	A14	Approximate NNLO [113]
Vector boson + jets					
$W \to \ell\nu$	Sherpa 2.2.1 [115, 116, 124]	NNPDF3.0NNLO	Sherpa 2.2.1 [117, 118]	Default	NNLO [119]
$Z/\gamma^* \to \ell\ell$	Sherpa 2.2.1	NNPDF3.0NNLO	Sherpa 2.2.1	Default	NNLO
$Z \to \nu\nu$	Sherpa 2.2.1	NNPDF3.0NNLO	Sherpa 2.2.1	Default	NNLO
Diboson					
$qq \to WW$	Sherpa 2.2.1	NNPDF3.0NNLO	Sherpa 2.2.1	Default	NLO
$qq \to WZ$	Sherpa 2.2.1	NNPDF3.0NNLO	Sherpa 2.2.1	Default	NLO
$qq \to ZZ$	Sherpa 2.2.1	NNPDF3.0NNLO	Sherpa 2.2.1	Default	NLO
$gg \to VV$	Sherpa 2.2.2	NNPDF3.0NNLO	Sherpa 2.2.2	Default	NLO

processes.

All generated events were passed through a full simulation of the ATLAS detector [125] based on GEANT 4 [126], then were reconstructed using the standard ATLAS software. The consequences of the multiple interactions in the same and nearby bunch-crossings (in-time and out-of-time pile-up) is accounted in the simulated events by overlaying additional minimum-bias events before running the reconstruction. This minimum-bias simulation is performed using the soft QCD processes of Pythia 8.186 with the A2 tune [127] and the MSTW2008LO [128] PDF set.

The EvtGen v1.2.0 program [129] was used to model the decays of bottom and charm hadrons of all samples of simulated events, except the ones generated using Sherpa where the internal routines were used instead.

Alternative samples of simulated events are used in the determination of the systematic uncertainties in the signal and background modelling. They are made either using different Monte Carlo generators, or using different settings of the nominal generator, and are described when needed in section 2.5.

2.2.3 Filters in datasets of simulated events

Disk space and CPU considerations limit the amount of Monte Carlo events that can be produced and used in the analysis, in particular for processes with large cross-sections such as $t\bar{t}$ or $V+$ jets. Conversely, large datasets of simulated samples are required for a smooth modelling of the backgrounds in the analysis. Indeed, as will be showed in section 2.6, statistical uncertainties in the background templates have a relatively large impact on the total systematic uncertainty of the measurement.

To mitigate this effect, filters are used at various stages in the generation of the events so that the effective luminosity of the datasets is increased in the more relevant parts of the phase space. The ideal case would be that the generated events cover exactly the phase space of the analysis, with an acceptance close to 100%, and with enhanced statistics in the more sensitive regions. However, as datasets of very common processes such as $t\bar{t}$ pair production or $V+$ jets productions are used by many analyses in the collaboration, the definitions of the filters is the result of a compromise. Studies were performed between each iteration of the $VH(b\bar{b})$ analysis to optimise the filters or propose new ones, so that the amount of MC events in the analysis phase space scales at least as well as the integrated luminosity of the data.

Relevant examples for the 0-lepton channel are discussed in Charles Delporte's thesis [130]. The studies were performed after the previous publication that used 36 $\mathrm{fb}^{-1}$of 13 TeV data [53], and looked at the backgrounds in the most sensitive bins of the multivariate discriminant output to understand which parts of their phase space were in most need of increased MC statistics.

The large Sherpa $V+$ jets samples are maybe the most commonly used in ATLAS, as these processes appear as background in almost every analysis that requires low multiplicity of charged leptons, or large missing transverse momentum. They are filtered on the flavour of the hadrons, i.e $V+b$ and $V+c$ events end up in dedicated datasets. In order to increase the effective luminosity in phase space areas used by many searches or measurements, the generation is sliced in bins of $\max(H_\mathrm{T}, p_\mathrm{T}^V)$, where H_T is the scalar sum of the transverse momenta of the jets: this allows to target both high-p_T^V events, and events with lower p_T^V but large jet multiplicities. Delporte showed that this slicing strategy was quite inappropriate for the $Z \to \nu\nu$ samples, as many events with large jet multiplicity but low p_T^V do not even pass the lowest unprescaled missing transverse momentum trigger available in ATLAS. Using a slicing strategy based on p_T^V improves the MC statistical uncertainty by a factor two for the same number of generated events. Such a strategy was indeed used for some new $Z \to \nu\nu$ samples used in the analysis presented in this document.

The $t\bar{t}$ background present in the 0-lepton channel represents a very peculiar part of the top-pair production phase space: with no charged lepton and 2 b-tagged jets in the final state, it means that several of the $t\bar{t}$ decay products are out of the acceptance or do not pass the analysis selections.

Therefore it was shown that the use of $E_{\mathrm{T}}^{\mathrm{miss}}$-filtered $t\bar{t}$ events initially designed for SUSY searches allowed to increase significantly the statistics in the analysis phase space, when properly merged with the large dataset commonly used in ATLAS that contains all semi-leptonic and dileptonic decays generated inclusively.

2.3 Object and event selection

As mentioned in section 2.1, the selections applied in the analysis are relatively straightforward, with the main goal of selecting the typical topology of the $VH(b\bar{b})$ events, and derive from a few guiding principles.

The first one is to have selections as consistent as possible between the three channels. As the main backgrounds are common between the channels ($Z(\ell\ell)$ + jets in 2-lepton vs $Z(\nu\nu)$ + jets in 0-lepton channel, W+ jets in 0- and 1-lepton channels, $t\bar{t}$ in all channels), and as the use of a simulatenous profile likelihood fit allows to constrain the important background modelling systematic uncertainties, keeping the selections close between the three channels allows to select very similar areas in phase space, and therefore limit the extrapolation uncertainties.

The second is to have lepton selections that keep the three channels orthogonal to each other, while optimising each channel according to its needs in terms of purity vs acceptance. This leads to the definition of two quality criteria for the leptons: a *loose* one and a *tight* one.

2.3.1 Object reconstruction

Interaction vertices are reconstructed from the tracks measured in the inner detector [131]. The primary vertex is selected from them as the one with the highest sum of transverse momenta of associated tracks.

Electrons are reconstructed using topological clusters of energy deposits in the calorimeter [132] that are matched to a track in the inner detector. Their energy calibration is mainly based on a data sample of $Z \to e^+e^-$ events [133]. Non-prompt and pile-up tracks are rejected by requiring small transverse ($\mathrm{IP}_{r\phi}$) and longitudinal (IP_z) impact parameters, defined with respect to the primary vertex positions. Tracks must have $|\mathrm{IP}_{r\phi}|/\sigma_{\mathrm{IP}_{r\phi}} < 5$ and $|\mathrm{IP}_z| < 0.5\,\mathrm{mm}$, where $\sigma_{\mathrm{IP}_{r\phi}}$ is the uncertainty in the measurement of the transverse impact parameter. *Loose* electrons are required to have $p_{\mathrm{T}} > 7\,\mathrm{GeV}$ and $|\eta| < 2.47$, to meet the 'LooseLH' likelihood-based quality criterion computed from shower shape and track quality variables [134], and to pass a loose track isolation requirement. The latter consists in a selection tuned for a constant efficiency of 99% as function of the electron p_{T}, asking for the electron track to be isolated from other tracks in a cone of variable size with $\Delta R_{\mathrm{max}} = 0.2$[1]. *Tight* electrons are selected by requiring in addition that they pass the 'TightLH' quality criterion, and a calorimeter-based isolation specifically tuned to improve the rejection of the multi-jet background in the 1-lepton channel, with a signal efficiency of 95% and a rejection factor of the multi-jet events of about 10 [135].

Following [136, 137], muons are reconstructed as tracks in the inner detector matched to tracks in the muon spectrometer up to $|\eta| = 2.5$. The acceptance is increased up to $|\eta| = 2.7$ by using the muon spectrometer alone, and in the region $|\eta| < 0.1$ the limited coverage of muon chambers is worked around by using tracks in the inner detector matched to calorimeter energy deposits consistent with typical muon energy loss. Similar to the electron case, non-prompt and pile-up tracks are rejected

---

[1] ↑The standard definition in hadron collider physics $\Delta R^2 = \Delta\eta^2 + \Delta\phi^2$ is used.

by applying impact parameter requirements: $|\mathrm{IP}_{r\phi}|/\sigma_{\mathrm{IP}_{r\phi}} < 3$ and $|\mathrm{IP}_z| < 0.5$ mm. *Loose* muons are required to have $p_\mathrm{T} > 7$ GeV and $|\eta| < 2.7$, to meet the 'loose' quality criterion defined in [137] and to pass a loose track isolation requirement. The latter is defined the same way as for electrons with a constant efficiency of 99%, but using an isolation cone with $\Delta R_\mathrm{max} = 0.3$. In addition, *tight* muons need to fulfil the 'medium' quality criterion and a stricter track isolation, that was also optimised specifically for the 1-lepton channel and yields a rejection of the multi-jet background by a factor about 3 for a signal efficiency of 95% [135].

Hadronically decaying τ-leptons are reconstructed as jets from noise-suppressed energy clusters, using the anti-k_t algorithm with radius parameter $R = 0.4$ [138, 139]. They are required to have exactly one or three matching tracks in the inner detector within a cone of size $\Delta R = 0.2$ around the jet axis, to have $p_\mathrm{T} > 20$ GeV and $|\eta| < 2.5$, and to be outside the transition region between the barrel and endcap calorimeters ($1.37 < |\eta| < 1.52$). A multivariate classifier relying on boosted decision trees is employed to reject jets being reconstructed and identified as τ-leptons, using information from the calorimeters and from the tracking detectors. The 'medium' quality criterion defined in [139] is used. Hadronically decaying τ-leptons are only used in the analysis in the overlap removal procedure described at the end of this section. This has an impact on the jet multiplicity in the events.

Jets are reconstructed from noise-suppressed topological energy clusters in the calorimeter [140] using the anti-k_t algorithm [86] with radius parameter $R = 0.4$. The energies of the jets are calibrated using a jet energy scale correction (JES) obtained from both simulation and *in situ* calibration using data [141, 142]. A jet vertex tagger [143] based on track and vertex information is used to remove jets associated with vertices other than the primary one, for jets with $p_\mathrm{T} < 60$ GeV and $|\eta| < 2.4$. Jets arising from non-collision backgrounds or noise in the calorimeters are identified using jet cleaning criteria [144], and events containing such jets are vetoed. Jets in the central region of the detector ($|\eta| < 2.5$) are required to have $p_\mathrm{T} > 20$ GeV. Outside of the acceptance of the inner detector ($2.5 < |\eta| < 4.5$), the requirement is raised to $p_\mathrm{T} > 30$ GeV in order to reduce the contamination by pile-up jets.

In the central region, jets are tagged as containing b-hadrons using a multivariate discriminant (MV2) [145], that combines information from several lower-level algorithms based on the impact parameters of the associated tracks, on the reconstruction of secondary vertices, and on a multi-vertex fitter that attempts to reconstruct the full b- to c-hadron decay chain. The chosen working point was tuned for a selection efficiency of 70% for b-jets in simulated $t\bar{t}$ events, corresponding to light-flavour (u-, d-, s-quark and gluon) and c-jet misidentification efficiencies of 0.3% and 12.5% respectively. The efficiencies in the simulation are corrected using calibrations computed from the analysis of $t\bar{t}$ data for b- and c-jets [146], and of multi-jet data for light-flavour jets [147]. Small efficiency differences observed in simulation between the samples generated using SHERPA and the other samples that use EVTGEN for the decay of heavy flavour hadrons are corrected using additional 'MC-to-MC' scale-factors. The continuous and impressive evolution of the b-tagging algorithms over the past years has been one of the driving factors for the improvement of the $VH(b\bar{b})$ analysis between its successive iterations, as it improves the signal-over-background ratio by removing events with signal-like kinematics but at least one c- or light-flavour jet in the Higgs candidate dijet pair. As a point of comparison, the misidentification efficiencies for the same b-jet efficiency of 70% were 0.5% and 12.5% for light-flavour and c-jets respectively in the previous analysis performed with 36 fb^{-1}of 13 TeV data [53], and about 1% and 20% in the analysis of the Run-1 data [51]. The difference between the Run-1 performance and the early Run-2 performance is estimated to come half from algorithmic improvements and half from the addition of the insertable B-layer detector at the heart of the ATLAS inner detector during the first long shutdown of the LHC [148, 149]. The further performance improvement between the early Run-2 analysis and the one discussed in this document is coming only from improved tuning and training of the algorithms.

Simulated jets are labelled as b-, c- or light-flavour jets according to which hadrons with $p_{\mathrm{T}} > 5\,\mathrm{GeV}$ are found within a cone of size $\Delta R = 0.3$ around their axis. If a b-hadron is present the jet is labelled as a b-jet. If not, but a c-hadron is found, then the jet is labelled as a c-jet. In the other cases the jet is labelled as a light jet. Simulated $V+$jets events are categorised depending on the labels of the jets that form the Higgs boson candidate: $V + ll$ when they are both ligh-flavour jets, $V + cl$ when on of them is a c-jet and the other one is a light-flavour jet; the other cases ($V + bb$, $V + bl$,...) are regrouped with the denomination $V+$hf (heavy flavour).

As already mentioned, the statistical uncertainty in the datasets of simulated events is a sizable source of uncertainty in the measurement of $VH(b\bar{b})$. Processes with large production cross-section and small selection efficiencies can be difficult to generate in large enough quantities to exceed significantly the integrated luminosity of the data. This is in particular the case of the $V+ll$ and $V+cl$ events, owing to the very large rejection of light-flavour jets achieved by the MV2 tagging discriminant. These events (as well as the WW events) are therefore not subjected to the b-tagging requirement, but instead they are weighted by the probability for their Higgs candidate jets to be tagged as b-jets. The probabilities are computed per jet, depending on its flavour, and are parameterised as a function of the jet kinematics ($p_{\mathrm{T}}$and η). As the processes subjected to this treatment represent only a sub-percent fraction of the total background, the assumption that the tagging probabilities of the jets in an event are independent from each other, which is not fully correct when the jets are close-by, is not causing any significant bias.

The JES correction applied as part of the jet calibration process is designed to obtain the correct response for the calorimeter energy deposits of an inclusive sample of jets [142]. Additional corrections can be implemented to improve the energy scale and resolution of the b-jets specifically, in order to improve the dijet-mass resolution of the signal. The first one applied to b-tagged jets is called the *muon-in-jet* correction, and is applied when a medium quality muon with $p_{\mathrm{T}} > 5\,\mathrm{GeV}$ is found within $\Delta R = 0.4$ of the jet, to better calibrate the jets with b- and c-hadron decays into muons which do not deposit their full energy in the calorimeter. Unlike in the lepton selection discussed previously, no isolation criteria are applied on the muons. When more than one muon is found, the one closest to the jet axis is chosen. The muon four-momentum is added to that of the jet. The small double-counting of the energy deposited by the muon in the calorimeter has a negligible effect. The b-jet response is further improved by a second correction, named *PtReco*, that is applied as function of the jet p_{T}. This correction is computed on simulated signal events, from the residual difference in scale between the reconstructed b-jets (with all other corrections applied) and the corresponding *truth jets*, formed by clustering the final-state particles in the Monte Carlo truth record, including muons and neutrinos. It increases the energy of the jets by only 1% for $p_{\mathrm{T}} > 100\,\mathrm{GeV}$, but by up to 12% at $p_{\mathrm{T}} = 20\,\mathrm{GeV}$. A larger correction is applied in case a muon or electron is identified within $\Delta R = 0.4$ of the jet axis, to account for the missing neutrino energy.

In the 2-lepton channel, the full reconstruction of the $Z \to \ell\ell$ decays with high an excellent resolution allows to further improve the estimate of the b-jets energy. In the plane transverse to the beam axis, the vectorial sum of the momenta of the reconstructed objects must be zero (within the resolution given by the intrinsic k_{T} of the partons). Therefore in ZH, $H \to b\bar{b}$ events the p_{T}^{Z} is expected to balance the sum of the momenta of the jets. This constraint is implemented in a likelihood fit that includes the momenta of all jets and leptons as well as their estimated resolutions. The jet energy resolution being much worse than that of the leptons, the fit mostly corrects the energies of the jets. In the best case where there are no additional jets in the events, the application of this likelihood-based correction of the b-jet energies on simulated signal events moves the central value of the dijet mass distribution closer to its nominal value, and improves its resolution by up to about 40%. This improvement is shown in fig. 2.2, along with the effect of the other two corrections. In the 0- and 1-lepton channels, where the neutrinos in the vector boson decays prevent the use of the kinematic constraint, the application of the *muon-in-jet* and *PtReco* corrections still yield a sizable improvement of 15-20% of the dijet mass resolution.

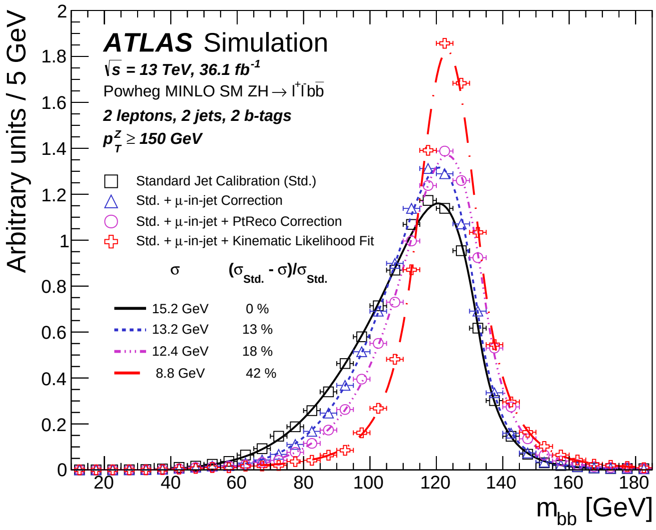

Figure 2.2: Comparison of the dijet mass distributions for the different corrections that are applied to the energy scale of b-tagged jets, for simulated signal events in the 2-lepton channel, 2-jet category, $p_T^Z > 150$ GeV region. The distributions are fitted by a Bukin function [150], and the values of the resolution are reported in the legend, along with the improvement with respect to the standard jet calibration.

The missing transverse momentum $\mathbf{E}_T^{\text{miss}}$ is reconstructed as the negative vector sum of the transverse momenta of electrons, muons, hadronically decaying τ-leptons and jets associated with the primary vertex, and of a 'soft term' that is built from well-reconstructed tracks matched to the primary vertex and not already matched to any of the physics objects [151].

As the object reconstruction and identification algorithms usually run independently from each other, an overlap removal procedure is applied to avoid any double counting between the reconstructed objects. Any hadronically decaying τ-lepton reconstructed closer than $\Delta R = 0.2$ to an electron or muon is removed, except in cases where the muon is of low quality. If a reconstructed muon shares a track in the inner detector with an electron, the latter is removed. Jets closer than $\Delta R = 0.2$ to an electron are removed, since the energy deposits in the calorimeter of any electron are always clustered in a jet. Any electrons reconstructed within $\Delta R = \min(0.4, 0.04 + 10\ \text{GeV}/p_T^e)$ of the axis of any surviving jet are removed, as they are likely to originate from semi-leptonic b- or c-hadron decays. If a jet is reconstructed within $\Delta R = 0.2$ of a muon and the jet has fewer than three associated tracks or the muon energy constitutes most of the jet energy then the jet is removed. Muons reconstructed within a cone of size $\Delta R = \min(0.4, 0.04 + 10\ \text{GeV}/p_T^{\mu})$ around the jet axis of any surviving jet are removed. Finally, jets that are closer than $\Delta R = 0.2$ to a hadronically decaying τ-lepton are removed. This last requirement justifies the identification of hadronically decaying τ-leptons in the analysis even though they are disregarded in the event selection, as it improves slightly the consistency of the background composition between the 0- and 1-lepton channels for some processes. As will be discussed below, the events are categorised according to the number of jets. As an example, let us consider how a $W(\to \tau\nu)$ + 2-jets event where the τ-lepton decays into hadrons may enter the 0-lepton channel selection. If the overlap removal procedure between reconstructed τ-leptons and jets is not performed the event will be classifed in the 3-jet category, while it will be correctly classified in the 2-jet category when the procedure is applied. This improves the consistency with the 1-lepton channel, where a $W(\to e/\mu\nu)$ + 2-jets event with similar kinematics will always be classified in the 2-jet category.

2.3.2 Event selection and categorisation

The orthogonality between the channels is ensured by the categorisation of the events into the 0-, 1- and 2-lepton channels depending on the number of selected *loose* electrons and muons, to target the $ZH \rightarrow \nu\nu b\bar{b}$, $WH \rightarrow \ell\nu b\bar{b}$ and $ZH \rightarrow \ell\ell b\bar{b}$ signatures, respectively. In all channels, the events are required to have exactly two b-tagged jets, which form the Higgs boson candidate. At least one of those jets should have $p_{\mathrm{T}} > 45\,\mathrm{GeV}$. Events are then categorised as being 2-jet or 3-jet depending on whether additional, untagged jets are present. In the 0- and 1-lepton channels, only one such additional jet is allowed: the $t\bar{t}$ background becomes overwhelming in events with four jets or more since it is the typical final state for a semi-leptonic $t\bar{t}$ decays. In the 2-lepton channel, where the typical final state for a dileptonic $t\bar{t}$ decay is in the 2-jet category, the signal-to-background ratio does not degrade with additional jets, so any number of additional untagged jets is allowed.

It has been mentioned already that the transverse momentum of the vector boson p_{T}^{V} is one of the key kinematic variables in the analysis. It is reconstructed as the $E_{\mathrm{T}}^{\mathrm{miss}}$ in the 0-lepton channel, as the vector sum of $\mathbf{E}_{\mathrm{T}}^{\mathrm{miss}}$ and of the charged-lepton transverse momentum in the 1-lepton channel, and as the transverse momentum of the dilepton system in the 2-lepton channel. As shown on fig. 2.3, the signal-to-background ratio increases at large vector boson transverse momenta. This makes clear why the analysis is focused on a high-p_{T}^{V} region defined as $p_{\mathrm{T}}^{V} > 150\,\mathrm{GeV}$. In the 2-lepton channel, the sensitivity in the medium-p_{T}^{V} region $75\,\mathrm{GeV} < p_{\mathrm{T}}^{V} < 150\,\mathrm{GeV}$ is large enough to justify adding it to the analysis. In the 1-lepton channel, Yanhui Ma showed that the addition of this medium-p_{T}^{V} region could bring an extra 8% sensitivity [135], but at the cost of an increased complexity of the background uncertainty model in the profile likelihood fit to accommodate the presence of this very high statistics, low signal-to-background ratio region. Because of this additional effort required, it was decided not to include the medium-p_{T}^{V} region in the 1-lepton channel.

In addition to the common event selections discussed above, specific selections are applied in each channel to improve the sensitivity of the analysis.

0-lepton channel

The online event selection uses $E_{\mathrm{T}}^{\mathrm{miss}}$ triggers, with thresholds that varied with the increase in instantaneous luminosity, starting at 70 GeV for the 2015 data-taking period, and up to 90 GeV then 110 GeV for 2016 and 2017 data-taking. Compared to an offline $E_{\mathrm{T}}^{\mathrm{miss}}$ threshold at 150 GeV, the $E_{\mathrm{T}}^{\mathrm{miss}}$ triggers are fully efficient for$E_{\mathrm{T}}^{\mathrm{miss}} > 180\,\mathrm{GeV}$, and have an efficiency of 85 – 90% at $E_{\mathrm{T}}^{\mathrm{miss}} = 150\,\mathrm{GeV}$. Their efficiency was measured in $W+$jets, $Z+$jets and $t\bar{t}$ events in data using single-muon triggers, resulting in correction factors applied in simulation ranging from 1.05 at 150 GeV, to 1 above 200 GeV. To remove a small part of the phase space where the trigger efficiency depends mildly on the jet multiplicity, a requirement on the scalar sum of the transverse momenta of the jets H_{T} is applied, with a threshold $H_{\mathrm{T}} > 120\,\mathrm{GeV}$ for 2-jet events, and $H_{\mathrm{T}} > 150\,\mathrm{GeV}$ for 3-jet events.

As expected from a 0-lepton channel, any event with a *loose* lepton is rejected. The use of *loose* leptons for the veto limits the contamination by $W+$jets and $t\bar{t}$ backgrounds. The majority of such events entering the 0-lepton selection are $W \rightarrow \tau\nu$ decays, with either hadronic τ-lepton decays, or leptonic decays where the daughter electron or muon does not pass the *loose* selection. This acceptance for $W \rightarrow \tau\nu$ events also means that some WH events pass the 0-lepton selection, accounting for about 20% of the signal in the 0-lepton channel.

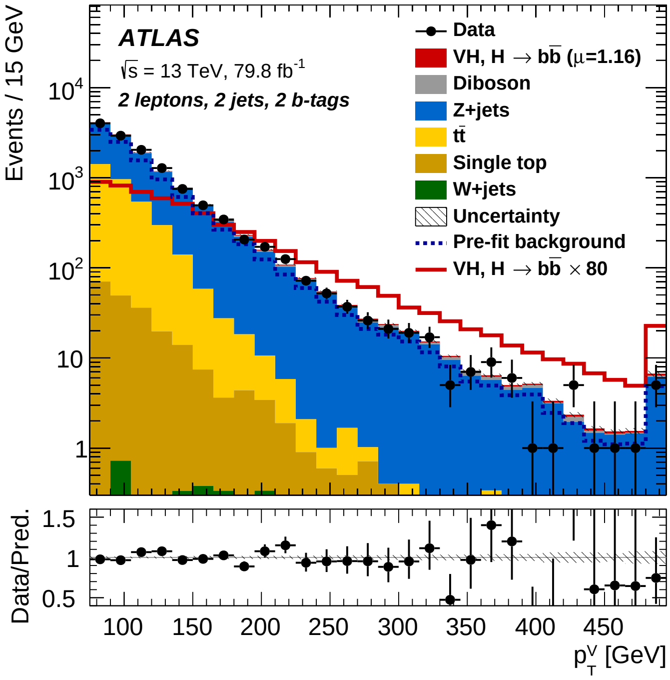

Figure 2.3: Reconstructed vector boson transverse momentum distribution in the 2-lepton channel, 2-jet category, after the profile likelihood fit to the data. The fitted signal multiplied by a factor of 80 is displayed as a red line, and has a harder spectrum than the backgrounds shown as solid colours.

In an event topology with only jets and $E_{\mathrm{T}}^{\mathrm{miss}}$ sizable multi-jet contamination can be expected, coming from beam background, and mostly from mismeasured jets in the calorimeters. However, the kinematics of such events can be easily separated from that of the signal events: instead of the typical two b-tagged jets close to each other and balanced against the $E_{\mathrm{T}}^{\mathrm{miss}}$, multi-jet events tend to have relatively back-to-back jets, with the $E_{\mathrm{T}}^{\mathrm{miss}}$ being aligned with one of them. This leads to the following selections, whose optimization is described in David Delgove's and Charles Delporte's theses [130, 152]:

- $\Delta\phi(\mathbf{E}_{\mathrm{T}}^{\mathrm{miss}}, \mathbf{p}_{\mathrm{T}}^{\mathrm{miss}}) < 90^\circ$,
- $\Delta\phi(\mathbf{b}_1, \mathbf{b}_2) < 140^\circ$,
- $\Delta\phi(\mathbf{E}_{\mathrm{T}}^{\mathrm{miss}}, \mathbf{bb}) > 120^\circ$,
- $\min[\Delta\phi(\mathbf{E}_{\mathrm{T}}^{\mathrm{miss}}, \mathbf{jets})] > 20^\circ$ for 2-jet events, $> 30^\circ$ for 3-jet events.

In these expressions, $\mathbf{b}_1$ and $\mathbf{b}_2$ are the four-momenta of the two b-tagged jets forming the Higgs boson candidate's dijet system **bb**, and $\mathbf{p}_{\mathrm{T}}^{\mathrm{miss}}$ is the missing transverse momentum computed from the negative sum of the transverse momenta of the inner detector tracks matched to the primary vertex.

1-lepton channel

In the electron sub-channel, the online selection uses a logical OR of single-electron triggers with p_{T} thresholds starting at 24 GeV in 2015, and increased to 26 GeV in 2016 and 2017. The lowest-threshold triggers include identification and isolation criteria looser than those used in the offline analysis, and that are removed or relaxed for the higher-threshold triggers. In the muon sub-channel, the same $E_{\mathrm{T}}^{\mathrm{miss}}$ triggers and corrections factors as in the 0-lepton channel are used. Since muons are not included in the $E_{\mathrm{T}}^{\mathrm{miss}}$ calculation at trigger level, $E_{\mathrm{T}}^{\mathrm{miss}}$ triggers are effectively p_{T}^{V} triggers in this sub-channel. That allows an overall trigger efficiency of about 98% with respect to the offline selection, compared to about 80% efficiency if single-muon triggers were used, due to the limited coverage of the muon trigger chambers in the central region of the detector.

The offline selection consists in requiring exactly one *tight* lepton and no additional *loose* leptons, with p_{T} thresholds of 27 GeV for the electrons and 25 GeV for the muons. The more stringent identification and isolation requirements in the *tight* lepton selections, combined with an additional selection of $E_{\mathrm{T}}^{\mathrm{miss}} > 30\,\mathrm{GeV}$ in the electron sub-channel, allow to reduce significantly the multi-jet background which in this channel comes mostly from misidentified hadrons and from poorly isolated leptons from heavy flavour hadrons decays.

Events in the 1-lepton channel are categorised into the signal region (SR) or into a control region enriched in $W+\mathrm{hf}$ events ($W+\mathrm{hf}$ CR). The control region is made of events passing the selection criteria $m_{bb} < 75\,\mathrm{GeV}$ and $m_{\mathrm{top}} > 225\,\mathrm{GeV}$, where m_{bb} is the invariant mass of the b-tagged jets, and m_{top} is the reconstructed mass of a leptonically-decaying top-quark candidate. The calculation of the latter requires the estimation of the four-momentum of the neutrino, achieved by the identification of its transverse component to the $E_{\mathrm{T}}^{\mathrm{miss}}$, and by the determination of its longitudinal component by a constraint of the lepton-neutrino system to the W mass. This estimation has usually two solutions, and m_{top} is then calculated as the invariant mass of the lepton, the reconstructed neutrino and the b-tagged jet that yields the lowest value among the four possibilities. The purity of the resulting $W+\mathrm{hf}$ control region is around 75%.

2-lepton channel

The online selection in the electron sub-channel is the same as in the 1-lepton channel. In the muon sub-channel, a logical OR of single-muon triggers is used, with p_{T} thresholds for the lowest ones ranging from 20 GeV to 26 GeV depending on the data-taking periods. Similarly to the electron triggers, the lowest-threshold ones include an isolation requirement that is removed for the higher-thresholds. The trigger efficiency with respect to the offline selection is close to 100% in the electron channel, while it is about 90% in the muon channel.

Events with exactly two *loose* leptons are selected. The lepton that triggered the event is required to have $p_{\mathrm{T}} > 27\,\mathrm{GeV}$ to ensure that the trigger efficiency reaches its plateau. In dimuon events, the two muons should have opposite-sign charge. This selection is not done in the electron sub-channel, where it would decrease a little the acceptance since the charge misidentification is not negligible. The dilepton invariant mass is required to be compatible with that of the Z boson: $81\,\mathrm{GeV} < m_{\ell\ell} < 101\,\mathrm{GeV}$. This reduces significantly the backgrounds without a resonant lepton pair, such as top-quark and multi-jet productions.

Events in the 2-lepton channel are categorised into a signal region (SR) if the two leptons are of the same flavour, or into a control region if they have one electron and one muon ($e\mu$ CR). This defines a control region 99% pure in $t\bar{t}$ and single-top-quark events, whose kinematics are identical to those in the signal region.

The event selection and categorisation in the three channels is summarised in table 2.2. The acceptances in the three channels after full selection, as well as predicted cross-sections times branching fractions for $(W/Z)H$ with $W \to \ell\nu$, $Z \to \ell\ell$, $Z \to \nu\nu$ and $H \to b\bar{b}$ are given in table 2.3. As already mentioned, the non-negligible acceptance for the $qq \to WH$ process in the 0-lepton channel is mostly due to hadronically-decaying τ-leptons produced in the W decays. The larger,

Table 2.2: Summary of the event selection and categorisation in the 0-, 1- and 2-lepton channels.

Selection	0-lepton	1-lepton e sub-channel	 μ sub-channel	2-lepton
Trigger	$E_{\mathrm{T}}^{\mathrm{miss}}$	Single lepton	$E_{\mathrm{T}}^{\mathrm{miss}}$	Single lepton
Leptons	0 *loose* leptons with $p_{\mathrm{T}} > 7$ GeV	1 *tight* electron $p_{\mathrm{T}} > 27$ GeV	1 *tight* muon $p_{\mathrm{T}} > 25$ GeV	2 *loose* leptons with $p_{\mathrm{T}} > 7$ GeV ≥ 1 lepton with $p_{\mathrm{T}} > 27$ GeV
$E_{\mathrm{T}}^{\mathrm{miss}}$	> 150 GeV	> 30 GeV	–	–
$m_{\ell\ell}$	–	–		81 GeV < $m_{\ell\ell}$ < 101 GeV
Jets	Exactly 2 / Exactly 3 jets			Exactly 2 / ≥ 3 jets
Jet p_{T}	> 20 GeV for $\lvert\eta\rvert < 2.5$ > 30 GeV for $2.5 < \lvert\eta\rvert < 4.5$			
b-jets	Exactly 2 b-tagged jets			
Leading b-tagged jet p_{T}	> 45 GeV			
H_{T}	> 120 GeV (2 jets), >150 GeV (3 jets)	–		–
$\min[\Delta\phi(\mathbf{E}_{\mathrm{T}}^{\mathrm{miss}}, \mathbf{jets})]$	> 20° (2 jets), > 30° (3 jets)	–		–
$\Delta\phi(\mathbf{E}_{\mathrm{T}}^{\mathrm{miss}}, \mathbf{bb})$	> 120°	–		–
$\Delta\phi(\mathbf{b}_1, \mathbf{b}_2)$	< 140°	–		–
$\Delta\phi(\mathbf{E}_{\mathrm{T}}^{\mathrm{miss}}, \mathbf{p}_{\mathrm{T}}^{\mathrm{miss}})$	< 90°	–		–
p_{T}^{V} regions	> 150 GeV			75 GeV < p_{T}^{V} < 150 GeV, > 150 GeV
Signal regions	–	$m_{bb} \geq 75$ GeV or $m_{\mathrm{top}} \leq 225$ GeV		Same-flavour leptons Opposite-sign charges ($\mu\mu$ sub-channel)
Control regions	–	$m_{bb} < 75$ GeV and $m_{\mathrm{top}} > 225$ GeV		Different-flavour leptons Opposite-sign charges

Table 2.3: The cross-section (σ) times branching fraction ($\mathscr{B}$) and acceptance for the three channels at $\sqrt{s}$ = 13 TeV. The qq- and gg-initiated ZH processes are shown separately. The branching fractions are calculated considering only decays into muons and electrons for $Z \to \ell\ell$, decays into all three lepton flavours for $W \to \ell\nu$ and decays into all neutrino flavours for $Z \to \nu\nu$. The acceptance is calculated as the fraction of events remaining in the combined signal and control regions after the full event selection.

Process	$\sigma \times \mathscr{B}$ [fb]	Acceptance [%]		
		0-lepton	1-lepton	2-lepton
$qq \to ZH \to \ell\ell b\bar{b}$	29.9	<0.1	0.1	6.0
$gg \to ZH \to \ell\ell b\bar{b}$	4.8	<0.1	0.2	13.5
$qq \to WH \to \ell\nu b\bar{b}$	269.0	0.2	1.0	–
$qq \to ZH \to \nu\nu b\bar{b}$	89.1	1.9	–	–
$gg \to ZH \to \nu\nu b\bar{b}$	14.3	3.5	–	–

almost double acceptance for $gg \to ZH$ events compared to the $qq \to ZH$ process is due to the harder p_{T}^{V} spectrum combined with the $p_{\mathrm{T}}^{V} > 75\,\mathrm{GeV}$ or $p_{\mathrm{T}}^{V} > 150\,\mathrm{GeV}$ selection in the 2-lepton or 0-lepton channel, respectively. The much larger acceptance in the 2-lepton channel compared to the other channels is due to the inclusion of the medium-p_{T}^{V} region.

2.3.3 Channels with tau leptons

Since hadronically decaying τ-leptons are identified in the analysis as part of the objets selections, it may seem surprising that they are not used further in the event selection to gain sensitivity to $WH \to \tau\nu b\bar{b}$ and $ZH \to \tau^+\tau^- b\bar{b}$ decays. The different cases were studied and concluded that the expected sensitivity increase was not high enough to justify the added complexity to the analysis.

$WH \to \tau\nu b\bar{b}$ events

It can be deduced from table 2.3 that about 20% of the signal events in the 0-lepton channel come from WH events, the vast majority of them with τ-leptons. In his thesis, Charles Deporte [130] attempted to classify these events seperately from the rest of the 0-lepton selection by using the selected hadronically-decaying τ-leptons. Unfortunately the acceptance and efficiency of the τ reconstruction was not high enough for this classification to yield any sizable sensitivity improvement in this channel.

The 1-lepton channel selection has a sizable acceptance for leptonically-decaying τ-leptons, although it is limited by the fact that the resulting muons or electrons are softer and may not pass the 1-lepton channel transverse momentum selection. An explicit selection of events with hadronically-decaying τ-leptons has been attempted by Yanhui Ma in his thesis [135]. As the 0-lepton channel has some acceptance to these events, the starting point is a selection of events containing a reconstructed hadronically-decaying τ-lepton candidate, not passing the 0-lepton channel selection, and passing the lowest unprescaled triggers with the $E_{\mathrm{T}}^{\mathrm{miss}}$, or $E_{\mathrm{T}}^{\mathrm{miss}} + \tau_{had}$, or τ_{had} signatures. Without any additional selection (that would be necessary to reduce the multi-jet contribution in this signature), the number of simulated signal events passing these trigger and τ-lepton selections amount to only 4% of the number of signal events selected in the 1-electron or 1-muon subchannels. The small sensitivity improvement to be expected after this preliminary study did not justify the continuation of the work to create a dedicated 1-τ subchannel.

Yanhui Ma also studied the possibility to veto events passing the 1-lepton selection when they have a reconstructed hadronically-decaying τ-lepton in addition to the selected electron or muon. Such a veto results in a negligible efficiency loss for the signal and removes 20% of the $t\bar{t}$ events in the 2-jet category, as it allows to veto topologies where one of the W bosons decay into an electron or a muon, and the other W boson decays into a τ-lepton. However, upon studying the distribution of the multivariate discriminating variable used in the analysis for these events, it appeared they are mostly in the low-BDT score, low-sensitivity part. In the high-sensitivity part of the distribution, the $t\bar{t}$ background was reduced by only a few percents. The gain in sensitivity was therefore negligible, and did not justify the complexity of this additional veto.

$ZH \rightarrow \tau^+\tau^- b\bar{b}$ events

The possibility to add selections dedicated to the $ZH \rightarrow \tau^+\tau^- b\bar{b}$ events was studied by Tasneem Saleem in her thesis [153].

The case where both τ-leptons decay hadronically was studied by selecting events with at least two reconstructed hadronically-decaying τ-leptons and no other charged lepton. The events were considered if they did not already pass the 0-lepton selection, have $p_{\mathrm{T}}^{Z} > 150\,\mathrm{GeV}$, and pass a combination of single-τ, di-τ and $\tau + E_{\mathrm{T}}^{\mathrm{miss}}$ triggers. Because of the much worse trigger performance, and of the worse τ-lepton selection efficiency compared to the muon and electron efficiencies, the signal events thus selected amount to less than 1.5% of the yields in the electron and muon subchannels in the $p_{\mathrm{T}}^{Z} > 150\,\mathrm{GeV}$ region.

The semi-leptonic case uses the same lepton selection as in the 1-lepton channel to look for the leptonically-decaying τ-lepton, and requires at least one additional reconstructed hadronic τ-lepton decay. A combination of single-lepton, single-τ, $\tau + E_{\mathrm{T}}^{\mathrm{miss}}$ and $E_{\mathrm{T}}^{\mathrm{miss}}$ triggers is used. Events already entering the standard 1-lepton selection are vetoed. This results in expected signal yields of around 2% of those in the standard 2-lepton selection, in both the $75\,\mathrm{GeV} < p_{\mathrm{T}}^{Z} < 150\,\mathrm{GeV}$ and the $p_{\mathrm{T}}^{Z} > 150\,\mathrm{GeV}$ regions.

The dileptonic case where both τ-leptons decay into an electron or a muon has the smallest branching fraction (12.4%), with usually relatively soft leptons. Given the very low signal yields selected in the other cases despite their larger branching fraction, this dileptonic case was not investigated further.

Overall, the expected signal yields from dedicated $ZH \rightarrow \tau^+\tau^- b\bar{b}$ selections are only a few percents of those in the standard 2-lepton selection. As channels with τ-leptons tend to have significant background contributions from multi-jet events faking the τ-leptons in addition to the Z boson and top backgrounds already present in the 2-lepton channel, the sensitivity increase to be expected from these selections can only be at the percent level. The preliminary studies discussed above were therefore not continued further.

2.3.4 Multivariate analysis

As mentioned previously, the main version of the analysis makes use of multivariate discriminants as final discriminating variables, in the form of boosted decision trees (BDTs). They are constructed, trained and evaluated in eight signal regions, corresponding to the two jet categories in the three lepton channels in the high-p_{T}^{V} region, in addition to the two jet categories in the 2-lepton medium-p_{T}^{V} region. Two sets of BDTs using the same input variables and parameters are constructed. The nominal one is designed to separate the Higgs boson events from the sum of expected background processes, and is referred to as BDT_{VH}. As mentioned previously, the second one is used to validate the analysis by separating the $VZ, Z \rightarrow b\bar{b}$ diboson process from the sum of all other expected background processes, including VH. It is referred to as BDT_{VZ}.

The input variables used for the BDTs are chosen independently in each lepton channel, as the result of an optimization process to maximise the separation between the signal and backgrounds in the BDT_{VH}. Details of this optimization can for instance be found in Charles Delporte's thesis for the 0-lepton channel [130]. Starting from the dijet mass (m_{bb}), additional variables describing the event kinematics are tried one at a time by re-training the BDT in each case. The variable yielding the highest statistics-only significance is selected and added to the list. This procedure is iterated until the remaining variables yield only negligible increase of the sensitivity. As expected, the most useful variables for the signal discrimination in the $VH(b\bar{b})$ topologies are the dijet mass m_{bb}, the angular separation between the jets , and the transverse momentum of the vector boson. The most dramatic case is in the 0-lepton 2-jet category, where the very simple final state (two b-jets and missing transverse energy) leads to 95% of the full sensitivity being achieved by using only m_{bb} and $\Delta R(\mathbf{b}_1, \mathbf{b}_2)$.

The lists of variables selected in each lepton channel are displayed in table 2.4. Depending on the channels, eight to thirteen input variables are used. Among the b-tagged jets, the leading one is labelled b_1 and the subleading one is labelled b_2. The separation in pseudorapidity between the b-tagged jets is $|\Delta\eta(\mathbf{b}_1, \mathbf{b}_2)|$. The azimuthal angle and the separation in pseudorapidity between the reconstructed vector boson and the dijet system are noted $\Delta\phi(\mathbf{V}, \mathbf{bb})$ and $|\Delta\eta(\mathbf{V}, \mathbf{bb})|$, respectively. In the 0-lepton channel, m_{eff} is defined as the scalar sum of the transverse momenta of all jets and $E_{\mathrm{T}}^{\mathrm{miss}}$. In the 1-lepton channel, $\min[\Delta\phi(\ell, \mathbf{b})]$ is the angle between the lepton and the closest b-tagged jet, m_{T}^{W} is the transverse mass of the reconstructed W boson, m_{top} is the reconstructed mass of a leptonically-decaying top-quark candidate as described in section 2.3.2, and $|\Delta Y(\mathbf{V}, \mathbf{bb})|$ is the rapidity difference between the W and Higgs boson candidates. The latter is calculated by using the same reconstruction of the W boson candidate four-momentum as for m_{top}. In the 2-lepton channel, $m_{\ell\ell}$ is the dilepton mass, and S_{T} is the scalar sum of transverse momenta of the charged leptons and jets in the event. In 3-jet events, the third jet is labelled jet_3 and the mass of the 3-jet system is noted m_{bbj}.

The technical implementation of the BDTs relies on the Tookit for Multivariate Data Analysis (TMVA) [154]. The hyperparameters had been thoroughly optimized using scans in the analysis of the Run 1 data [51], and their tuning was found still acceptable for the Run 2 analysis, where few values were changed [130]. The performance and robustness of the BDTs is improved by the use of a k-folding technique with two folds. For each BDT, the simulated Monte Carlo events in the corresponding analysis region are split randomly into two halves, A and B. The performance of the BDT trained on sample A (B) is evaluated with sample B (A) in order to use independent events for the training and the evaluation, while still making use of all the available Monte Carlo statistics. When applying the BDTs to data events, the fold A or B is chosen randomly. The output distributions of the BDTs evaluated on samples B and A are then merged into a single distribution. The performance of the BDTs depends strongly on the availability of large datasets of MC events to perform the training, an issue quite common when using machine learning techniques. The amount of events available is increased by removing the b-tagging requirements in the training of the BDTs, and using instead for all events the jet weighting technique described in section 2.3.1 for backgrounds with only c- and light-jets. As the analysis uses a b-tagging operating point with 70% efficiency on b-jets, the number of events is therefore increased by at least a factor two for both signal and backgrounds.

Table 2.4: Variables used for the multivariate discriminant in each of the categories.

Variable	0-lepton	1-lepton	2-lepton
p_{T}^{V}	$\equiv E_{\mathrm{T}}^{\mathrm{miss}}$	×	×
$E_{\mathrm{T}}^{\mathrm{miss}}$	×	×	
$p_{\mathrm{T}}^{b_1}$	×	×	×
$p_{\mathrm{T}}^{b_2}$	×	×	×
m_{bb}	×	×	×
$\Delta R(\mathbf{b_1},\mathbf{b_2})$	×	×	×
$\|\Delta\eta(\mathbf{b_1},\mathbf{b_2})\|$	×		
$\Delta\phi(\mathbf{V},\mathbf{bb})$	×	×	×
$\|\Delta\eta(\mathbf{V},\mathbf{bb})\|$			×
m_{eff}	×		
$\min[\Delta\phi(\ell,\mathbf{b})]$		×	
m_{T}^{W}		×	
m_{top}		×	
$\|\Delta Y(\mathbf{V},\mathbf{bb})\|$		×	
$m_{\ell\ell}$			×
$E_{\mathrm{T}}^{\mathrm{miss}}/\sqrt{S_{\mathrm{T}}}$			×
	Only in 3-jet events		
$p_{\mathrm{T}}^{\mathrm{jet_3}}$	×	×	×
m_{bbj}	×	×	×

2.3.5 Dijet-mass analysis

The main multivariate analysis is further cross-checked by using the invariant mass of the two b-tagged jets as the discriminating variable. As the dijet mass is only one of the variables entering the BDTs, the sensitivity of this method is significantly improved by imposing additional selections, shown in table 2.5, on top of the ones used for the multivariate analysis. Details on their optimisation for the analysis of the Run 2 data can be found in David Delgove's and Yanhui Ma's theses [135, 152].

In the 1-lepton channel, the fraction of the $t\bar{t}$ background where both W bosons decay into leptons is efficiently reduced using a selection on the transverse mass of the reconstructed W boson candidate, since the presence of two neutrinos can yield a large value. In the 2-lepton channel, a selection is applied on $E_{\mathrm{T}}^{\mathrm{miss}}/\sqrt{S_{\mathrm{T}}}$, which can be seen as an approximation of a significance of the $E_{\mathrm{T}}^{\mathrm{miss}}$ and therefore reduces the $t\bar{t}$ background.

The main improvement in sensitivity for this cross-check comes from making use of the most discriminant kinematic variables besides m_{bb}, by splitting the high-p_{T}^{V} region into two regions $150\,\mathrm{GeV} < p_{\mathrm{T}}^{V} < 200\,\mathrm{GeV}$ and $p_{\mathrm{T}}^{V} > 200\,\mathrm{GeV}$, and by applying a selection on the angular separation between the b-tagged jets optimised in each p_{T}^{V} region.

In the 1-lepton channel, the low mass range of the dijet mass distribution brings enough information to sufficiently constrain the $W+\mathrm{hf}$ background, thus the categorisation of the events into the $W+\mathrm{hf}$ CR is not applied and they are kept in the SR.

Table 2.5: Summary of the event selection criteria in the 0-, 1- and 2-lepton channels for the dijet-mass analysis, applied in addition to those described in Table 2.2 for the multivariate analysis.

	Channel		
Selection	0-lepton	1-lepton	2-lepton
m_T^W	-	< 120 GeV	-
$E_T^{miss} / \sqrt{S_T}$	-	-	$< 3.5\sqrt{\text{GeV}}$

	p_T^V regions		
p_T^V	$75 - 150$ GeV (2-lepton only)	$150 - 200$ GeV	> 200 GeV
$\Delta R(\mathbf{b}_1, \mathbf{b}_2)$	<3.0	<1.8	<1.2

2.4 Estimation of the multi-jet background

The backgrounds simulated using MC samples and presented in section 2.2.2 all involve W or Z bosons, and are referred to as electroweak (EW) backgrounds hereafter. But pure multi-jet backgrounds can also enter the analysis phase space, due to fake E_T^{miss}, or misidentified or non-prompt leptons. Because of the large cross-section and large rejection factor of multi-jet processes, and because of the possible inaccuracies of the simulation of the fake E_T^{miss} or misidentified leptons in the tails of multi-jet distributions, data-driven methods are used in each channel to estimate the contribution of this background.

2.4.1 Estimation in the 0-lepton channel

In the 0-lepton channel, the multi-jet background is mostly due to fake E_T^{miss} arising from fluctuation in the energy deposition of a jet in the calorimeters. It is then expected that the resulting E_T^{miss} is close to the direction of the jet. Indeed, the $\min[\Delta\phi(\mathbf{E}_T^{miss}, \mathbf{jets})]$ variable introduced in section 2.3.2 is extremely effective at reducing this background contribution, as can be seen in fig. 2.4 where the selection on this variable is removed in the 3-jet category. The optimization of the selections aiming at reducing the multi-jet background is discussed in the theses of David Delgove [152] and Charles Delporte [130]. The selection values were precisely tuned to reduce the multi-jet background down to negligible levels, at a minimal cost for the signal efficiency. In the 3-jet category, a fit to the $\min[\Delta\phi(\mathbf{E}_T^{miss}, \mathbf{jets})]$ distribution is performed to extract the multi-jet contribution. The $t\bar{t}$ and $Z+$jets distributions are taken from the Monte Carlo, with their normalisations allowed to float, while the multi-jet distribution is parameterised with a falling exponential, whose parameter and normalisation are determined in the fit. In the analysis of the first 36 fb^{-1} of Run-2 data [53], the multi-jet was then estimated to be less than 0.2% of the total background, and around 10% of the signal contribution in the $80\,\text{GeV} < m_{bb} < 160\,\text{GeV}$ mass window. The BDT distribution of the multi-jet was estimated by using the data at low $\min[\Delta\phi(\mathbf{E}_T^{miss}, \mathbf{jets})]$, and found to have a shape similar to the one of the sum of the EW backgrounds. The small multi-jet contribution can therefore be absorbed in the floating normalisation factors of the EW backgrounds in the global likelihood fit. In the 2-jet category, the selections are even more efficient at reducing the multi-jet contribution. An estimation of its contribution similar to the fit in the 3-jet category could not be made, as the other anti-multi-jet selections reduce it down to very small levels even in the low part of the $\min[\Delta\phi(\mathbf{E}_T^{miss}, \mathbf{jets})]$

distribution. Hence, the multi-jet production in the 0-lepton channel is small enough to be neglected in the global likelihood fit.

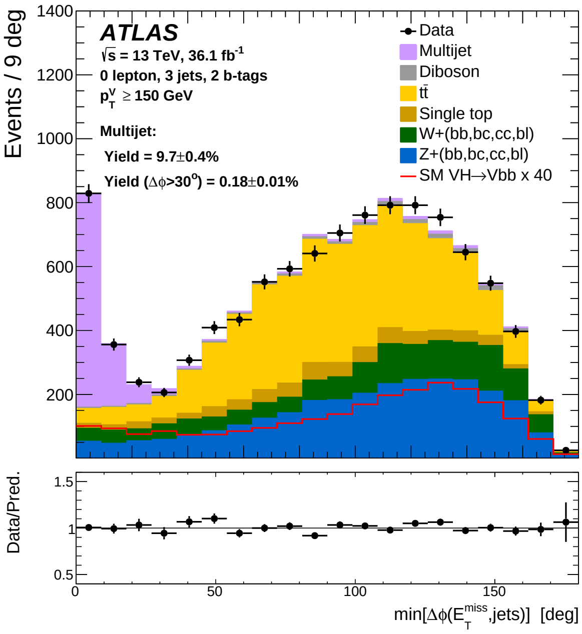

Figure 2.4: Distribution of min[$\Delta\phi(\mathbf{E}_{\mathrm{T}}^{\mathrm{miss}}, \mathbf{jets})$] in the 3-jet category of the 0-lepton channel, before any selection on this variable, on 36 fb^{-1} of Run-2 data [53]. The pink distribution is obtained using a Pythia 8 MC sample, scaled to the yield resulting from a fit assuming an exponential shape for the multi-jet contribution. The quoted multi-jet fractions are from the results of the fit (see text).

2.4.2 Estimation in the 1-lepton channel

In the 1-lepton channel, the multi-jet background comes mostly from leptons produced in decays of heavy-flavour hadrons, with smaller contributions arising from photon conversions, from misidentified hadrons (in the electron channel) or from decays in flight of strange particles (in the muon channel). While leptons produced in these ways tend to be poorly isolated, a small fraction, in the tails of the distributions, can pass the lepton isolation requirements and therefore enter the signal region of the analysis.

The procedure to estimate the multi-jet contribution and to obtain templates of multi-jet distributions is presented in detail in the theses of Yanhui Ma [135] and Tasneem Saleem [153] for the multivariate and dijet mass analyses, respectively. The estimation is performed separately in the electron and muon sub-channels, and in the 2- and 3-jet categories. In each category, the multi-jet yield is obtained in a template fit to the transverse mass of the W boson candidate, which was found to achieve the clearest discrimination between the multi-jet and the EW processes. While the templates for the EW backgrounds are obtained directly from the MC predictions, the template used for the multi-jet contribution has to be obtained from data, in a control region, after subtraction of the residual EW contribution. The control region has to be as pure as possible in multi-jet events, to be kinematically close to the signal region to avoid any significant bias, while being orthogonal to it. These criteria are met by inverting the isolation selection used in the *tight* lepton definition, while keeping all the rest of the nominal selection. However, the data statistics in this inverted isolation region are quite poor, therefore the number of required b-tagged jets is reduced from two to one to increase the precision on the template. All templates for multi-jet distributions, such as the shape of the BDT discriminant, or the transverse mass of the W boson candidate, are obtained by subtracting the remaining EW contribution to the data in this 1-b-tag, inverted isolation control region, whose purity in multi-jet ranges from 30% (muon sub-channel, 3-jet) to 70% (electron sub-channel, 2-jet). The m_{T}^{W} distributions of the dominant $W+$hf and $t\bar{t}$ backgrounds have different shapes, since di-leptonic $t\bar{t}$ decays create a larger tail. To limit any potential bias on the multi-jet yield, their normalisations are therefore floated independently, along with that of the multi-jet component. A better discrimination between the $t\bar{t}$ and $W+$hf backgrounds, and therefore more stable fit results, is achieved by a simultaneous fit of the m_{T}^{W} distribution in the SR and of the yield in the $W+$hf CR. The multi-jet is then found to amount to 1.9% (2.8%) of the total background in the electron (muon) sub-channel in the 2-jet category, while it is found to be 0.2% (0.4%) in the 3-jet category. These yields are used for the normalisation of the multi-jet component in all distributions. An illustration of the m_{T}^{W} template fit is displayed in fig. 2.5, coming from the first analysis of 36 fb^{-1}of Run-2 data [53] where a quite similar procedure was used (the extraction of the multi-jet template was slightly different). The separation of the multi-jet, the $W+$hf and the $t\bar{t}$ components offered by the use of the m_{T}^{W} distribution is quite visible: the multi-jet contribution peaks at low m_{T}^{W} values, and the $t\bar{t}$ background has large tails due to its dileptonic component.

The same procedure is applied in the dijet-mass analysis, with a few modifications pertaining to the template fit that determines the multi-jet normalisation. Because the dijet-mass analysis does not separate a $W+$hf control region, a first fit is performed on the $\Delta R(\mathbf{b}_1,\mathbf{b}_2)$ distribution, neglecting the multi-jet contribution, to fix the relative normalisations of the $W+$hf and $t\bar{t}$ samples. Their relative normalisation is then fixed in the template fit, while their overall normalisation is adjusted along with that of the multi-jet template. As the dijet-mass analysis has additional selections compared to the main multivariate analysis, the distribution of the azimuthal separation between the charged lepton and the $E_{\mathrm{T}}^{\mathrm{miss}}$ ($\Delta\phi(\ell,E_{\mathrm{T}}^{\mathrm{miss}})$) was found to yield a better-performing template fit than the m_{T}^{W} distribution.

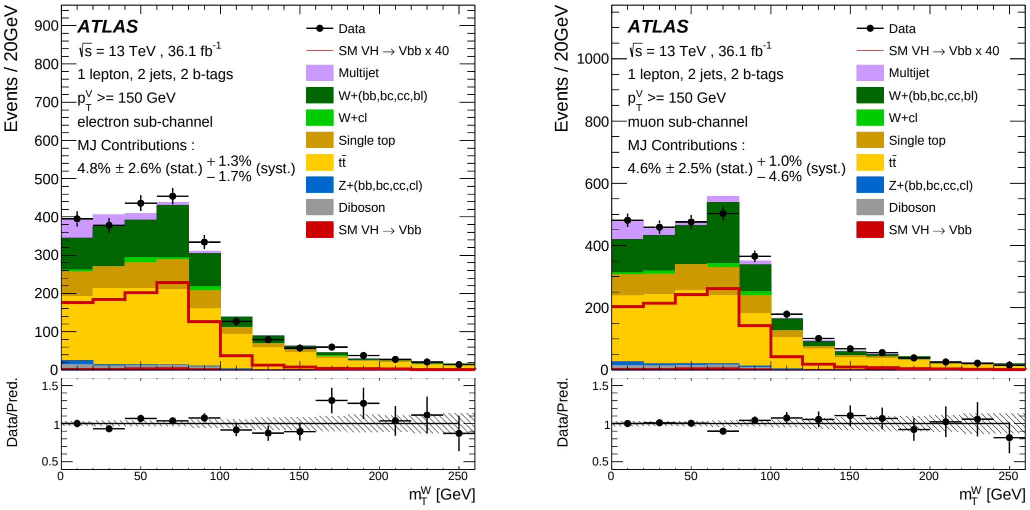

(a) **(b)**

Figure 2.5: Distribution of the transverse masse of the W boson candidate in the electron (a) and muon (b) sub-channels of the 1-lepton, 2-jet category, in the analysis of the first 36 fb^{-1} of Run-2 data [53].

The multi-jet estimates are subject to large systematic uncertainties, which are discussed in section 2.5.3.

2.4.3 Estimation in the 2-lepton channel

As expected from a topology with two isolated electrons or muons in the final state, the multi-jet background is very well suppressed in the 2-lepton channel. Its residual contribution was estimated in the analysis of the first 36 fb^{-1} of Run-2 data using a fit to the dilepton invariant mass distribution in a sample of events where the two lepton candidates have the same charge. The contribution from the EW backgrounds was taken from simulation, and the multi-jet distribution was assumed to have an exponential shape. The extrapolation of the result to the signal region assumed that the number of multi-jet events with same-charge and opposite-charge lepton candidates are equal. The multi-jet contribution to the total background was then estimated to be less than 0.2% in the electron channel, and much less than 0.1% in the muon channel. Similarly to the 0-lepton case, this background is therefore neglected in the global likelihood fit, where its small contribution is absorbed in the floating normalisations of the EW backgrounds.

2.5 Systematic uncertainties

As expected from an analysis with a quite low signal-to-background ratio, systematic uncertainties play a significant role in the *VH*$(b\bar{b})$ analysis. They must therefore be evaluated as accurately as possible, in order to provide an appropriate coverage of the true precision of the model used for the measurement. The use of a global profile likelihood analysis over the three channels is in particular more demanding in terms of background modelling. This will be discussed in section 2.5.2 below. The other sources of systematic uncertainties can be broadly classified into experimental uncertainties, those related to the multi-jet background estimation, and those related to the Higgs boson signal simulation.

2.5.1 Experimental uncertainties

The uncertainties pertaining to the physics objects reconstruction are determined centrally in specific analyses and then used globally in the physics measurements within the ATLAS collaboration. Uncertainties in selection efficiencies, energy scales and energy resolutions are then propagated to the *VH*$(b\bar{b})$ analysis phase space.

The dominant experimental uncertainties affecting the *VH*$(b\bar{b})$ measurement originate from the b-tagging efficiency correction factors, from the jet energy scale corrections, and from the modelling of the jet energy resolution.

The b-tagging correction factors applied to the simulated events to match the efficiencies measured in data are determined using $t\bar{t}$ events (for b- and c-jets) or multi-jet events (for light jets) [147, 155, 156]. The measurement of the b-jet efficiencies is performed using dileptonic $t\bar{t}$ decays, with a dilepton invariant mass selection that vetoes events in a window $80\,\text{GeV} < m_{\ell\ell} < 100\,\text{GeV}$ around the Z boson mass. This selection is therefore almost fully orthogonal to that of the 2-lepton channel. The b-tagging efficiency of c-jets is measured in fully reconstructed semi-leptonic $t\bar{t}$ decays, meaning that there must be at least four jets in the final state. The phase space of this analysis is therefore orthogonal to that of the 1-lepton channel. The correction factors resulting from the calibration analyses depend on jet p_{T} and $|\eta|$, and have uncertainties estimated from multiple sources. These uncertainties, which have various correlation patterns along p_{T} and $|\eta|$, are grouped and decomposed into uncorrelated components that are then treated independently. The components with the largest impact on the efficiencies are retained, resulting in three uncertainties for b-jets, three for c-jets, and five for light-flavour jets. The approximate size of the combined uncertainty in the tagging efficeincy is 2% for b-jets, 10% for c-jets and 40% for light-flavour jets. Additional uncertainties, with negligible impact on the analysis, are considered in the extrapolation of the b-jet efficiency calibration to jets with $p_{\mathrm{T}} > 300\,\mathrm{GeV}$, and in the misidentification of hadronically-decaying τ-leptons as b-jets.

The uncertainties in the jet energy scale and resolution are estimated in their respective measurements [142, 157]. The many uncertainty sources considered in the correction of the jet energy scale are decomposed into 23 uncorrelated components that are treated as independent. In addition, a specific uncertainty in the energy calibration of b- and c-jets is considered. The different sources considered for the jet energy resolution are grouped in a single uncertainty component.

Uncertainties are considered in the energy scale and resolution of the electrons and muons, as well as in their reconstruction, identification, isolation and trigger efficiencies. They are all estimated using 13 TeV data [137, 158], and are found to have a small impact on the result. The uncertainties in the energy scale and resolution of the jets and the leptons are propagated to the calculation of the $E_{\mathrm{T}}^{\mathrm{miss}}$, which also has additional uncertainties from the scale, resolution and reconstruction efficiency of the tracks used to compute the soft term [151], along with the modelling of the underlying event. Several sources of uncertainty are considered for the $E_{\mathrm{T}}^{\mathrm{miss}}$ trigger correction factors used in the 0-lepton and 1-muon channels, determined from the difference between the trigger efficiency in data and simulation: they account for the statistical uncertainty in the measured correction factors, and for differences between the correction factors determined from $W+$jets, $Z+$jets and $t\bar{t}$ events.

The uncertainty in the luminosity is 2.0% for the combined 2015–2017 data [159]. Based on the measurement of the visible cross-section in minimum-bias events [160], the average number of interactions per bunch crossing is rescaled by 3% to improve the agreement between simulation and data. An uncertainty as large as the correction is assigned.

2.5.2 Simulated background uncertainties

Background modelling uncertainties have a critical impact on the analysis given the low signal-to-background ratio over most of the phase space. Any insufficient coverage by the assigned uncertainties can lead to an artificially enhanced sensitivity, and biases in the measurement. Conversely, needlessly generous uncertainties may rapidly degrade the sensitivity. The difficulty to find an adequate set of uncertainties for the background model is further increased by the use of a global profile likelihood fit over the three channels. As the same background processes are present in the three channels, in similar but not quite the same phase spaces ($W+$jets in 0- and 1-lepton channels, $Z+$jets in 0- and 2-lepton channels, $t\bar{t}$ in all channels...), the acceptance differences that affect the relative normalisations between analysis regions with a common normalisation need to be properly covered. Similarly, uncertainties must be assigned to the transfer of background normalisations in control regions to the signal regions. Failure in controlling these acceptance uncertainties can again result in biases in the measurement.

The uncertainties on the simulated background samples are therefore classified in three areas: normalisations, acceptance differences, and the shape of the differential distributions of the most important kinematic variables. The data in the phase space of the analysis are sufficiently precise that the normalisations of the main backgrounds are left unconstrained (floated) in the global likelihood fit. The uncertainties associated to the normalisations of the other backgrounds are taken from the currently most accurate calculations that are detailed in table 2.1. The systematic uncertainties in the acceptance differences or in the shapes of the kinematic variables are obtained either from particle-level comparisons between nominal and alternative simulated samples using the RIVET framework [161], or from comparisons to data in control regions. Whenever possible, the particle-level simulations are cross-checked with detector-level simulations, and good agreement is found. The nominal and alternative simulated samples are always normalised to the same cross-section in order to estimate acceptance uncertainties. Shape uncertainties are derived in each of the analysis regions separately. All samples are normalised to a common value in that region, and when several alternative samples exist the uncertainty is taken from the one showing the largest shape deviation from the nominal sample. While the distributions of the BDT$_{VH}$ discriminant may in principle be quite complex as the BDTs are built from many input variables, it was found in practice that assigning shape uncertainties to the main m_{bb} and p_{T}^{V} variables is sufficient to cover these BDT$_{VH}$ shape variations.

V+ jets production

The V+ jets events are labelled according to the jet flavour labels of the b-tagged jets. The resulting event types are designed as $V+bb$, $V+bc$, $V+bl$, $V+cc$, $V+cl$, $V+ll$. Given the high purity achieved by the b-tagging algorithm, the $V+bb$ contribution is by far the largest one in all categories of the analysis. Conversely, the $V+cl$ and $V+ll$ contributions constitute less than 1% of the background, and the relevant diagrams for these processes are quite different from those involved in the four other components. Therefore only simple uncertainties in the normalisation of these two backgrounds are included. The main contributions ($V+bb$, $V+bc$, $V+bl$ and $V+cc$) are jointly called the V+ hf background, and have their overall normalisation freely adjusted in the global likelihood fit, separately in the 2-jet and 3-jet categories. Uncertainties are assigned in the composition of this V+ hf background, in the form of an uncertainty in the yield of $V+bc$, $V+bl$ or $V+cc$ with respect to the yield of $V+bb$. They are estimated separately in each lepton channel. Acceptance uncertainties are also estimated in the relative normalisations of the V+ hf background in different regions that share a common normalisation parameter. In the case of the Z+ hf background, this applies to the relative normalisation in the 0-lepton channel with respect to that in the 2-lepton channel. For the W+ hf background, this includes both the relative normalisation in the 0-lepton channel with respect to that in the 1-lepton channel, and the ratio of the event yield in the W+ hf control region to that in the signal region in the 1-lepton channel. Finally, uncertainties are also assigned to the shapes of the m_{bb} and p_{T}^{V} distributions.

With the exception of the shape uncertainties in the Z+ hf background, which are evaluated from comparisons with data in m_{bb} sidebands, all uncertainties in the V+ jets processes are estimated from comparisons of different Monte-Carlo generators setups. The nominal SHERPA 2.2.1 sample is therefore compared to systematic variations of itself, which differ by:

- The renormlisation scale, changed by factors of 0.5 and 2,
- the factorisation scale, changed by factors 0.5 and 2,
- the CKKW merging scale, from 30 GeV to 15 GeV,
- the parton-shower and resummation scale, changed by factors of 0.5 and 2.

In addition, an alternative sample is produced using MADGRAPH5_aMC@NLO v2.2.2 [162], with up to four partons at LO, and interfaced to PYTHIA 8.212, using the A14 tune together with the NNPDF2.3LO PDF set. All normalisation and acceptance uncertainties are calculated by adding in quadrature the differences between the nominal sample and the systematic variations, including the difference with the MADGRAPH5 sample. For shape uncertainties, the largest of the differences is taken. As scale variations are found to have a minor effect on the shapes of the distributions, the evaluation of the shape uncertainties relies in practice on the comparison with the nominal SHERPA and the MADGRAPH5_aMC@NLO sample.

The values of the uncertainties for the $Z+$jets and $W+$jets backgrounds are listed in table 2.6. Among these values, the 7% assigned to the relative normalisation uncertainty of $Z+$hf between the 0-lepton and the 2-lepton channels may seem a bit large, since a priori the uncertainty in the ratio $Z \to \ell\ell$ to $Z \to \nu\nu$ is tiny. The causes are found in a detailed investigation of the differences in the phase state selected in these two channels, which is presented in Charles Delporte's thesis. The main contribution actually coming from the p_{T}^{V} selection, as the 0-lepton channel is limited to $p_{\mathrm{T}}^{V} > 150$ GeV while the 2-lepton channel selects $p_{\mathrm{T}}^{V} > 75$ GeV. But more subtle effects also contribute. The acceptance for the jets is different, as the overlap removal with the leptons (see section 2.3.1) is present only in the 2-lepton channel. The acceptance for b-tagged jets is also not exactly the same, as the fit for the primary vertex is much more accurate in the 2-lepton channel due to the presence of the two high-quality tracks from the leptons. Finally, the acceptance for the charged leptons is constrained within $|\eta| < 2.5$ or $|\eta| < 2.7$, while there is no such angular selection for neutrinos.

$t\bar{t}$ production

The $t\bar{t}$ background is significantly present in the three lepton channels, but the regions of the phase space probed are different enough, that the $t\bar{t}$ background in the 2-lepton channel is considered independently from that in the 0- and 1-lepton channels (referred to as 0+1-lepton channel). Indeed in the 2-lepton channel the selection of two leptons and two b-tagged jets probes the bulk of the phase space for dileptonic $t\bar{t}$ decays (the $m_{\ell\ell}$ selection set aside), while in the 0+1-lepton channels a mix of dileptonic and semileptonic $t\bar{t}$ decays are probed, where one to several jets and possibly leptons are unreconstructed (the leptons being either electrons or muons out of the acceptance, or hadronically-decaying τ-leptons). An examination of the distributions of the transverse momenta of the top-quarks and of the top-quark pair at particle-level confirms that the regions of the phase space probed in the 0- and 1-lepton channels are very similar, while that probed in the 2-lepton channel is quite different.

In the 2-lepton channel, the overall $t\bar{t}$ normalisation is floated independently in the 2-jet and in the 3-jet categories, and is effectively determined in the respective $e\mu$ regions. In the 0+1-lepton channels, a different setup is used, with an overall free normalisation floated in the global likelihood fit, and an acceptance uncertainty in the relative normalisations of the 2-jet and 3-jet categories. In addition, similar acceptance uncertainties are considered in the normalisation ratios of the 0-lepton channel to the 1-lepton channel, and of the $W+$hf control region to the 1-lepton signal region. Uncertainties in the shapes of the m_{bb} and p_{T}^{V} distributions are also estimated separately in the 0+1- and 2-lepton channels.

These uncertainties are estimated from comparisons of the nominal sample generated using POWHEG-BOX with alternative samples: one with a different parton-shower algorithm (using HERWIG 7 [163, 164] instead of PYTHIA 8), and another with a different matrix-element generation (using MADGRAPH5_aMC@NLO instead of POWHEG-BOX). The uncertainties in the acceptance are estimated by adding the difference between the nominal and the alternative generators in quadrature. For the shape uncertainties, the largest difference is used. A summary of the uncertainties considered and the values of the acceptance uncertainties are given in table 2.6.

Single top-quark production

As mentioned in section 2.2.2, the single top-quark samples are normalised to the most accurate cross-sections predictions. Uncertainties associated to these predictions are used, that take into account variations of the renormalisation and factorisation scales, of α_S and of the PDFs. No other uncertainties are considered for the s-channel, whose contribution is negligible in all analysis regions. In the t- and Wt-channels, acceptance uncertainties are estimated, separately in the 2-jet and 3-jet categories. Shape uncertainties are also considered in the m_{bb} and p_{T}^{V} distributions. In the Wt-channel, the phase space probed when the two b-tagged jets are b-jets (a case named $Wt(bb)$) is very different from the case named Wt(other) where one of the b-tagged jets is not a b-jet (and therefore comes most probably from a W boson decay). Therefore both acceptance and shape uncertainties are estimated separately in the $Wt(bb)$ and Wt(other) cases.

The estimation of these uncertainties is performed in a similar way to that of the $t\bar{t}$ process, using alternative samples characterised by the use of another parton-shower generation algorithm (HERWIG instead of PYTHIA) or of another matrix-element generation (MADGRAPH5_AMC@NLO instead of POWHEG-BOX). In addition, in the Wt-channel the uncertainty related to the interference between the Wt and the $t\bar{t}$ production processes is assessed by using a diagram subtraction scheme instead of the nominal diagram removal scheme [108, 165]. This uncertainty in the interference effect is particularly important in the $Wt(bb)$ case. The values of the single top-quark uncertainties are shown in table 2.6.

Diboson production

The diboson background is composed of three distinct processes: WZ, WW and ZZ production. The requirement of two b-tagged jets almost completely eliminates the WW events ($< 0.1\%$ of the total background), therefore only a normalisation uncertainty is assigned to this process. The uncertainties in the normalisation, acceptance and shape of distributions for the sizable WZ and ZZ backgrounds are estimated using alternative samples. Systematic variations of the nominal SHERPA samples are used, with varied factorisation, renormalisation and resummation scales. Samples generated using POWHEG, with either PYTHIA 8 (with several tunes of the shower parameters) or HERWIG++ as parton-shower generators, are also considered.

Normalisation uncertainties are the result of the scale variations on the generated cross-section. The scale variations are also used to estimate acceptance uncertainties in the different jet categories using the Stewart-Tackmann method [92], resulting in an uncertainty that applies to ≥ 2-jet events, another one that applies to ≥ 3-jet events, and an additional one associated to the 4-jet events in the 0- and 1-lepton channels. The samples differing by their parton-shower generator or in their parton-shower tune are employed to estimate other acceptance uncertainties, one inclusive, and a second one restricted to the 3-jet category. Both scale variations and parton-shower differences are considered to estimate a relative acceptance uncertainty in the yields in the 0-lepton channel with respect to those of the 1-lepton channel (for the WZ process) and of the 2-lepton channel (for the ZZ process). Separate uncertainties in the shape of the m_{bb} and p_{T}^{V} distributions are estimated from the scale variations, from the comparison of parton-shower generators, and from the comparison of the SHERPA and POWHEG matrix-element generators. The latter is the dominant shape effect in most of the analysis regions, with changes of the order 10 – 20% to the shape of the m_{bb} distribution for values in the range 100 – 130 GeV. A summary of the uncertainties in the diboson backgrounds and the values of the normalisation and acceptance uncertainties are listed in table 2.7.

2.5.3 Multi-jet background uncertainties

The data-driven estimate of the multi-jet background in the 1-lepton channel is subject to large systematic uncertainties, which are studied in details in Yanhui Ma's and Tasneem Saleem's theses. The uncertainties aim to cover all assumptions that go into the multi-jet estimate, and result in

Table 2.6: Summary of the systematic uncertainties in the background modelling for $Z+$jets, $W+$jets, $t\bar{t}$, and single top-quark. An 'S' symbol is used when only a shape uncertainty is assessed. The regions for which the normalisations float independently are listed in brackets. Where the size of an acceptance systematic uncertainty varies between regions, a range is displayed.

$Z+$jets	
$Z+ll$ normalisation	18%
$Z+cl$ normalisation	23%
$Z+$hf normalisation	Floating (2-jet, 3-jet)
$Z+bl$-to-$Z+bb$ ratio	20 – 25%
$Z+bc$-to-$Z+bb$ ratio	30 – 40%
$Z+cc$-to-$Z+bb$ ratio	13 – 15%
0-to-2 lepton ratio	7%
m_{bb}, p_{T}^{V}	S
$W+$jets	
$W+ll$ normalisation	32%
$W+cl$ normalisation	37%
$W+$hf normalisation	Floating (2-jet, 3-jet)
$W+bl$-to-$W+bb$ ratio	26% (0-lepton) and 23% (1-lepton)
$W+bc$-to-$W+bb$ ratio	15% (0-lepton) and 30% (1-lepton)
$W+cc$-to-$W+bb$ ratio	10% (0-lepton) and 30% (1-lepton)
0-to-1 lepton ratio	5%
$W+$hf CR to SR ratio	10% (1-lepton)
m_{bb}, p_{T}^{V}	S
$t\bar{t}$ (all are uncorrelated between the 0+1- and 2-lepton channels)	
$t\bar{t}$ normalisation	Floating (0+1-lepton, 2-lepton 2-jet, 2-lepton 3-jet)
0-to-1 lepton ratio	8%
2-to-3-jet ratio	9% (0+1-lepton only)
$W+$HF CR to SR ratio	25%
m_{bb}, p_{T}^{V}	S
Single top-quark	
Cross-section	4.6% (s-channel), 4.4% (t-channel), 6.2% (Wt)
Acceptance 2-jet	17% (t-channel), 55% ($Wt(bb)$), 24% (Wt(other))
Acceptance 3-jet	20% (t-channel), 51% ($Wt(bb)$), 21% (Wt(other))
m_{bb}, p_{T}^{V}	S (t-channel, $Wt(bb)$, Wt(other))

Table 2.7: Summary of the systematic uncertainties in the background modelling for diboson production, and for the multi-jet estimation. An 'S' symbol is used when only a shape uncertainty is assessed and 'PS/UE' indicates parton shower/underlying event. When extracting the $(W/Z)Z$ diboson production signal yield, as the normalisations are unconstrained, the normalisation uncertainties are removed. Where the size of an acceptance systematic uncertainty varies between regions, a range is displayed.

ZZ	
Normalisation	20%
0-to-2 lepton ratio	6%
Acceptance from scale variations	10 – 18%
Acceptance from PS/UE variations for 2 or more jets	6%
Acceptance from PS/UE variations for 3 jets	7% (0-lepton), 3% (2-lepton)
m_{bb}, p_{T}^{V}, from scale variations	S (correlated with WZ uncertainties)
m_{bb}, p_{T}^{V}, from PS/UE variations	S (correlated with WZ uncertainties)
m_{bb}, from matrix-element variations	S (correlated with WZ uncertainties)
WZ	
Normalisation	26%
0-to-1 lepton ratio	11%
Acceptance from scale variations	13 – 21%
Acceptance from PS/UE variations for 2 or more jets	4%
Acceptance from PS/UE variations for 3 jets	11%
m_{bb}, p_{T}^{V}, from scale variations	S (correlated with ZZ uncertainties)
m_{bb}, p_{T}^{V}, from PS/UE variations	S (correlated with ZZ uncertainties)
m_{bb}, from matrix-element variations	S (correlated with ZZ uncertainties)
WW	
Normalisation	25%
Multi-jet (1-lepton)	
Normalisation	60 – 100% (2-jet), 90 – 140% (3-jet)
BDT template	S

either changes to the m_{T}^{W} distributions used in the multi-jet template fits, therefore impacting the extracted multi-jet normalisations, or changes to the multi-jet BDT distributions used in the global likelihood fit. Variations of the multi-jet templates are obtained by changing the definition of the multi-jet control region, either by tuning the isolation requirements to keep the most isolated half of the events (i.e keeping the events which are closest to the isolated signal region), or in the electron sub-channel by using a different single-electron trigger to probe potential trigger biases in the isolation requirements. Variations of the normalisation of the contamination from the top and $W+$jets processes in the multi-jet control region are also considered, that affect the multi-jet templates through the subtraction procedure. In addition, uncertainties affecting only the multi-jet normalisation are estimated. The distribution of the azimuthal separation between the charged lepton and the vectorial sum of the momenta of the selected jets is used in the template fit instead of the m_{T}^{W} distribution. In the electron sub-channel, the $E_{\mathrm{T}}^{\mathrm{miss}} < 30\,\mathrm{GeV}$ region is included, that significantly enhances the multi-jet contribution in the template fit. The respective effects of all these uncertainty sources on the extracted multi-jet normalisation are added in quadrature to yield the multi-jet normalisation uncertainty, separately for the electron and muon sub-channels and for the 2-jet and 3-jet categories. The variations that yield changes to the multi-jet templates are considered as separate shape uncertainties. The effects are taken as uncorrelated between the electron and muon sub-channels, and between the 2-jet and 3-jet categories. A summary of the multi-jet uncertainties is shown in table 2.7.

2.5.4 Signal uncertainties

The uncertainties in the calculations of the VH production cross-sections and of the $H \to b\bar{b}$ branching fraction are those described in section 1.4.1. The NLO EW effects have a sizable impact in the differential p_{T}^{V} distribution, therefore a dedicated shape uncertainty is assigned. The methods used to estimate the impact of scale variations on the acceptance at particle-level in the STXS categories that are described in section 1.4.2 are also applied to the estimation of these scale variations effects on the overall acceptance of the analysis, including the experimental (detector-level) acceptance effect. The Stewart-Tackmann procedure is used to properly estimate this impact in the jet categories. The uncertainties resulting from scale variations in the m_{bb} and p_{T}^{V} distributions are also considered. Small uncertainties in the analysis acceptance and in the shapes of the m_{bb} and p_{T}^{V} distributions also result from variations of the PDFs and of α_S.

Uncertainties due to the parton-shower and underlying-event models are also evaluated by considering the difference between the nominal Powheg+MiNLO+Pythia 8 sample and an alternative sample using instead Herwig 7 as the parton-shower generator. While this difference yielded negligible effects in the particle-level distributions in the STXS categories discussed in section 1.4.2 since their definition depends mostly on the kinematics of the leptonic vector boson decay, it has a significant impact in the analysis acceptance and in the shapes of the m_{bb} and p_{T}^{V} distributions once the analysis selections are taken into account. A summary of the signal systematic uncertainties is displayed in table 2.8.

Table 2.8: Summary of the systematic uncertainties in the signal modelling. An 'S' symbol is used when only a shape uncertainty is assessed and 'PS/UE' indicates parton shower / underlying event. Where the size of an acceptance systematic uncertainty varies between regions, a range is displayed.

Signal	
Cross-section (scale)	0.7% (qq), 27% (gg)
Cross-section (PDF)	1.9% ($qq \to WH$), 1.6% ($qq \to ZH$), 5% (gg)
$H \to b\bar{b}$ branching fraction	1.7%
Acceptance from scale variations	2.5 – 8.8%
Acceptance from PS/UE variations for 2 or more jets	2.9 – 6.2% (depending on lepton channel)
Acceptance from PS/UE variations for 3 jets	1.8 – 11%
Acceptance from PDF+α_{S} variations	0.5 – 1.3%
m_{bb}, p_{T}^{V}, from scale variations	S
m_{bb}, p_{T}^{V}, from PS/UE variations	S
m_{bb}, p_{T}^{V}, from PDF+α_{S} variations	S
p_{T}^{V} from NLO EW correction	S

2.6 Statistical analysis

The statistical analysis of the data selected is based on a likelihood function $\mathcal{L}(\mu,\boldsymbol{\theta})$, constructed as the product of Poisson probability terms over the bins of the input distributions, and built using the HistFactory tool included in RooStats [166, 167]. The likelihood function takes the form:

$$\mathcal{L}(\mu,\boldsymbol{\theta}) = \prod_{i\in\text{bins}} \text{Pois}\left(n_i | \mu s_i(\boldsymbol{\theta}) + b_i(\boldsymbol{\theta})\right) \prod_{\theta\in\boldsymbol{\theta}} \mathcal{C}(\theta). \quad (2.1)$$

In eq. (2.1), μ is the signal strength that multiplies the SM Higgs boson production cross-section times the branching fraction into $b\bar{b}$ and is the parameter of interest to be extracted by maximising the likelihood. The signals and backgrounds yields in each bin of the input distributions are referred to as s_i and b_i, respectively. Both depend on the nuisance parameters (NP), $\boldsymbol{\theta}$, which encode the effects of the systematic uncertainties in the likelihood, and are classified in three main types that differ in their constraint terms $\mathscr{C}$.

As mentioned in section 2.5.2, the normalisations of the largest backgrounds $t\bar{t}$, $Z+$ hf and $W+$ hf can be reliably determined in the fit and are therefore left unconstrained in the likelihood ($\mathscr{C}(\theta) = 1$).

All the other systematic uncertainties discussed in section 2.5 are constrained using Gaussian probability density functions, which in the frequentist language must be thought as auxiliary measurements of the nuisance parameter considered: $\mathscr{C}(\theta) = \mathrm{Gaus}(0|\theta, 1)$. The systematic uncertainty estimates consist in normalisation or shape variations which are assumed to represent the $\pm 1\sigma$ variations under the constraint, and therefore correspond to the parameter values $\theta = \pm 1$. There is some freedom in the interpolation between the nominal and the varied templates for $-1 < \theta < 1$, and in the extrapolation beyond the varied templates for $|\theta| > 1$. The default setting of HistFactory is employed, which uses a linear interpolation for the shape components, and a polynomial interpolation with an exponential extrapolation for the normalisation components. The latter approach has two advantages: it avoids a possible kink (discontinuous derivatives) at $\theta = 0$ which appears with a linear interpolation when the positive and negative uncertainties are different, and which can sometimes cause difficulties in the minimisation by Minuit ; paired with the Gaussian constraint it acts as a log-normal constraint for $|\theta| > 1$, which ensures that the normalisation never becomes negative.

The uncertainties due to the limited number of events in the simulated samples used for the background predictions are also included in the likelihood, using the Barlow-Beeston technique [168] where one multiplicative nuisance parameter is assigned to each bin, with a Poisson constraint term whose parameter is the effective number of events corresponding to the relative statistical uncertainty of the background template in that bin: $\mathscr{C}(\theta) = \mathrm{Pois}(m_i|\theta\tau_i)$. As θ is then a multiplicative factor on b_i chosen to be centered around 1, then $m_i = \tau_i = (b_i/\delta_{bi})^2$, with δ_{bi} being the statistical uncertainty in the background template in the bin i. It must be understood that τ_i is the parameter of the Poisson distribution and therefore a constant, while m_i is the number of effective simulated events, and would fluctuate around $\theta\tau_i$ if we were to generate pseudo-experiments.

The probability that the background-only hypothesis is compatible with the observed data is determined using the q_0 test statistic constructed from the profile-likelihood ratio with the asymptotic approximation [169]:

$$q_0 = -2\log\Lambda_0 = -2\log\frac{\mathscr{L}(0,\hat{\hat{\boldsymbol{\theta}}}_0)}{\mathscr{L}(\hat{\mu},\hat{\boldsymbol{\theta}})}. \tag{2.2}$$

In eq. (2.2), $\hat{\mu}$ and $\hat{\boldsymbol{\theta}}$ are the values of the parameter of interest of the nuisance parameters that unconditionally maximise the likelihood, while $\hat{\hat{\boldsymbol{\theta}}}_0$ represents the values of the nuisance parameters that maximise the likelihood for $\mu = 0$.

2.6.1 Working with complex profile likelihood analyses

The likelihood function used in the $VH(b\bar{b})$ analysis includes about 15 analysis regions, resulting in over 120 bins, that each contain from 10 to 15 templates for the different signal and background contributions. Over 100 sources of experimental and modelling uncertainties are considered, plus one uncertainty due to the statistical uncertainty of the background templates for each bin. The product of these numbers concur to make the likelihood function a complex object, that has to be thoroughly studied and checked for the maximisation procedure to yield meaningful results.

Checks of the likelihood function

Beyond simple checks of the likelihood contents to ensure that all templates and all uncertainties are included as intended, a lot of insight on the likelihood function can be gained by performing simple fits either to the Asimov dataset (as defined in [169]) or to the analysis data and inspecting the post-fit values and uncertainties of the fit parameters. These can indeed point towards pathologies in the likelihood, or towards deficiencies in the background uncertainty model. It is important that these checks are performed prior to the unblinding of the results. This can be achieved either by simply blinding the post-fit value of the signal strength, or by fixing it to 1 (which in the case of an analysis with low signal-to-background ratio does not bias significantly the post-fit values of the nuisance parameters).

A post-fit value of a constrained nuisance parameter significantly different from 0 (usually called a *pull*) indicates that the data is significantly better fitted by a template varied according to the effect of a systematic uncertainty. A post-fit uncertainty < 1 for a nuisance parameter indicates that the data is sufficiently precise to provide a higher constraint on the allowed variation than the one provided by the auxiliary measurement. Nuisance parameters with an estimated uncertainty > 1 (underconstraint) often point to an underlying problem such as incorrect normalisation or non-convergence. They can also indicate cases where the $+1\sigma$ and -1σ variations are on the same side with respect to the nominal template, which should not happen except in very specific circumstances.

The aim of the investigations of the likelihood is to understand, among the significant pulls and constraints of nuisance parameters, which indicate likelihood pathologies or an improper background model, and which are a legitimate, reasonable use of the data, in particular of the control regions, in order to improve upon the estimated background modelling uncertainties. In general, significant pulls or constraints on the nuisance parameters of the experimental systematic uncertainties are not expected, as the analysis is not supposed to measure them with a precision matching that of their dedicated calibration analyses. A frequent cause for unexpected behaviour of these nuisance parameters are pathological uncertainty templates, which are discussed below in section 2.6.1.

Background model nuisance parameters with large pulls or significant post-fit constraints are investigated individually. To help selecting the cases which should be studied in depth, it is useful to introduce the concept of *significance of a pull*. In the following, the example of parameters with a Normal constraint is used for simplicity, but the same concept can be applied to the Poisson constraint of the nuisance parameters on the statistics of the simulated samples. The argument is that a given post-fit value for a nuisance parameter may reflect very different situations. If the post-fit uncertainty on the parameter is very small, it means that the data have sufficient statistical power to measure this nuisance parameter much more precisely than the auxiliary measurement. A large deviation of the post-fit value from 0 can happen in this case without necessarily meaning that the data and the auxiliary measurement are in tension. Conversely, if the post-fit uncertainty is not much smaller than 1 and the post-fit value is large, it means that the data is trying to pull the parameter very far away from 0 without having the power to overcome the Gaussian constraint from the auxiliary measurement. Such a case then indicates possibly a more serious mismodelling of the data by the likelihood model, which needs further attention. This reasoning can be formalized by quantifying the probability of compatibility of the post-fit value of the nuisance parameter with the value of its auxiliary measurement (i.e 0). Under the assumption of Wald's approximation [170] for the profile likelihood over the parameter θ when the corresponding constraint term is removed, i.e that if θ is considered as an unconstrained parameter then the profile likelihood can be approximated by a Gaussian distribution around its best-fit value, then the significance of the compatibility of the post-fit value of the parameter with 0 is:

$$Z_\theta = \frac{\hat{\theta}}{\sqrt{1-\sigma_\theta^2}}, \tag{2.3}$$

where σ_θ is the post-fit uncertainty on $\hat{\theta}$. The demonstration of this result is given in appendix A.1. The usefulness of using this quantity when assessing the validity of the likelihood function is to raise the attention on nuisance parameters whose pull is not large enough to pass the subjective threshold one uses to trigger deeper investigations, compared to other parameters more pulled but also more constrained. The values of Z_θ should in any case be taken *cum grano salis*, as they become sensitive to the limited numerical precision on $\hat{\theta}$ and σ_θ when $\sigma_\theta \sim 1$ which can yield spurious large significances.

The validity of the significant pulls and constraints of the nuisance parameters related to background modelling can be assessed by combining several tools:

Comparisons of analyses. The fit results of the main multivariate analysis can be compared to that of the validation diboson analysis, and to that of the cross-check dijet-mass analysis, that both differ in the choice of the fitted distributions, and (in the case of the dijet-mass analysis) by slightly different analysis selections. A post-fit nuisance parameter value consistent between the three cases is more likely to originate from a real feature in the data that is picked up in the minimization. As an example, the floated normalizations of the $t\bar{t}$ and $V+$jets backgrounds are very similar in the three cases. Similarly, fits to single lepton channels are compared together and with the combined fit.

Comparisons of likelihood configurations. The assumptions on the correlation (or absence of correlation) of background uncertainties over parts of the analysis phase space are among the most important hypotheses that are built in the likelihood function. While they are based on physics judgement on a case-by-case basis, as discussed in section 2.5.2, they can be checked to some extent by comparing the nominal fit results with specific fits where the nuisance parameter under investigation is uncorrelated in all analysis regions. Tensions in the pulls in different regions may indicate that the assumption on the correlation of the nuisance parameter is incorrect, or that some other effect is not properly covered in the background model and may call for additional uncertainties.

Post-fit distributions. Post-fit plots of distributions different from the fitted ones can be made by propagating the post-fit values of the nuisance parameters. This is especially useful for m_{bb} and p_{T}^V distributions, as a good post-fit agreement with the data helps to gain confidence in the pulls of the related m_{bb} and p_{T}^V shape uncertainties.

The use of the methods described above does not lead to clear-cut answers in all cases, in particular as post-fit correlations appear between all nuisance parameters. Furthermore the absence of any pull or constraint is not a proof that the chosen set of uncertainties for the background model provides adequate coverage of the true uncertainty. The combination of all checks described is nonetheless very effective to gain confidence in the appropriateness of the background model.

Smoothing of systematic uncertainties

In the absence of a way to provide uncertainty on the uncertainties[2], an assumption built in the likelihood function is that the templates provided for the systematic uncertainties represent the true $\pm 1\sigma$ variations of the uncertainty. However, the estimation of some of the uncertainties relies on different simulated events being selected in the systematic template than in the nominal template. There is therefore a statistical uncertainty in the varied template which can result in incorrect fit results, in particular spurious over- or underconstraints of the nuisance parameter, for instance through bins where the $+1\sigma$ and -1σ variations are on the same side with respect to the nominal template. Several techniques are used to obtain smooth systematic templates (with respect to the nominal one) in the different cases.

Shape uncertainties of the signal and background models. As discussed in section 2.5, the shape uncertainties in the m_{bb} and p_{T}^{V} distributions of the signal and of several background processes are obtained by comparing the distributions from different generators, or from different configurations of a generator. In most of the cases, different simulated events are then present in the nominal template and in the variation. The ratio between the varied template and the nominal one is fitted by a simple polynomial or exponential function. For a given event in the nominal template (and therefore given values of m_{bb} and p_{T}^{V}), the value of the fitted function is then used as an event weight to yield the varied template. This procedure gives by construction a smooth variation for the systematic uncertainty in all distributions.

Energy scale and energy resolution systematic uncertainties. These uncertainties are evaluated by applying the analysis selections to the simulated events after shifting or smearing the energy of the reconstructed objects. The difference between the nominal and the varied cases comes from events migrating in or out of the acceptance, and from events migrating between analysis bins. The ratios of the varied templates to the nominal template have complex statistical uncertainties, because of the partial overlap of events between them. The strategy to obtain smooth ratios is to rebin them until the variation is statistically significant in each bin. Because of the complex statistical correlations of the events, a mathematically correct evaluation of statistically significant variations can only be achieved through techniques such as bootstrapping [172, 173], which are impractical to use due to the very large number of templates to smooth. Heuristic algorithms are employed instead to rebin the ratios with an accuracy deemed good enough to retain the correct shape effects while smoothing the statistical fluctuations. A study of such algorithms was conducted as part of the analysis of the Run-1 data [51], where their performance was evaluated on an ensemble of low statistics toy datasets sampled from a high statistics sample of simulated $t\bar{t}$ events. The selected algorithm merges bins in a ratio between a varied and a nominal template based on the constraints that the statistical uncertainty in each bin (evaluated on the nominal template) should be less than 5%, and that the shape of the ratio remain physical: monotonous for a BDT_{VH} or BDT_{VZ} discriminant, and with at most one local extremum for a dijet mass. It runs iteratively from the initial ratio, and removes local extrema one at a time until the monotonicity criteria is met, chosing the one that preserves the most shape similarity with the initial ratio, as evaluated by a simple χ^2 test. The relevance of this algorithm in the analysis of the Run-2 data was checked by comparing the varied templates before and after this smoothing procedure is applied.

---

[2] ↑Although a model introducing parameters to account for the uncertainty in the systematic errors has been developed [171], its general application to the cases discussed below would be far from practical.

Pruning of systematic uncertainties

The large number of uncertainty components included in the likelihood function resulting from the multiplication of the number of signal and background templates by the number of analysis regions and by the number of uncertainty sources, results in long likelihood maximisation times. This can be detrimental for the quality of the analysis as it slows down the process of likelihood checks described above. A pruning procedure is therefore employed to remove uncertainty components (region by region and template by template) that have a negligible impact on the final results. A normalisation (shape) uncertainty is dropped if the associated template variation is below 0.5% (below 0.5% in all bins). Looser pruning criteria are applied to small backgrounds (less than 1% of the total background), where the impact of the template variation is compared to the signal template in signal regions, and to the total background in control regions. Finally, for systematic uncertainties where opposite-sign variations are expected, the shape uncertainties are dropped when the up- and down-varied shapes are more similar to each other than to the nominal template (as quantified by a χ^2). This procedure allows to reduce the computation time significantly, and its validity is checked by comparing the fit results before and after its use.

2.6.2 Multivariate analysis

Following the analysis selections discussed in section 2.3.2, the likelihood function contains eight signal regions, and 6 control regions. The signal regions are the 2- and 3-jet categories in the high-p_{T}^{V} region in the three channels, and the medium-p_{T}^{V} region in the 2-lepton channel. The BDT$_{VH}$ distribution is fitted in these regions. The control regions are the two $W+$hf CR in the 1-lepton channel, in which the yields are used in the fit, and the four $e\mu$ regions in the 2-lepton channel, where the m_{bb} distributions are used, except for the 2-jet category of the high-p_{T}^{V} region, where the event yield is used because of the relatively low statistics. Figure 2.6 shows a representation of the fit setup, with the categorisation of the regions and the distributions used in the fit.

While simple 50 GeV-wide bins are used in the m_{bb} distributions of the $e\mu$ regions, the binning employed in the BDT$_{VH}$ distributions is the result of an optimization. Since the numerical values of the output of the BDTs trained using TMVA do not have any specific meaning, the distribution can be freely remapped. Several rebinning algorithms were studied in the context of the analysis of the Run-1 data [51] and are discussed in details in the thesis of Daniel Büscher [174]. Their triple goal is to keep a sufficiently fine binning in the high signal-to-background ratio region to maximise the signal sensitivity, albeit not too fine in order to avoid any bias (similar to an overtraining effect); in the low sensitivity part of the distribution, coarser bins are sufficient, as the goal is to keep just enough information to improve the background separation and possibly constrain some background modelling nuisance parameters. Starting from a finely binned BDT$_{VH}$ output, the algorithm chosen for the analysis of the Run-2 data uses the following quantity:

$$Z(k,l) = \frac{z_s}{S}\sum_{i=k}^{l} s_i + \frac{z_b}{B}\sum_{i=k}^{l} b_i, \tag{2.4}$$

where n_i and b_i are the signal and background yields in the bin i, S and B the total signal and background yields, and z_s and z_b two parameters. The algorithm runs iteratively. Starting with $k = l =$ last bin, k is decreased until $Z(k,l) \geq 1$. The bins between k and l are then merged into a single one, l is set to $k-1$, and the procedure is repeated. After application of the algorithm, the high-sensitivity bins (for which b_i is small) contain a fraction of about $1/z_s$ of the total signal each, while the low sensitivity bins contain a fraction of about $1/z_b$ of the total background each. The

Table 2.9: Factors applied to the nominal normalisations of the $t\bar{t}$, $W+\text{hf}$ and $Z+\text{hf}$ backgrounds, as obtained from the global likelihood fit to the 13 TeV data for the nominal multivariate analysis, used to extract the Higgs boson signal. The errors represent the combined statistical and systematic uncertainties.

Process	Normalisation factor
$t\bar{t}$ 0- and 1-lepton	0.98 ± 0.08
$t\bar{t}$ 2-lepton 2-jet	1.06 ± 0.09
$t\bar{t}$ 2-lepton 3-jet	0.95 ± 0.06
$W+\text{hf}$ 2-jet	1.19 ± 0.12
$W+\text{hf}$ 3-jet	1.05 ± 0.12
$Z+\text{hf}$ 2-jet	1.37 ± 0.11
$Z+\text{hf}$ 3-jet	1.09 ± 0.09

values $z_s = 10$ and $z_b = 5$ are found to be a good compromise for the analysis sensitivity, resulting in output distributions with 15 bins.

The post-fit normalisation factors of the unconstrained backgrounds in the global likelihood fit are shown in table 2.9. They are all close to 1, except for the normalisations of the $V+\text{hf}$ backgrounds in the 2-jet regions, which are all found to be significantly larger than 1. This feature is present in the three lepton channels.

The effects of systematics uncertainties on the measurement of the signal strength are quantified using complementary methods. Figure 2.7 presents the impact of individual nuisance parameters: for each parameter θ it is evaluated as the change in the fitted signal strength when profiling the likelihood at the values corresponding to the parameter' $+1\sigma$ and -1σ post-fit values. In practice it means evaluating $\hat{\hat{\mu}}_\theta - \hat{\mu}$ when solving $-2\log\mathscr{L}(\hat{\hat{\mu}}_\theta, \theta, \hat{\hat{\boldsymbol{\theta}}}_\theta) = -2\log\mathscr{L}(\hat{\mu}, \hat{\theta}, \hat{\boldsymbol{\theta}}) + 1$. The systematic uncertainties listed in fig. 2.7 are ranked in decreasing order of their impact on the signal strength, so that only 15 most significant ones are shown. The post-fit values of these parameters and their fitted uncertainties are also shown. Background modelling uncertainties have the largest impact on the signal strength, in particular those related to the m_{bb} and p_{T}^{V} shapes of all backgrounds. Signal modelling uncertainties are also important. Among the experimental uncertainties, the ones related to b-tagging are the most significant. The constraints observed on the nuisance parameters controlling the $t\bar{t}$ m_{bb} shapes are explained by the large data sample and high purity in the 1-lepton 3-jet region (for the 0+1-lepton parameter) and in the $e\mu$ control regions (for the 2-lepton parameter). The signifiant pull and constraint on the $Z+\text{hf}$ m_{bb} shape parameter is coming from both the 0- and 2-lepton channels, and corrects a mismodelling observed in the sidebands of the m_{bb} distribution. The events in those sidebands end up in bins in the low sensitivity part of the BDT_{VH} distributions, therefore the information on this mismodelling is preserved in the multivariate analysis.

An alternative method is used to evaluate the combined impact of groups of nuisance parameters. As all parameters are correlated by the fit, there is no single unambiguous definition for such a combined impact, and various procedures will account for the correlations in different ways and lead to different results. In the $VH(b\bar{b})$ analysis, the impact of a category of systematic uncertainties is defined as the difference in quadrature between the uncertainty in μ when all nuisance parameters are fitted, and when the parameters in the category are fixed to their best-fit values. The total statistical uncertainty is defined as the uncertainty in μ when all the nuisance parameters are fixed to their best-fit values. The total systematic uncertainty is then defined as the difference in quadrature between the total uncertainty in μ and the total statistical uncertainty. The results of this evaluation are shown in table 2.10 and confirm the conclusions drawn from fig. 2.7: the systematic uncertainties

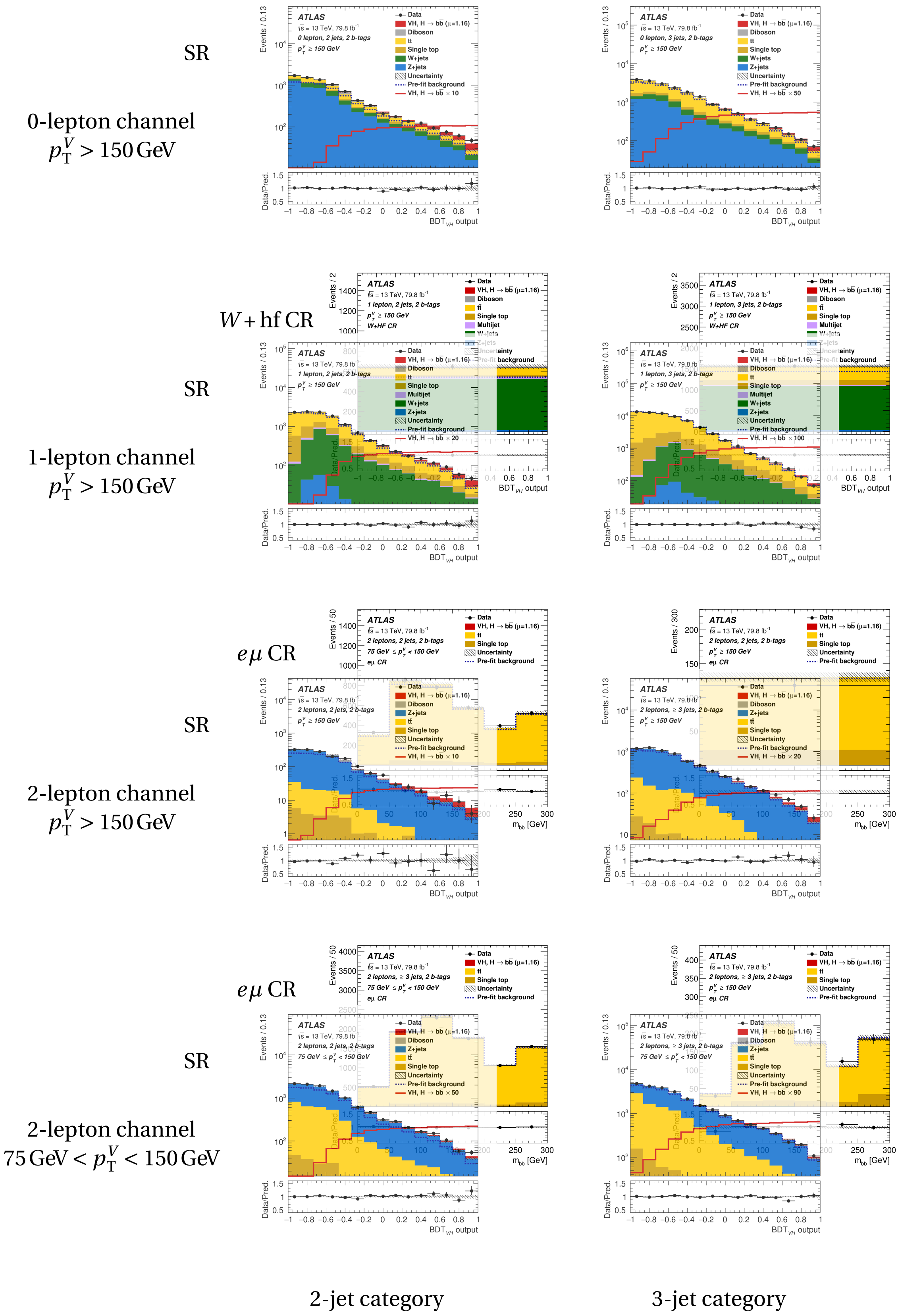

Figure 2.6: Representation of the setup of the global likelihood fit of the multivariate analysis, with signal and control regions included, and fitted distributions.

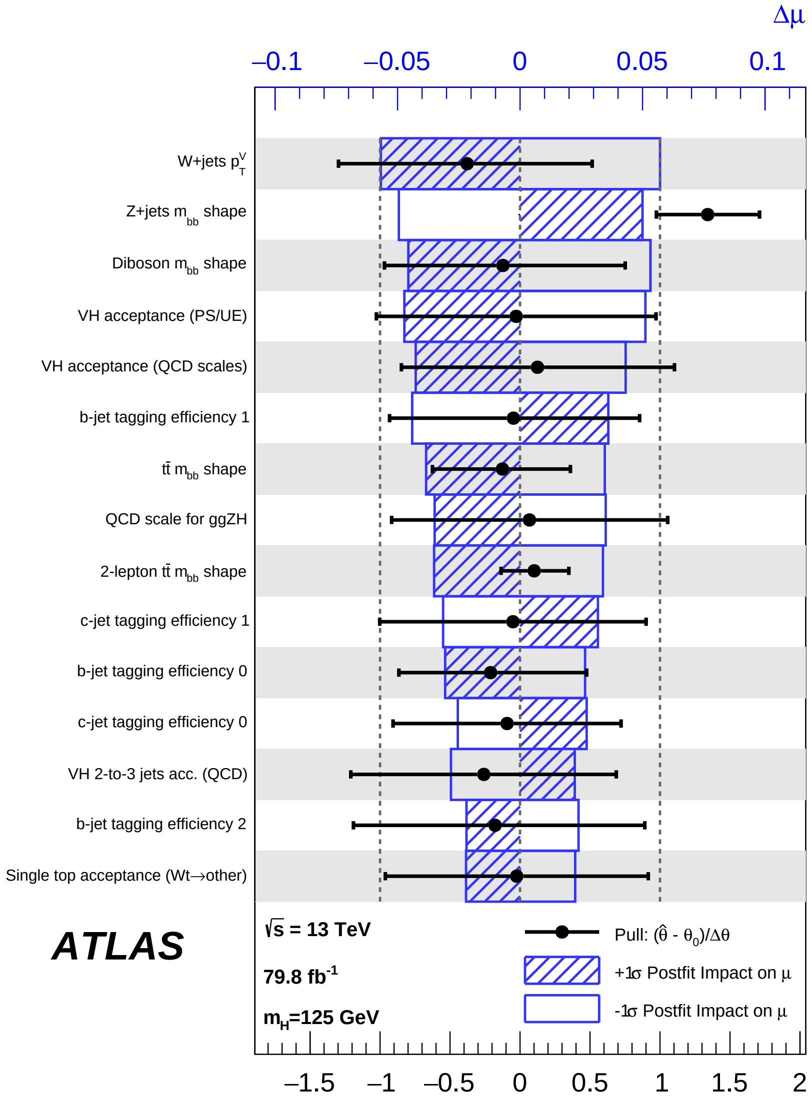

Figure 2.7: Impact of systematic uncertainties for the fitted Higgs boson signal strength μ for the nominal MVA analysis applied to the 13 TeV data. The systematic uncertainties are listed in decreasing order of their impact on μ. The hatched and open boxes correspond to the upwards and downwards variations, respectively. The filled circles, referring to the bottom x-axis, show the deviations of the fitted nuisance parameters $\hat{\theta}$ from their nominal values θ_0, expressed in terms of standard deviations with respect to their nominal uncertainties $\Delta\theta$. The associated error bars show the fitted uncertainties of the nuisance parameters, relative to their nominal uncertainties. As the b-tagging uncertainties are decomposed into uncorrelated components, the labels 0 and 1 refer to the leading and second-leading components.

Table 2.10: Breakdown of the contributions to the uncertainty in μ. The sum in quadrature of the systematic uncertainties attached to the categories differs from the total systematic uncertainty due to correlations.

Source of uncertainty		σ_μ
Total		0.259
Statistical		0.161
Systematic		0.203
Experimental uncertainties		
Jets		0.035
$E_{\mathrm{T}}^{\mathrm{miss}}$		0.014
Leptons		0.009
b-tagging	b-jets	0.061
	c-jets	0.042
	light-flavour jets	0.009
	extrapolation	0.008
Pile-up		0.007
Luminosity		0.023
Theoretical and modelling uncertainties		
Signal		0.094
Floating normalisations		0.035
$Z+$jets		0.055
$W+$jets		0.060
$t\bar{t}$		0.050
Single top quark		0.028
Diboson		0.054
Multi-jet		0.005
MC statistical		0.070

in the modelling of the signal and of the backgrounds have the largest impact in the measurement of the signal strength, followed by the b-tagging uncertainty of both b- and c-jets. In addition, it shows that the uncertainty due to the limited size of the simulated samples plays a significant role as well. Because of the correlations between the parameters induced by the fit the total systematic uncertainty is different from the sum in quadrature of the uncertainties from the breakdown in categories. This procedure to estimate a combined impact has the undesirable property of yielding very asymmetric results for the uncertainties in the modelling of the signal, therefore symmetrized results are presented in table 2.10. A proof of this effect is given in appendix A.2, along with a discussion on the comparison between the two methods used to quantify the impact of nuisance parameters.

2.6.3 Dijet-mass analysis

As explained in section 2.3.5, the dijet-mass analysis has a finer categorisation of the signal regions, with an additional split at $p_{\mathrm{T}}^{V} = 200\,\mathrm{GeV}$, while the $W+\mathrm{hf}$ control regions are merged into the corresponding 1-lepton signal regions. This results in 14 signal regions and 4 control regions in which the m_{bb} distributions are input to the fit, with the exception of the two $e\mu$ control regions in the 2-jet category, where the event yield is used.

2.6.4 Diboson analysis

The diboson analysis aims at validating the model embedded in the likelihood function by measuring the signal strength of the WZ and ZZ processes instead of that of VH. Therefore the main difference with the main analysis is the use of the BDT_{VZ} distributions in the signal regions instead of the BDT_{VH} ones as inputs to the likelihood function. Because of the smaller samples of simulated diboson events compared to the Higgs boson samples, the binning of the BDT_{VZ} distributions cannot be as fine as that of the BDT_{VH} distributions. Adequate parameters for the binning algorithm are found to be $z_s = 5$ and $z_b = 5$. The parameter of interest μ_{VZ} is the signal strength of the combined WZ and ZZ processes. The small contribution from WW production is treated as a background and constrained within its uncertainty. The overall normalisation uncertainties in the WZ and ZZ processes are removed, while all the other systematic uncertainties are kept identical to those in the main analysis. The SM Higgs boson processes are included as backgrounds with an additional uncertainty in the cross-section of 50%, which conservatively comprises the previous measurement and its uncertainty [53]. The BDTs provide sufficient separation between the VZ and the VH processes that the VH normalisation has a negligible impact on the diboson signal strength measurement.

2.7 Results

2.7.1 Distributions and yields

The BDT_{VH} output distributions in the signal regions are shown in fig. 2.8 for the 0- and 1-lepton channels, and in fig. 2.9 for the 2-lepton channel. The yields and the m_{bb} distributions in the $W+\mathrm{hf}$ and $e\mu$ control regions are presented in appendix as fig. B.2. The post-fit distributions are obtained by normalising the signal and backgrounds and setting the nuisance parameters to the result of the maximum likelihood fit. The post-fit yields of the signal and backgrounds are shown in table 2.11 and table B.1 (in appendix) for the signal and control regions, respectively.

An excellent agreement is achieved between the post-fit predictions and the data in all BDT_{VH} distributions and in the control regions. This agreement extends to all distributions of the kinematic variables that are used as inputs to the BDTs. Figure 2.10 shows m_{bb} and p_{T}^{V} distributions as examples, while further cases are presented in appendix as fig. B.1.

A graphical summary of the sensitivity of the analysis is shown in fig. 2.11, where the bins of BDT_{VH} distributions in all regions are combined into bins of $\log(S/B)$, S and B being the fitted signal and background yields in each analysis bin, respectively. This figure provides some insights of the origin of the sensitivity of the analysis: even without accounting for the systematic uncertainties, it shows that the majority of the sensitivity is in the analysis bins with relatively good S/B (over 0.1) despite the lower statistics available.

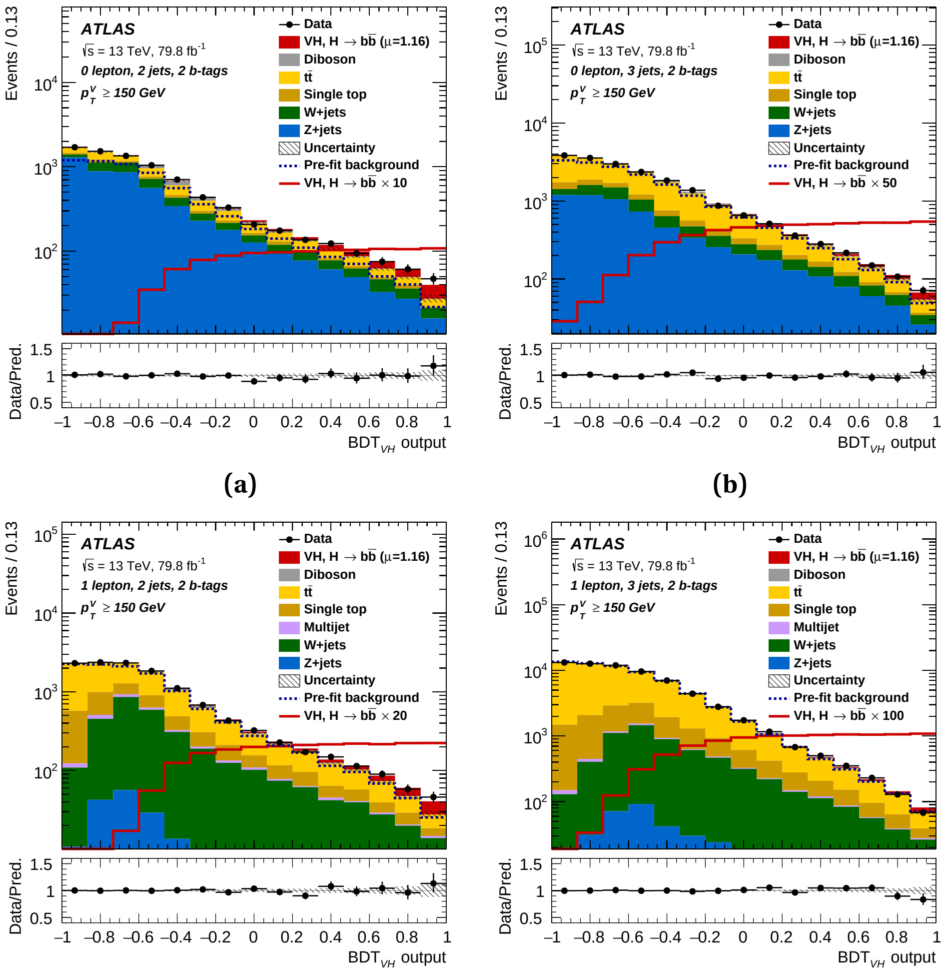

(a) **(b)**

(c) **(d)**

Figure 2.8: The BDT$_{VH}$ output post-fit distributions in the 0-lepton (top) and 1-lepton (bottom) channels for 2-b-tag events, in the 2-jet (left) and 3-jet (right) categories. The background contributions after the global likelihood fit are shown as filled histograms. The Higgs boson signal (m_H = 125 GeV) is shown as a filled histogram on top of the fitted backgrounds normalised to the signal yield extracted from data (μ = 1.16), and unstacked as an unfilled histogram, scaled by the factor indicated in the legend. The dashed histogram shows the total pre-fit background. The size of the combined statistical and systematic uncertainty for the sum of the fitted signal and background is indicated by the hatched band. The ratio of the data to the sum of the fitted signal (μ = 1.16) and background is shown in the lower panel. The BDT$_{VH}$ output distributions are shown with the binning used in the global likelihood fit.

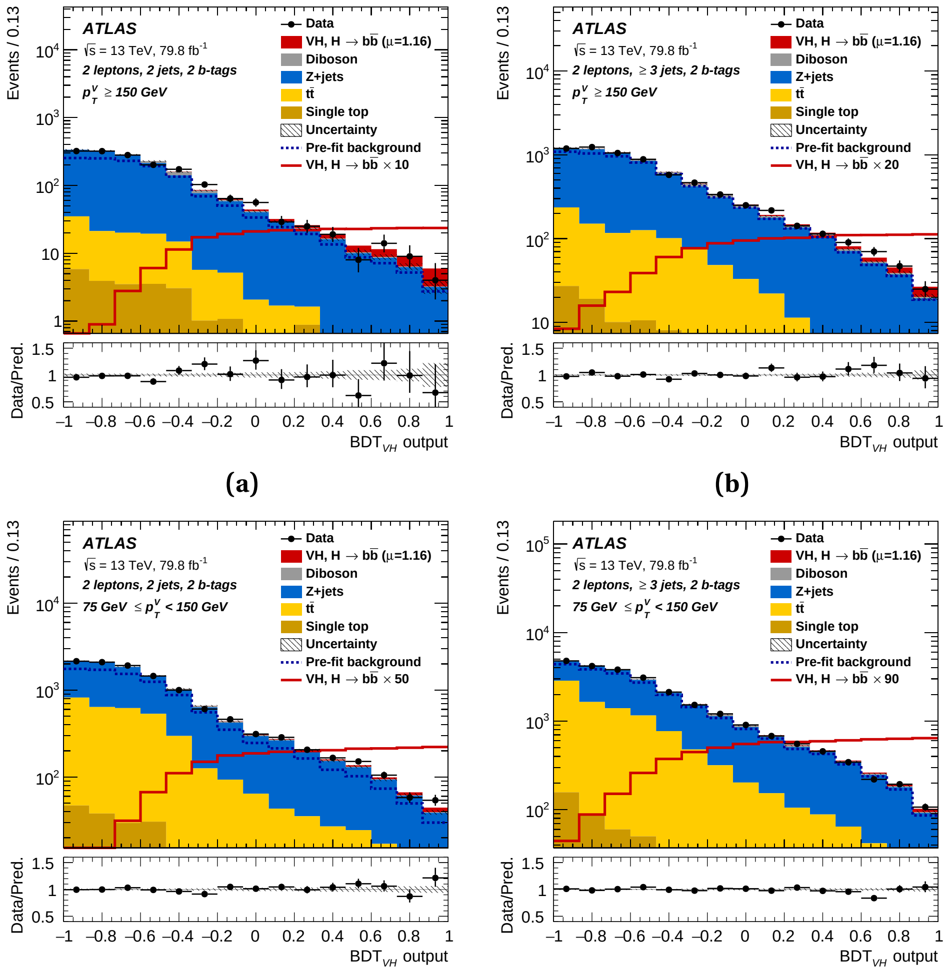

(a) (b)

(c) (d)

Figure 2.9: The BDT$_{VH}$ output post-fit distributions in the 2-lepton channel, in the high-p_{T}^{V} (top) and medium-p_{T}^{V} (bottom) regions, in the 2-jet (left) and ≥3-jet (right) categories. The background contributions after the global likelihood fit are shown as filled histograms. The Higgs boson signal (m_H = 125 GeV) is shown as a filled histogram on top of the fitted backgrounds normalised to the signal yield extracted from data (μ = 1.16), and unstacked as an unfilled histogram, scaled by the factor indicated in the legend. The dashed histogram shows the total pre-fit background. The size of the combined statistical and systematic uncertainty for the sum of the fitted signal and background is indicated by the hatched band. The ratio of the data to the sum of the fitted signal (μ = 1.16) and background is shown in the lower panel. The BDT$_{VH}$ output distributions are shown with the binning used in the global likelihood fit.

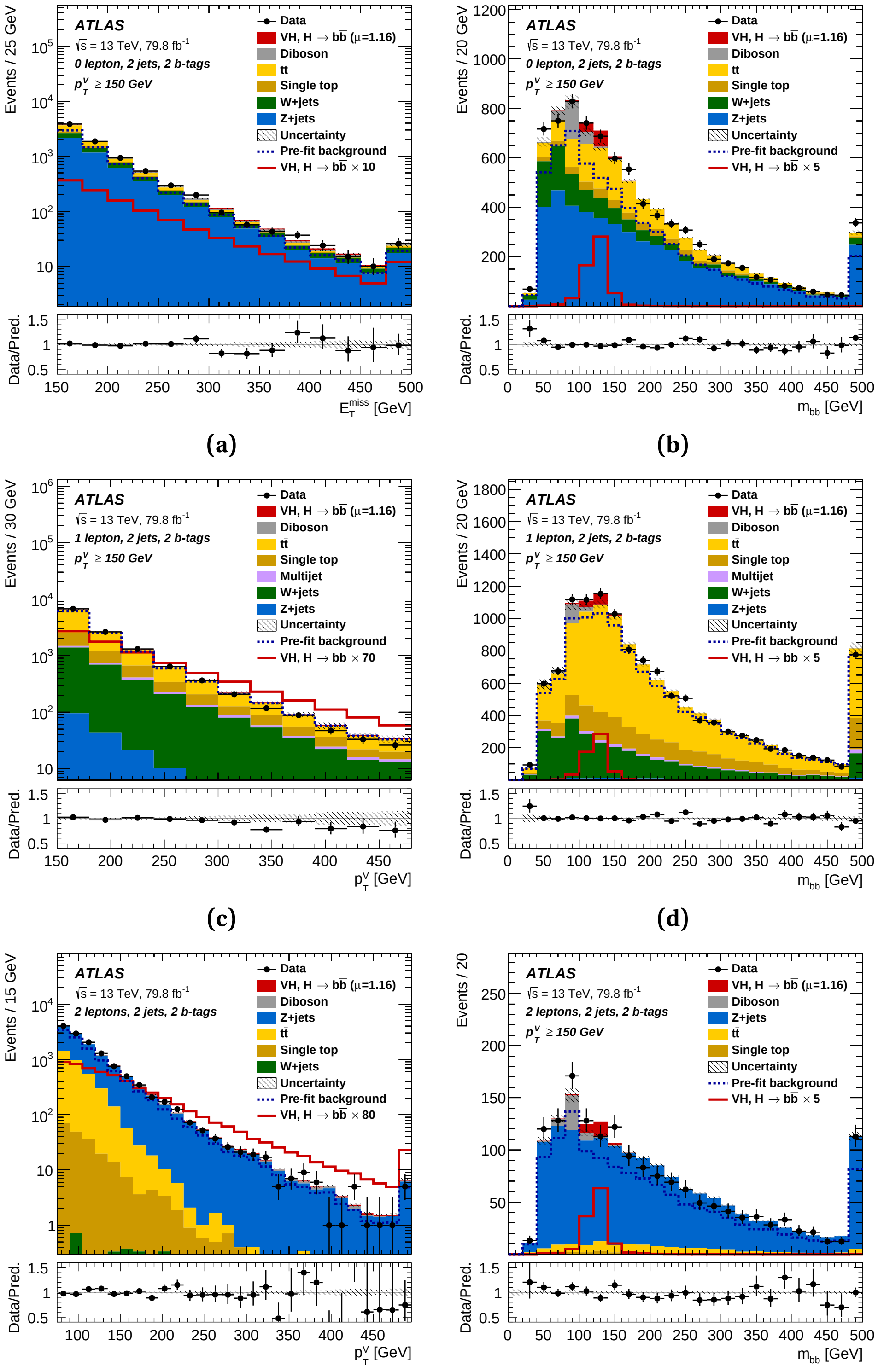

(a) **(b)**

(c) **(d)**

(e) **(f)**

Figure 2.10: The post-fit distributions for p_{T}^{V} (left) and m_{bb} (right) in the 0-lepton (top), 1-lepton (middle) and 2-lepton (bottom) channels for 2-jet, 2-b-tag events in the high p_{T}^{V} region (except for the p_{T}^{V} distribution in the 2-lepton channel that spans both the medium-p_{T}^{V} and the high-p_{T}^{V} regions). The background contributions after the global likelihood fit are shown as filled histograms. The Higgs boson signal ($m_H = 125$ GeV) is shown as a filled histogram on top of the fitted backgrounds normalised to the signal yield extracted from data ($\mu = 1.16$), and unstacked as an unfilled histogram, scaled by the factor indicated in the legend. The entries in overflow are included in the last bin. The dashed histogram shows the total pre-fit background. The size of the combined statistical and systematic uncertainty for the sum of the fitted signal and background is indicated by the hatched band. The ratio of the data to the sum of the fitted signal and background is shown in the lower panel.

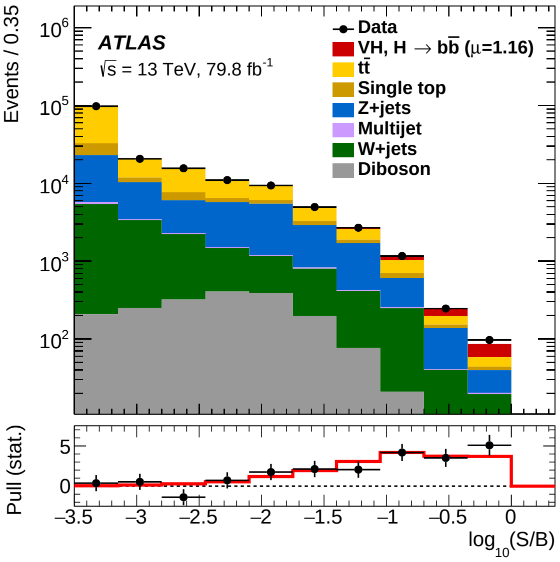

Figure 2.11: Event yields as a function of $\log_{10}(S/B)$ for data, background and a Higgs boson signal with $m_H = 125$ GeV. Final-discriminant bins in all regions are combined into bins of $\log_{10}(S/B)$, with S being the fitted signal and B the fitted background yields. The Higgs boson signal contribution is shown after rescaling the SM cross-section according to the value of the signal strength extracted from data ($\mu = 1.16$). In the lower panel, the pull of the data relative to the background (the statistical significance of the difference between data and fitted background) is shown with statistical uncertainties only. The full line indicates the pull expected from the sum of fitted signal and background relative to the fitted background.

Table 2.11: The Higgs boson signal, background and data yields for each signal region category in each channel after the full selection of the multivariate analysis. The signal and background yields are normalised to the results of the global likelihood fit. All systematic uncertainties are included in the indicated uncertainties. An entry of "–" indicates that a specific background component is negligible in a certain region, or that no simulated events are left after the analysis selection.

	0-lepton		1-lepton		2-lepton			
	$p_T^V > 150$ GeV, 2-b-tag		$p_T^V > 150$ GeV, 2-b-tag		75 GeV $< p_T^V <$ 150 GeV, 2-b-tag		$p_T^V > 150$ GeV, 2-b-tag	
Process	2-jet	3-jet	2-jet	3-jet	2-jet	≥3-jet	2-jet	≥3-jet
$Z+ll$	17 ± 11	27 ± 18	2 ± 1	3 ± 2	14 ± 9	49 ± 32	4 ± 3	30 ± 19
$Z+cl$	45 ± 18	76 ± 30	3 ± 1	7 ± 3	43 ± 17	170 ± 67	12 ± 5	88 ± 35
$Z+$hf	4770 ± 140	5940 ± 300	180 ± 9	348 ± 21	7400 ± 120	14160 ± 220	1421 ± 34	5370 ± 100
$W+ll$	20 ± 13	32 ± 22	31 ± 23	65 ± 48	< 1	< 1	< 1	< 1
$W+cl$	43 ± 20	83 ± 38	139 ± 67	250 ± 120	< 1	< 1	< 1	< 1
$W+$hf	1000 ± 87	1990 ± 200	2660 ± 270	5400 ± 670	2 ± 0	13 ± 2	1 ± 0	4 ± 1
Single top quark	368 ± 53	1410 ± 210	2080 ± 290	9400 ± 1400	188 ± 89	440 ± 200	23 ± 7	93 ± 26
$t\bar{t}$	1333 ± 82	9150 ± 400	6600 ± 320	50200 ± 1400	3170 ± 100	8880 ± 220	104 ± 6	839 ± 40
Diboson	254 ± 49	318 ± 90	178 ± 47	330 ± 110	152 ± 32	355 ± 68	52 ± 11	196 ± 35
Multi-jet e sub-ch.	–	–	100 ± 100	41 ± 35	–	–	–	–
Multi-jet μ sub-ch.	–	–	138 ± 92	260 ± 270	–	–	–	–
Total bkg.	7850 ± 90	19020 ± 140	12110 ± 120	66230 ± 270	10960 ± 100	24070 ± 150	1620 ± 30	6620 ± 80
Signal (post-fit)	128 ± 28	128 ± 29	131 ± 30	125 ± 30	51 ± 11	86 ± 22	28 ± 6	67 ± 17
Data	8003	19143	12242	66348	11014	24197	1626	6686

2.7.2 Signal strengths and significances

The combined analysis of the three lepton channels leads, for a Higgs boson mass of 125 GeV, to a probability p_0 of obtaining a signal at least as strong as the one observed in data from background alone of $5.3 \cdot 10^{-7}$, for an expected value of $7.3 \cdot 10^{-6}$. The observed probability corresponds to an excess with a significance of 4.9 standard deviations (s.d.), to be compared with an expectation of 4.3 standard deviations. The measured value of the signal strength is:

$$\mu_{VH}^{bb} = 1.16^{+0.27}_{-0.25} = 1.16 \pm 0.16(\text{stat.})^{+0.21}_{-0.19}(\text{syst.}).$$

The results from the combined fit are compared to those of a fit where the lepton channels have each their own signal strength. The signal strengths, p_0-values and significances of the two fits are shown in table 2.12. The highest expected sensitivity comes from the 0-lepton channel (3.1 s.d.) , followed by the 2-lepton channel (2.6 s.d.) and the 1-lepton channel (2.4 s.d.). The signal strengths measured in the three channels are found compatible with each other, with a slightly larger value measured in the 2-lepton channel. This compatibility can be evaluated quantitatively: in the asymptotic regime, a result from Wilks [175] implies that the difference between the minima of the negative log-likelihoods of two fits differing only in their number of parameters of interest follows a χ^2 distribution with a number of degrees of freedom equal to the difference between the numbers of parameters of interest. The probability of compatibility of the signal strengths measured in the three lepton channels is then found to be 80%.

Table 2.12: Measured signal strengths with their combined statistical and systematic uncertainties, expected and observed p_0 and significance values (in standard deviations) from the combined fit with a single signal strength, and from a combined fit where each of the lepton channels has its own signal strength, using 13 TeV data.

Signal strength	Signal strength	p_0		Significance	
		Exp.	Obs.	Exp.	Obs.
0-lepton	$1.04^{+0.34}_{-0.32}$	$9.5 \cdot 10^{-4}$	$5.1 \cdot 10^{-4}$	3.1	3.3
1-lepton	$1.09^{+0.46}_{-0.42}$	$8.7 \cdot 10^{-3}$	$4.9 \cdot 10^{-3}$	2.4	2.6
2-lepton	$1.38^{+0.46}_{-0.42}$	$4.0 \cdot 10^{-3}$	$3.3 \cdot 10^{-4}$	2.6	3.4
$VH, H \to b\bar{b}$ combination	$1.16^{+0.27}_{-0.25}$	$7.3 \cdot 10^{-6}$	$5.3 \cdot 10^{-7}$	4.3	4.9

Another combined fit is performed, where separate signal strengths are attached to the WH and ZH production processes. The measured signal strengths are shown in fig. 2.12. The probability of their compatibility is found to be 84%. The observed (expected) significances of the WH and ZH production modes are 2.5 (2.3) and 4.0 (3.5) standard deviations, respectively. The linear correlation between the two signal strengths is very small, -1%.

2.7.3 Results of the dijet-mass analysis

The post-fit m_{bb} distributions in the signal regions of the dijet-mass analysis (displayed in appendix B.2) show a good agreement of the post-fit predictions with the data in all regions. The

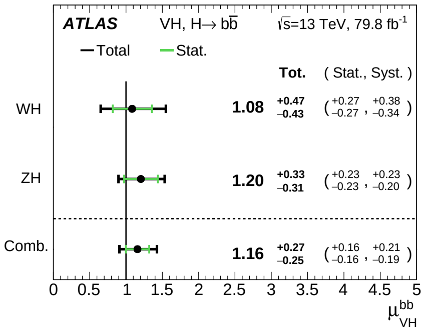

Figure 2.12: The fitted values of the Higgs boson signal strength μ_{VH}^{bb} for $m_H = 125$ GeV for the WH and ZH processes and their combination.

measured value of the signal strength is:

$$\mu_{VH}^{bb} = 1.06^{+0.36}_{-0.33} = 1.06 \pm 0.20(\text{stat.})^{+0.30}_{-0.26}(\text{syst.}).$$

The measurement is in good agreement with that of the multivariate analysis, with an uncertainty larger by about 35%. Consequently, the observed excess has a lower significance of 3.6 s.d., compared to an expectation of 3.5 s.d. The values of the signal strengths in the individual channels are also in good agreement with those from the multivariate analysis, as shown in fig. B.6 (in appendix).

The sensitivity of the dijet-mass analysis is represented in fig. 2.13 in the form of an m_{bb} distribution summed over all channels and regions, weighted by their respective values of the ratio of fitted Higgs signal and background yields and after subtraction of all backgrounds except for the VZ diboson processes. The result is a clear $Z \to b\bar{b}$ peak with a significant shoulder around $m_{bb} = 125$ GeV that matches well the Higgs boson prediction scaled by $\mu_{VH}^{bb} = 1.06$.

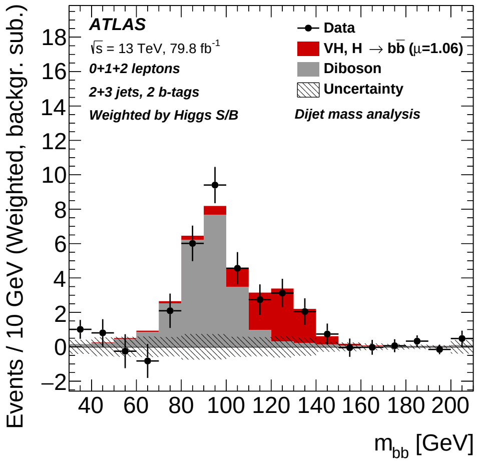

Figure 2.13: The distribution of m_{bb} in data after subtraction of all backgrounds except for the WZ and ZZ diboson processes, as obtained with the dijet-mass analysis. The contributions from all lepton channels, p_{T}^{V} regions and number-of-jets categories are summed and weighted by their respective S/B, with S being the total fitted signal and B the total fitted background in each region. The expected contribution of the associated WH and ZH production of a SM Higgs boson with $m_H = 125$ GeV is shown scaled by the measured signal strength ($\mu = 1.06$). The size of the combined statistical and systematic uncertainty for the fitted background is indicated by the hatched band.

2.7.4 Results of the diboson analysis

The post-fit m_{bb} distributions in the signal regions of the diboson analysis (displayed in appendix B.3) show equally a good agreement of the post-fit predictions with the data in all regions. The measured value of the VZ signal strength is:

$$\mu_{VZ}^{bb} = 1.20^{+0.20}_{-0.18} = 1.20 \pm 0.08(\text{stat.})^{+0.19}_{-0.16}(\text{syst.}).$$

This result, used as a validation of the analysis and therefore obtained before the unblinding of the Higgs boson results, is in good agreement with the Standard Model prediction. This good agreement is still observed when fitting separate signal strengths for the WZ and ZZ production modes (with a probability of compatibility with the combined signal strength of 47%), or for the three lepton channels (with a probability of compatibility of 64%), as shown in fig. 2.14. A limit to the usefulness of this validation analysis is the low sensitivity achieved in the 1-lepton channel, which comes from an accumulation of factors. First, despite a much larger inclusive production cross-section (by over an order of magnitude) for the WZ and ZZ processes compared to the WH and ZH processes, the lower branching fraction for $Z \to b\bar{b}$ compared to $H \to b\bar{b}$ and the softer p_{T}^{V} spectrum for the diboson processes result in yields of events selected in the high-p_{T}^{V} signal regions (as shown in table 2.11) not much larger for the diboson processes than for the Higgs boson signal. The yields of ZZ events are increased relatively to the WZ yields because of the symmetry in the final state. Finally, there is a much larger $W+$hf background under the WZ process than under the WH process in the 1-lepton channel. Because of the large systematic uncertainties in the $W+$hf background, its contribution to the total systematic uncertainty is much larger in the measurement of the WZ signal strength than in that of the WH signal strength.

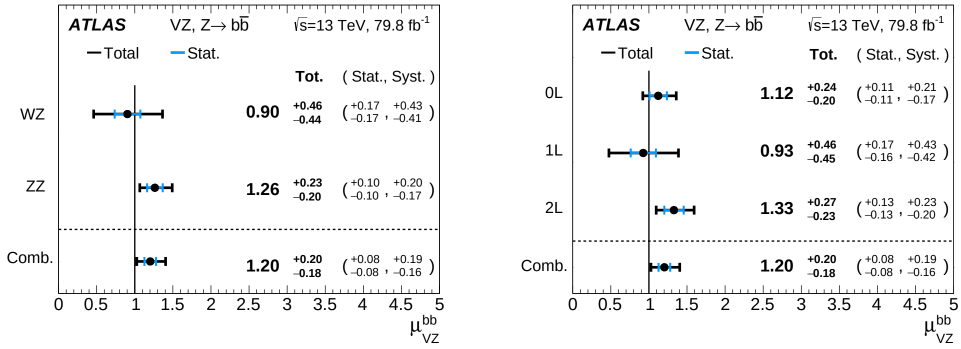

(a) **(b)**

Figure 2.14: The fitted values of the VZ signal strength μ_{VZ}^{bb} (a) for the WZ and ZZ processes and their combination and (b) for the 0-, 1- and 2-lepton channels and for their combination. The individual μ_{VZ}^{bb} values for the $(W/Z)Z$ processes (0-, 1- and 2-lepton channels) are obtained from a simultaneous fit with the signal strengths for each of the WZ and ZZ processes (0-, 1- and 2-lepton channels) floating independently.

Chapter 3

Combinations and differential cross-section measurements

The analysis of 80 fb^{-1}of Run-2 data leads to a very strong evidence for the $VH, H \to b\bar{b}$ signal with 4.9 standard deviations and an uncertainty in μ^{bb}_{VH} of 0.26. While the standard of 5.0 standard deviations to claim an observation is purely conventional, and is probably not well justified when it comes to observing a new production process or a new decay mode predicted by the Standard model for an already observed particle, it is still interesting to try to push the sensitivity as high as possible to get a more precise measurement of the process. This is achieved through the statistical combination of this result with related ones, by multiplying their likelihood functions with a proper treatment of the constraint terms to account for correlations. Three measurements are performed. The best precision on the $VH, H \to b\bar{b}$ process is achieved through the combination with the result of the analysis of the 7 TeV and 8 TeV data. Further knowledge on the $H \to b\bar{b}$ decays is obtained by combining with the searches performed in the vector boson fusion and in the top-quark associated production modes. Finally the highest sensitivity on the VH production process is obtained through a combination with the $H \to \gamma\gamma$ and $H \to ZZ^* \to 4\ell$ analyses. These different combinations are described in section 3.1, and their results are presented in section 3.2.

The uncertainty of 0.26 achieved in μ^{bb}_{VH} by the analysis of the Run-2 data is low enough that the measurement of first differential cross-sections in this channel is possible with decent uncertainty in each measured bin. This measurement is performed in the kinematic fiducial volumes defined in the STXS framework, which as shown in section 1.4.2 categorises the events first as function of the vector boson transverse momentum, then as function of the number of additional jets. This measurement is described in section 3.3, and its results are presented in section 3.4. These results are then interpreted in the context of an effective field theory lagrangian in section 3.5.

3.1 Combinations

3.1.1 Combination of $VH(b\bar{b})$ results

The results of the analysis of the 13 TeV data are statistically combined with that of the Run-1 search using 7 TeV and 8 TeV data [51]. Studies were performed in the context of the previous analysis of the Run-2 data with 36 fb^{-1} [53] to estimate the impact of the choices of correlations of nuisance parameters between the two analysis on the combined result, and the same resulting correlation scheme is adopted for this combination. Indeed, while a correct treatment of the correlations is needed in order not to bias the results, it is often difficult to fully justify the choices made, so specific studies are conducted to estimate the potential biases for the dominant uncertainty sources.

The only simple case is that of the Higgs boson signal theory uncertainties, some of which were treated consistently between the Run-1 and Run-2 analysis and are thus correlated: it concerns the uncertainties in the overall cross-section, in the $H \to b\bar{b}$ branching fraction and in the p_{T}^{V}-dependent NLO EW corrections. The significant uncertainties in the parton shower and underlying event are not correlated as different Monte Carlo generators were used in the two analyses.

The leading experimental uncertainties are those on the b-tagging efficiencies. The modifications of the ATLAS detector (with the inclusion of the insertable B-layer detector), the large improvement in the tagging discriminant variable, and in the b-tagging calibration analyses support the choice of neglecting the correlations affecting the b-tagging uncertainties across the two analyses. Correlation tests were nevertheless conducted and found an effect of less than 5% on the central value, with a negligible impact on the combined uncertainty. The jet energy calibration analyses were performed consistently between Run-1 and Run-2, and consequently well-defined correlations hypotheses can be made between the corresponding sets of nuisance parameters. Different schemes were tested, without any significant impact on the combined result. The chosen solution only correlates the b-jet-specific jet energy scale uncertainty across the two analyses.

While the background modelling uncertainties have a significant impact on the result, studying the effect of potential correlations is difficult due to the changes in centre-of-mass energy, Monte Carlo generators, ATLAS simulation and reconstuction, and object and event selections. It is however expected that the potential impact of underestimating correlations may not be large, as each uncertainty constitutes a small fraction of the total uncertainty. An estimation of the potential effect of correlations is obtained by performing a χ^2-combination of the two measurements of the signal strength. This combination uses the breakdown of the total uncertainty in each measurement in categories as shown in table 2.10 and neglects the correlations between the categories. This allows to introduce simple linear correlations for a given category between the two analyses. The linear correlations coefficients for the $t\bar{t}$, $Z+$hf and $W+$hf uncertainties are varied from 0 (no correlation) to 1 (full correlation), with an impact on the combined signal strength always smaller than 1% and an effect on the signal strength uncertainty smaller than 4%.

3.1.2 Combination of $H \to b\bar{b}$ results

The previous result is further combined with the results of the latest searches for the $H \to b\bar{b}$ decays available at the time of the publication in the $t\bar{t}H$ [60, 62] and in the VBF [55, 57] production modes, using Run-1 and Run-2 data. The analysis targetting the VBF production mode has a sizable contribution from gluon fusion events and is therefore referred to as the VBF+ggF analysis in the following. The combination assumes the cross-sections of the production modes to be as predicted by the SM to measure the ratio of the branching fraction of the Higgs boson into b-quarks to the SM prediction.

The uncertainty in the $H \to b\bar{b}$ branching fraction that affects the SM prediction is correlated across the six analyses. The other correlations of nuisance parameters across analyses follow the studies conducted for the $VH(b\bar{b})$ combination discussed above, for the combination of Run-1 results [20], that of Run-2 results [30] and that of analyses of the $t\bar{t}H$ production mode [32].

3.1.3 Combination of *VH* results

The sensitivity to the *VH* measurement is maximised by combining the results of the Run-2 *VH*($b\bar{b}$) analysis with those from analyses of the Higgs boson decaying into two photons or into four charged leptons (via ZZ^*). The Run-1 analyses are not used in this case due to the additional work required to perform a correct combination in the $\gamma\gamma$ and in the 4ℓ channels. Both analyses are preliminary results [176, 177] that extend to the 80 fb^{-1}dataset the measurements previously published using 36 fb^{-1}of 13 TeV data [178, 179]. The combination with the *VH*($b\bar{b}$) analysis assumes the branching fractions to be as predicted by the SM to measure the signal strength of the *VH* production mode, following the methodology and correlation schemes developed for the ATLAS-wide combination of Higgs boson results [30]. Both analyses in the di-photon and four-leptons final states having sensitivities to all Higgs boson production modes, the signal strengths for the non-VH modes are left floating in the combined fit.

3.2 Results of combinations

3.2.1 Run-1 and Run-2 combination for $VH, H \to b\bar{b}$

The signal strength measured in this combination is:

$$\mu_{VH}^{bb} = 0.98^{+0.22}_{-0.21} = 0.98 \pm 0.14(\text{stat.})^{+0.17}_{-0.16}(\text{syst.}).$$

An excess over the background-only hypothesis is observed with a p_0 value of $5.5 \cdot 10^{-7}$, corresponding to 4.9 standard deviations, to be compared with an expectation of 5.1 standard deviations. A simultaneous fit to the ZH and WH signal strengths yields the values shown on fig. 3.1a, with a probability of compatibility between the two values of 72%. The linear correlation between them is very small, as evidenced by the likelihood contour of fig. 3.1b.

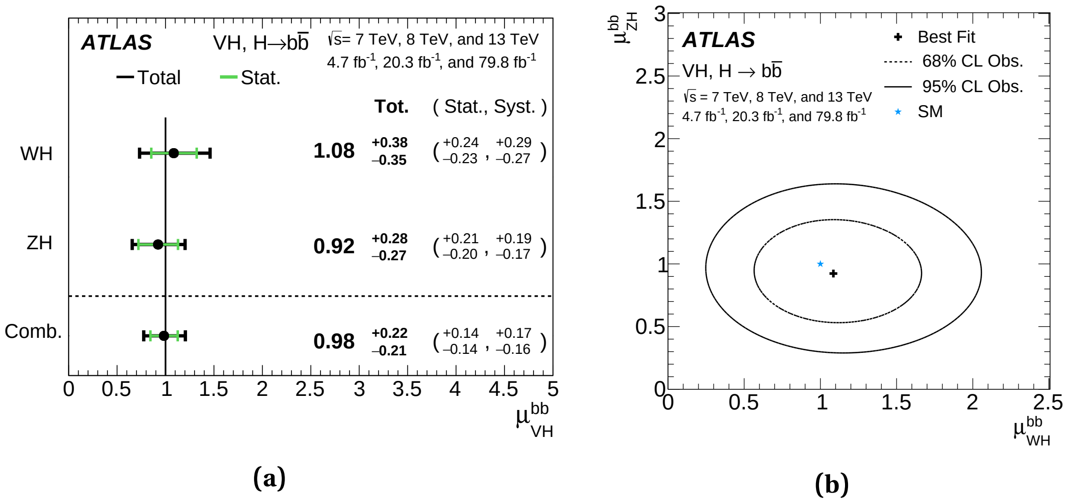

Figure 3.1: (a) The fitted values of the Higgs boson signal strength μ_{VH}^{bb} for m_H = 125 GeV for the WH and ZH processes and their combination in the joint analysis of the 7 TeV, 8 TeV and 13 TeV data. (b) Likelihood contours for the Higgs boson signal strengths μ_{WH}^{bb} and μ_{ZH}^{bb}, for the WH and ZH processes respectively.The best-fit result (+) and the SM expectation (*) are also indicated.

3.2.2 Observations of $H \to b\bar{b}$ decays

The combination of the *VH*($b\bar{b}$) results with those from the searches in the VBF and in the $t\bar{t}H$ production modes leads to an observed significance of the $H \to b\bar{b}$ decay of 5.4 standard deviations compared to an expectation of 5.5 standard deviations, for a Higgs boson mass of 125 GeV and assuming the relative production cross-sections are those predicted by the SM. With the additional assumption that the absolute production cross-sections are those predicted by the SM, the measured signal strength is that of the branching fraction into b-quark pairs:

$$\mu_{H\to bb} = 1.01 \pm 0.20 = 1.01 \pm 0.12(\text{stat.})^{+0.16}_{-0.15}(\text{syst.}).$$

The significance values for the VBF+ggF, $t\bar{t}H$ and *VH* channels and their combination are shown in table 3.1. The search in the *VH* production mode is dominating the sensitivity, with a measurable contribution from the $t\bar{t}H$ analysis, and a smaller one from the VBF+ggF analysis. The individual signal strengths for the production modes obtained from a fit where they are measured simultaneously are displayed in fig. 3.2. The values are compatible with each other, with a probability evaluated at 83%. A fit where the signal strengths are measured independently for each of the production modes in both Run-1 and Run-2 shows a probability of compatibility of the six measurements of 54%.

Table 3.1: Expected and observed significance values (in standard deviations) for the $H \to b\bar{b}$ channels fitted independently and their combination using the 7 TeV, 8 TeV and 13 TeV data.

Channel	Significance	
	Exp.	Obs.
VBF+ggF	0.9	1.5
$t\bar{t}H$	1.9	1.9
VH	5.1	4.9
$H \to b\bar{b}$ combination	5.5	5.4

3.2.3 Observation of VH production

The combination of the Run-2 VH, $H \to b\bar{b}$ result with those from the Run-2 analyses in the di-photon and four-leptons final states leads to an observed significance for *VH* production of 5.3 standard deviations, to be compared to an expectation of 4.8 standard deviations, for a Higgs boson mass of 125 GeV and assuming the relative branching fractions of the three decay modes are as predicted by the SM. With the additional assumption that the absolute branching fractions are those predicted by the SM, the measured signal strength is that of the *VH* production:

$$\mu_{VH} = 1.13^{+0.24}_{-0.23} = 1.13 \pm 0.15(\text{stat.})^{+0.18}_{-0.17}(\text{syst.}).$$

The significance values in the $H \to b\bar{b}$, $H \to \gamma\gamma$ and $H \to ZZ^* \to 4\ell$ decay modes and their combination are shown in table 3.2. The search in the $b\bar{b}$ final state is dominating the sensitivity, with a measurable contribution from the di-photon final state, and a smaller one from the analysis in the four-lepton channel. The individual signal strengths for the decay modes obtained from a fit where they are measured simultaneously are displayed in fig. 3.3. The values are compatible with each other, with a probability evaluated at 96%.

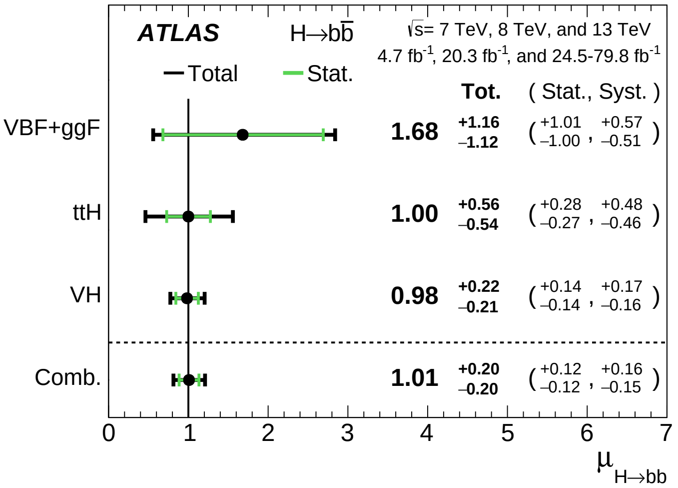

Figure 3.2: The fitted values of the Higgs boson signal strength $\mu_{H\to bb}$ for $m_H = 125$ GeV separately for the VH, $t\bar{t}H$ and VBF+ggF analyses along with their combination, using the 7 TeV, 8 TeV and 13 TeV data. The individual $\mu_{H\to bb}$ values for the different production modes are obtained from a simultaneous fit with the signal strengths for each of the processes floating independently.

Table 3.2: Expected and observed significance values (in standard deviations) for the VH production channels from the combined fit and from a combined fit where each of the lepton channels has its own signal strength, using 13 TeV data.

Channel	Significance	
	Exp.	Obs.
$H \to ZZ^* \to 4\ell$	1.1	1.1
$H \to \gamma\gamma$	1.9	1.9
$H \to b\bar{b}$	4.3	4.9
VH combined	4.8	5.3

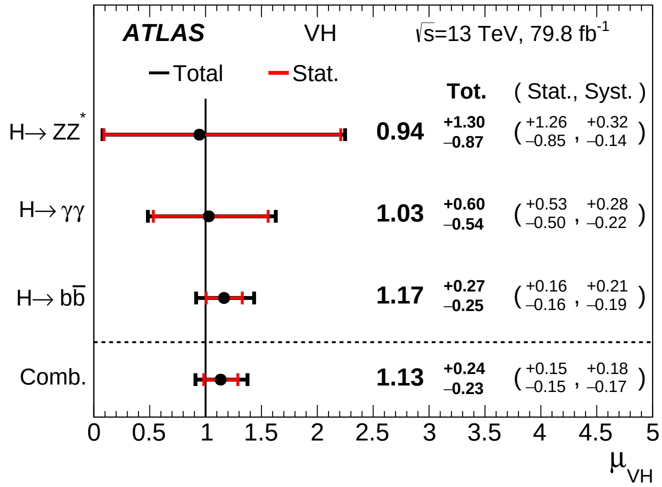

Figure 3.3: The fitted values of the Higgs boson signal strength μ_{VH} for $m_H = 125$ GeV separately for the $H \to b\bar{b}$, $H \to \gamma\gamma$ and $H \to ZZ^* \to 4\ell$ decay modes, along with their combination. The individual μ_{VH} values for the different decay modes are obtained from a simultaneous fit with the signal strengths for each of the processes floating independently.

3.3 Measurement of VH, $H \to b\bar{b}$ as function of the vector-boson transverse momentum

As explained in section 1.2, the framework of simplified template cross-sections has been introduced to probe the kinematic properties of Higgs boson production, to reduce the impact of theoretical uncertainties on the measurements and to make the measurements easier to compare with future updated calculations. In the case of *VH* production, the exclusive fiducial regions (also called STXS bins) in which the measurements are made have been selected to map the kinematic properties of the Higgs boson production with criteria close to those used in the analysis in order to reduce the extrapolation: as shown in section 1.4.2 each production mode is binned across the transverse momentum of the associated vector boson, and in the number of additional particle-level jets with $p_{\mathrm{T}} > 30\,\mathrm{GeV}$.

As the sensitivity of the *VH*($b\bar{b}$) analysis is not sufficient to measure simultaneously the cross-sections in all STXS bins, the fiducial regions are combined together so that the uncertainty in the measurements stay near or below 100%. As there is little discrimination between the $gg \to ZH$ and $qq \to ZH$ processes kinematics in a given STXS ($p_{\mathrm{T}}^{V}, N_{\mathrm{jet}}$) bin, the corresponding regions in these two production processes are merged together. The STXS bins differing only by their number of particle-jets are also merged together, as the categorisation across p_{T}^{V} carries more information to constrain possible new physics than the number of additional jets. Two sets of regions reflecting the sensitive phase-space of the *VH*($b\bar{b}$) analysis are considered. The first one is referred to as the 5-POI (parameters of interest) scheme and simultaneously measures three cross-sections for ZH production ($75\,\mathrm{GeV} < p_{\mathrm{T}}^{Z} < 150\,\mathrm{GeV}$, $150\,\mathrm{GeV} < p_{\mathrm{T}}^{Z} < 250\,\mathrm{GeV}$ and $p_{\mathrm{T}}^{Z} > 250\,\mathrm{GeV}$) and two for WH production ($150\,\mathrm{GeV} < p_{\mathrm{T}}^{W} < 250\,\mathrm{GeV}$ and $p_{\mathrm{T}}^{W} > 250\,\mathrm{GeV}$). The other one is referred to as the 3-POI scheme and simultaneously measures two cross-sections for ZH production ($75\,\mathrm{GeV} < p_{\mathrm{T}}^{Z} < 150\,\mathrm{GeV}$ and $p_{\mathrm{T}}^{V} > 150\,\mathrm{GeV}$) and one for WH production ($p_{\mathrm{T}}^{W} > 150\,\mathrm{GeV}$). These definitions of STXS regions are recalled in table 3.3, which relates them to the corresponding most sensitive analysis regions. To avoid any confusion between the particle-level p_{T}^{V} quantity used in the definition of the STXS bins, and the reconstructed quantity used in the analysis selections and region definitions, the latter will be referred to as $p_{\mathrm{T}}^{V,\mathrm{r}}$ hereafter. The measurements in the 5-POI scheme have by construction larger uncertainties than those in the 3-POI scheme, but are more sensitive to potential high-p_{T}^{V} anomalous contributions to the interaction vertex between the Higgs boson and the weak gauge bosons.

Table 3.3: The 3-POI and 5-POI sets of merged regions used for the measurements, the corresponding kinematic regions of the VH simplified template cross-sections, and the reconstructed-event categories that are most sensitive in each merged region. The regions WH, $p_{\mathrm{T}}^{W} < 150$ GeV, $q\bar{q} \to ZH$, $p_{\mathrm{T}}^{Z} < 75$ GeV and $gg \to ZH$, $p_{\mathrm{T}}^{Z} < 75$ GeV, in which the current analysis is not sensitive and whose corresponding cross-sections are fixed to the SM prediction in the fit, are not shown.

Merged region 3-POI scheme	Merged region 5-POI scheme	STXS region	Reconstructed-event categories with largest sensitivity		
			N_{lep}	$p_{\mathrm{T}}^{V,\mathrm{r}}$ interval	N_{jet}
WH, $p_{\mathrm{T}}^{W} > 150$ GeV	WH, $150 < p_{\mathrm{T}}^{W} < 250$ GeV	$q\bar{q} \to WH$, $150 < p_{\mathrm{T}}^{W} < 250$ GeV, 0-jet $q\bar{q} \to WH$, $150 < p_{\mathrm{T}}^{W} < 250$ GeV, ≥ 1-jet	1	> 150 GeV	2, 3
	WH, $p_{\mathrm{T}}^{W} > 250$ GeV	$q\bar{q} \to WH$, $p_{\mathrm{T}}^{W} > 250$ GeV			
ZH, $75 < p_{\mathrm{T}}^{Z} < 150$ GeV	ZH, $75 < p_{\mathrm{T}}^{Z} < 150$ GeV	$q\bar{q} \to ZH$, $75 < p_{\mathrm{T}}^{Z} < 150$ GeV $gg \to ZH$, $75 < p_{\mathrm{T}}^{Z} < 150$ GeV	2	75–150 GeV	2, ≥ 3
ZH, $p_{\mathrm{T}}^{Z} > 150$ GeV	ZH, $150 < p_{\mathrm{T}}^{Z} < 250$ GeV	$q\bar{q} \to ZH$, $150 < p_{\mathrm{T}}^{Z} < 250$ GeV, 0-jet $gg \to ZH$, $150 < p_{\mathrm{T}}^{Z} < 250$ GeV, 0-jet $q\bar{q} \to ZH$, $150 < p_{\mathrm{T}}^{Z} < 250$ GeV, ≥ 1-jet $gg \to ZH$, $150 < p_{\mathrm{T}}^{Z} < 250$ GeV, ≥ 1-jet	0 2	> 150 GeV > 150 GeV	2, 3 2, ≥3
	ZH, $p_{\mathrm{T}}^{Z} > 250$ GeV	$q\bar{q} \to ZH$, $p_{\mathrm{T}}^{Z} > 250$ GeV $gg \to ZH$, $p_{\mathrm{T}}^{Z} > 250$ GeV			

While the analysis regions in the three lepton channels are defined inclusively for $p_{\mathrm{T}}^{V,\mathrm{r}} > 150\,\mathrm{GeV}$, some discrimination between the STXS bins $150\,\mathrm{GeV} < p_{\mathrm{T}}^{V} < 250\,\mathrm{GeV}$ and $p_{\mathrm{T}}^{V} > 250\,\mathrm{GeV}$ is provided by the BDT_{VH} distributions. Indeed, since $p_{\mathrm{T}}^{V,\mathrm{r}}$ is one of the most important variables in the training of the BDTs along with m_{bb} and the angular separation between the b-jets, it is largely correlated with the BDT_{VH} output. This is shown in fig. 3.4 for the 2-lepton channel, where the BDT_{VH} distribution for the $p_{\mathrm{T}}^{Z} > 250\,\mathrm{GeV}$ STXS bin peaks at the highest values, while that of the $150\,\mathrm{GeV} < p_{\mathrm{T}}^{Z} < 250\,\mathrm{GeV}$ category has a broader distribution between -0.3 and 0.8. The same pattern appears in the 0- and 1-lepton channels.

The likelihood function used in the inclusive $VH(b\bar{b})$ analysis is only slightly modified to allow for these cross-section measurements in the STXS framework. In particular the backgrounds and the associated uncertainties are the same. Only the signal treatment is modified. Instead of using a single signal template in each analysis region, one template is introduced for each STXS region under study, with a corresponding parameter of interest. The overall theoretical cross-section and branching fraction uncertainties which affect the signal strength measurements are not included. Consequently the parameters of interest are ratios of the measured cross-sections to the corresponding SM prediction.

The acceptance for signal events from the five considered STXS categories in each analysis region are shown in fig. 3.5a, while the fraction of signal events in each analysis region originating from the different STXS bins is shown in fig. 3.5b. The relatively low acceptance values are explained by the product of the b-tagging efficiency (around 50% for two b-tagged jets), the low acceptance to τ-lepton decays of the vector bosons, the veto of events with > 3 jets in the 0- and 1-lepton channels, and the selection efficiencies of charged leptons and jets. The low acceptance for the STXS bins with $p_{\mathrm{T}}^{V} < 150\,\mathrm{GeV}$ in the analysis regions with $p_{\mathrm{T}}^{V,\mathrm{r}} > 150\,\mathrm{GeV}$ is expected to yield low correlations between the parameters of interest corresponding to the bins below or above 150 GeV, a benefit

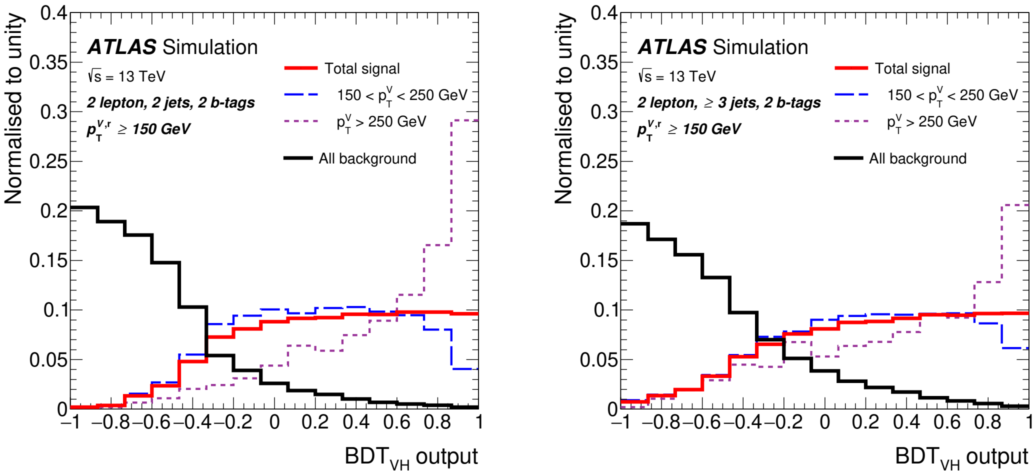

(a) **(b)**

Figure 3.4: BDT$_{VH}$ distributions for different p_T^V STXS regions in the 2-lepton, $p_T^{V,r} > 150$ GeV 2-jet (a) and 3-jet (b) analysis regions. Only STXS bins contributing at least 10% of the expected signal yield in the analysis region are displayed. The distributions of the total signal and background are also shown. The BDT$_{VH}$ distributions are scaled to the same (unit) area to highlight the shape differences.

coming from the alignment of the STXS bin definitions and the analysis categorisation. As expected from the experimental resolution on $p_T^{V,r}$ coming from the resolutions of the energy measurement of charged leptons and of missing transverse energy, a better purity is achieved in the 2-lepton channel than in the 0-lepton or in the 1-lepton channels. Conversely, since the separation between the STXS bins below or above 250 GeV comes only from the BDT$_{VH}$ distributions sizable anti-correlations between their measurements is expected. As the acceptance to WH events with $p_T^W < 150$ GeV and to ZH events with $p_T^Z < 75$ GeV is below 0.1% in each region, the analysis is not sensitive to them, and their cross-section is therefore constrained in the fit to the SM prediction within the theoretical uncertainties. This assumption has a negligible impact on the final results: setting them to 70% of the prediction (about seven times the nominal uncertainty) changes the measured cross-sections of the STXS bins of interest by less than 1%.

While the theoretical cross-section uncertainties do not affect by construction the cross-section measurements and are only included in the theoretical predictions when they are compared to the measured values, the uncertainties affecting the acceptance and shape of the kinematic distributions have to be included. The estimations of the theoretical uncertainties discussed in section 1.4.2 are therefore used and merged appropriately to correspond to the 3-POI and 5-POI schemes. The total uncertainties due to missing higher-order terms are about 4% for the $qq \to VH$ processes and about 40% for the $gg \to ZH$ process, while the uncertainties due to α_S and to the PDF amount to 2% to 3% depending on the STXS category.

3.4 Results of the differential cross-section measurements

The measured cross-sections in the STXS bins multiplied by the $H \to b\bar{b}$ branching fraction in both the 3-POI and the 5-POI schemes are shown in table 3.4 along with the SM predictions and their uncertainties. The breakdown of the uncertainties in the measurements is obtained with the same procedure as in the inclusive case. Therefore the total systematic uncertainty differs from the sum

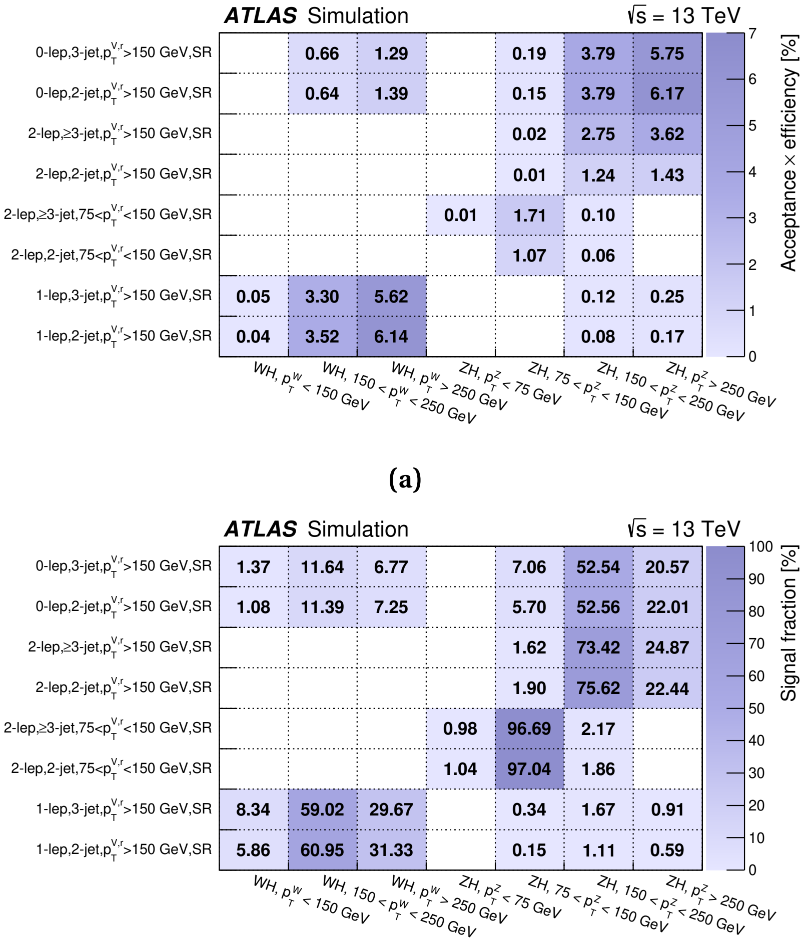

(a)

(b)

Figure 3.5: In the 5-POI scheme, (a) the acceptance (including the efficiency of the experimental selection) for VH, $V \to$ leptons, $H \to b\bar{b}$ events of each analysis region (y-axis) for each STXS signal bin (x-axis), in percent; (b) the fraction of signal (in percent) from each STXS bin (x-axis) in every analysis region (y-axis). Entries with acceptance times efficiency below 0.01% or signal fractions below 0.1% are not shown.

in quadrature of the uncertainties in the modelling of the signal process, of those in the modelling of the background processes and of those of experimental nature because of correlations. The measurements in the 5-POI scheme are also displayed in fig. 3.6. In both cases, the measurements agree with the SM predictions.

The uncertainties in the measurements vary between 50% and 125% in the 5-POI scheme, and between 29% and 56% in the 3-POI scheme. Statistical uncertainties dominate, except for the WH cross-sections with $p_{\mathrm{T}}^{W} > 150\,\mathrm{GeV}$ in the 3-POI case and with $150\,\mathrm{GeV} < p_{\mathrm{T}}^{W} < 250\,\mathrm{GeV}$ in the 5-POI case. The dominant systematic uncertainties are due to the modelling of the background processes and to the limited size of the simulated samples. The uncertainties due to the modelling of the signal processes are smaller, with an impact between 6% and 12%. The uncertainties in the SM predictions are 2-3 times larger for ZH than for WH because of the large uncertainties from missing higher-order corrections in the $gg \to ZH$ process.

Table 3.4: Best-fit values and uncertainties for the VH, $V \to$ leptons simplified template cross-sections times the $H \to b\bar{b}$ branching fraction, in the 5-POI (top five rows) and 3-POI (bottom three rows) schemes. The SM predictions for each region are also shown. The contributions to the total uncertainty in the measurements from statistical (Stat. unc.) or systematic uncertainties (Syst. unc.) in the signal modelling (Th. sig.), background modelling (Th. bkg.), and in experimental performance (Exp.) are given separately. All leptonic decays of the weak gauge bosons (including those to τ-leptons, $\ell = e, \mu, \tau$) are considered.

Measurement region	SM prediction	Result	Stat. unc.	Syst. unc. [fb]		
($\lvert y_H \rvert < 2.5$, $H \to b\bar{b}$)	[fb]	[fb]	[fb]	Th. sig.	Th. bkg.	Exp.
		5-POI scheme				
$W \to \ell\nu$; $150 < p_{\mathrm{T}}^{V} < 250$ GeV	24.0 ± 1.1	20 ± 25	± 17	± 2	± 13	± 9
$W \to \ell\nu$; $p_{\mathrm{T}}^{V} > 250$ GeV	7.1 ± 0.3	8.8 ± 5.2	± 4.4	± 0.5	± 2.5	± 0.9
$Z \to \ell\ell, \nu\nu$; $75 < p_{\mathrm{T}}^{V} < 150$ GeV	50.6 ± 4.1	81 ± 45	± 35	± 10	± 21	± 19
$Z \to \ell\ell, \nu\nu$; $150 < p_{\mathrm{T}}^{V} < 250$ GeV	18.8 ± 2.4	14 ± 13	± 11	± 1	± 6	± 3
$Z \to \ell\ell, \nu\nu$; $p_{\mathrm{T}}^{V} > 250$ GeV	4.9 ± 0.5	8.5 ± 4.0	± 3.7	± 0.8	± 1.2	± 0.6
		3-POI scheme				
$W \to \ell\nu$; $p_{\mathrm{T}}^{V} > 150$ GeV	31.1 ± 1.4	35 ± 14	± 9	± 2	± 9	± 4
$Z \to \ell\ell, \nu\nu$; $75 < p_{\mathrm{T}}^{V} < 150$ GeV	50.6 ± 4.1	81 ± 45	± 35	± 10	± 21	± 19
$Z \to \ell\ell, \nu\nu$; $p_{\mathrm{T}}^{V} > 150$ GeV	23.7 ± 3.0	28.4 ± 8.1	± 6.4	± 2.4	± 3.6	± 2.3

The observed correlations between the measured cross-sections are shown in fig. 3.7 for both the 3-POI and 5-POI schemes. As expected from the inspection of the signal acceptances and purities, a large anti-correlation of the order of 40%-60% is observed between the cross-sections in the ranges $150\,\mathrm{GeV} < p_{\mathrm{T}}^{V} < 250\,\mathrm{GeV}$ and $p_{\mathrm{T}}^{V} > 250\,\mathrm{GeV}$, while the correlation between the ranges $p_{\mathrm{T}}^{V} < 150\,\mathrm{GeV}$ and $p_{\mathrm{T}}^{V} > 150\,\mathrm{GeV}$ is very small. The anti-correlation between the WH and ZH cross-sections in a given p_{T}^{V} range comes from the sizable acceptance to WH events in the 0-lepton channel.

3.5 Constraints on effective field theory operators

The measurement of the differential cross-sections in the STXS framework is modified to set constraints on effective Lagrangian operators in the SILH basis following the methodology developed in section 1.4.3. The relations between the simplifed template cross-sections and the dimensionless coefficients [97] are implemented in the likelihood function with an appropriate weighting of the STXS bins merged into the measured regions, so that the coefficients $\bar{c}_{HW}$, $\bar{c}_{HB}$, $\bar{c}_{W} - \bar{c}_{B}$ and $\bar{c}_{d}$ can be directly measured in the maximum likelihood fit.

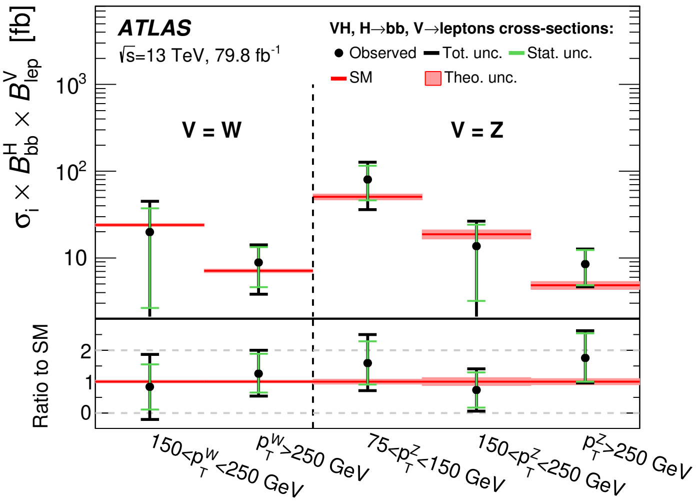

Figure 3.6: Measured VH, $V \rightarrow$ leptons simplified template cross-sections times the $H \rightarrow b\bar{b}$ branching fraction.

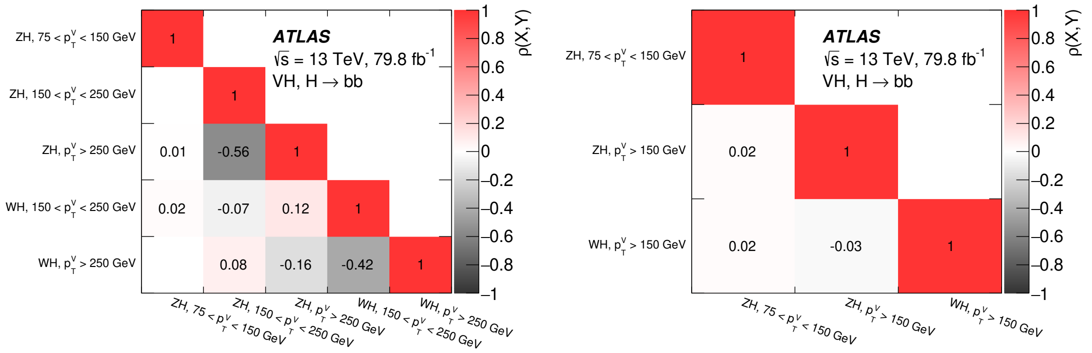

(a)

(b)

Figure 3.7: Observed correlations between the measured simplified template VH, $H \rightarrow b\bar{b}$ cross sections, including both the statistical and systematic uncertainties, in (a) the 5-POI scheme and (b) the 3-POI scheme.

The effect of the SILH operators on the predicted cross-sections in the five measured STXS regions are shown in fig. 3.8 for the values of the corresponding coefficients that are expected to be excluded at 95% confidence level. While the effect of $\mathcal{O}_d$ is the same in all regions since it modifies only the branching fraction of the Higgs boson into b-quark pairs, the sensitivity to the other anomalous couplings depends strongly on p_{T}^V and becomes quite signifiant in the regions with $p_{\mathrm{T}}^V > 250\,\mathrm{GeV}$ compared to the regions $150\,\mathrm{GeV} < p_{\mathrm{T}}^V < 250\,\mathrm{GeV}$. Therefore the constraints are much tighter (by about a factor two) when using the 5-POI scheme rather than the 3-POI scheme.

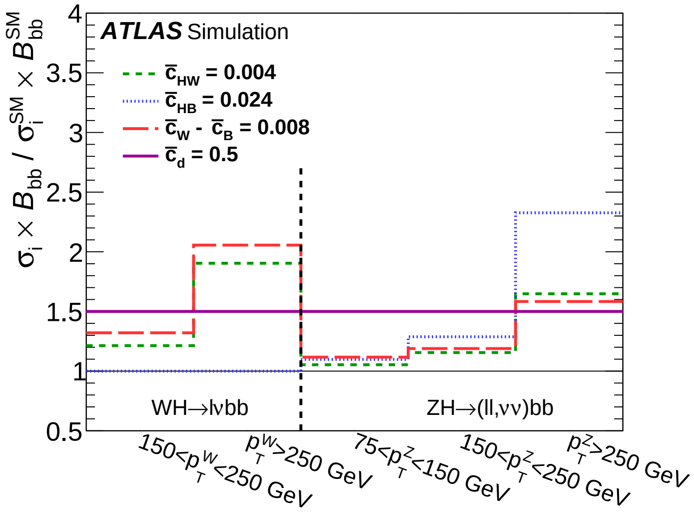

Figure 3.8: Impact on the five simplified template cross sections of the effective Lagrangian operators $\mathcal{O}_{HW}$, $\mathcal{O}_{HB}$, $\mathcal{O}_W$, $\mathcal{O}_B$ and $\mathcal{O}_d$ for the values of the coefficients $\bar{c}_{HW}$, $\bar{c}_{HB}$, $\bar{c}_W - \bar{c}_B$ and $\bar{c}_d$ that are expected to be excluded at 95% confidence level.

The constraints are set on each coefficient one at a time, by assuming all others are zero and inferring the 68% and 95% confidence level (CL) intervals for the coefficient under study. Figure 3.9 shows the observed and expected negative-log-likelihood profiles, and the 68% and 95% CL intervals are summarised in table 3.5. The parameters $\bar{c}_{HW}$ and $\bar{c}_W - \bar{c}_B$ are constrained at 95% CL to be no more than a few percent, while the constraint on $\bar{c}_{HB}$ is about five times worse, and the constraint on $\bar{c}_d$ is of order unity. Comparing to the measurements in the di-photon channel [178] that were also performed in the HEL implementation of the SILH basis, the $VH(b\bar{b})$ analysis has unique sensitivity to $\bar{c}_d$ through the $H \to b\bar{b}$ decays and to $\bar{c}_{HB}$ and $\bar{c}_W - \bar{c}_B$ through ZH production. The sensitivity on $\bar{c}_{HW}$ which is also measured in the di-photon channel is very competitive (better than 1-2% compared to 5%).

Table 3.5 also shows for comparison the 68% and the 95% CL intervals for the dimensionless coefficients when only the interference term (as defined in eq. (1.4)) is considered and the BSM term is neglected. The resulting constraints are typically 50% stronger. A comparison of the observed negative-log-likelihood profiles for two of the coefficients is shown in fig. 3.10. The large impact of the BSM contribution on the likelihood and on the resulting limits questions the assumption that the dimension-8 operators (which are of the same perturbative order $1/\Lambda^4$) can be neglected. Recent progress in the predictions of effective field theories, in particular with the GeoSMEFT approach [180], may allow to test this assumption in the future.

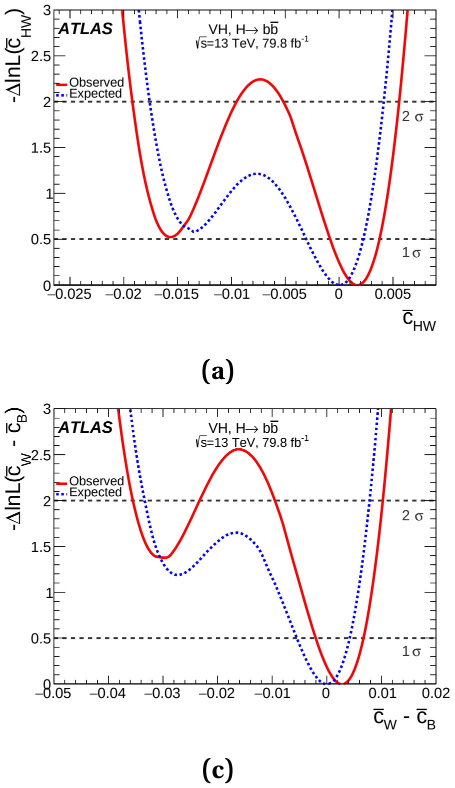

(a) (b)

(c) (d)

Figure 3.9: The observed (solid) and expected (dotted) profiled negative-log-likelihood functions for the one-dimensional fits to constrain the coefficients (a) $\bar{c}_{HW}$, (b) $\bar{c}_{HB}$, (c) $\bar{c}_W - \bar{c}_B$ and (d) $\bar{c}_d$ of the HEL, when the other coefficients are assumed to vanish.

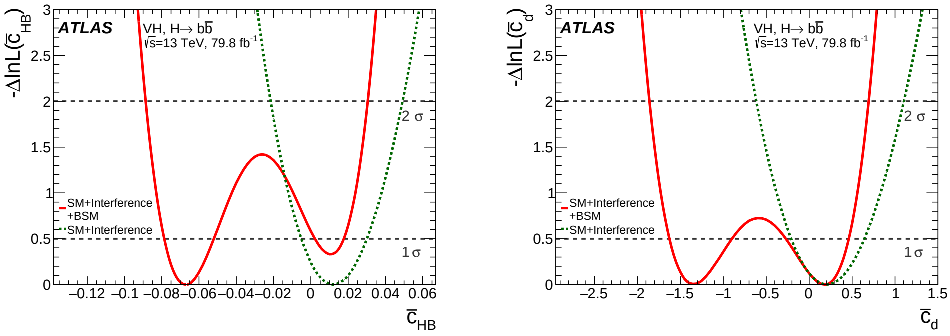

(a) (b)

Figure 3.10: The observed profiled negative log-likelihood functions for the one-dimensional fits to constrain the coefficients (a) $\bar{c}_{HB}$ (b) $\bar{c}_d$ of the HEL, when the other coefficients are assumed to vanish, if both the interference between SM and non-SM amplitudes and the BSM contribution are considered (solid line) or only the interference term (dashed line) on top of the SM prediction.

Table 3.5: The expected and observed 68% CL (four top rows) and 95% CL (four bottom rows) intervals for the effective Lagrangian coefficients $\bar{c}_{HW}$, $\bar{c}_{HB}$, $\bar{c}_W - \bar{c}_B$ and $\bar{c}_d$ when the other coefficients are assumed to vanish. Each row is composed of two sub-rows: the first one uses the interference between SM and non-SM amplitudes and the BSM contributions, while the second sub-row uses only the interference term.

Coefficient	Expected interval	Observed interval
Results at 68% confidence level		
$\bar{c}_{HW}$	[−0.003, 0.002]	[−0.001, 0.004]
(interference only	[−0.002, 0.003]	[−0.001, 0.005])
$\bar{c}_{HB}$	[−0.066, 0.013]	[−0.078, −0.055] ∪ [0.005, 0.019]
(interference only	[−0.016, 0.016]	[−0.005, 0.030])
$\bar{c}_W - \bar{c}_B$	[−0.006, 0.005]	[−0.002, 0.007]
(interference only	[−0.005, 0.005]	[−0.002, 0.008])
$\bar{c}_d$	[−1.5, 0.3]	[−1.6, −0.9] ∪ [−0.3, 0.4]
(interference only	[−0.4, 0.4]	[−0.2, 0.7])
Results at 95% confidence level		
$\bar{c}_{HW}$	[−0.018, 0.004]	[−0.019,−0.010] ∪ [−0.005, 0.006]
(interference only	[−0.005, 0.005]	[−0.003, 0.008])
$\bar{c}_{HB}$	[−0.078, 0.024]	[−0.090, 0.032]
(interference only	[−0.033, 0.033]	[−0.022, 0.049])
$\bar{c}_W - \bar{c}_B$	[−0.034, 0.008]	[−0.036,−0.024] ∪ [−0.009, 0.010]
(interference only	[−0.009, 0.010]	[−0.006, 0.014])
$\bar{c}_d$	[−1.7, 0.5]	[−1.9, 0.7]
(interference only	[−0.8, 0.8]	[−0.6, 1.1])

Chapter 4

Conclusions and perspectives

This document is centered around the search for the Standard Model Higgs boson decaying into a $b\bar{b}$ pair and produced in association with a W or Z boson, performed using 80 fb^{-1} of data collected at a center-of-mass energy of 13 TeV in the first three years of the Run-2 of the LHC by the ATLAS experiment. This search is performed in three channels targetting the leptonic decays of the vector boson, with 0, 1 or 2 charged leptons in the final state, and at least two b-tagged jets to reconstruct a Higgs boson candidate. While the backgrounds such as $V+$ hf or $t\bar{t}$ are much larger than the expected signal, the analysis leverages various techniques to improve the sensitivity of the analysis. The events are split into categories that differ in background composition and signal-to-background ratio. Multivariate techniques are employed to maximally exploit the difference in kinematics between signal and background events. Finally, a lot of attention is put on the systematic uncertainties in the modelling of the background processes in order to estimate them as precisely as possible. At all stages of the analysis, the possible extensions of its phase space (such as the inclusion of channels with τ-leptons) or other potential improvements are critically reviewed to weigh the expected benefits with the induced increased complexity, as managing this complexity is an important element in the timely delivery of the analysis results. The statistical analysis of the data is a critical point in this regard, as the time devoted to the detailed scrutiny of the profile likelihood fit can grow exponentially if overly optimistic decisions are made in the design of the analysis.

An excess over the background is observed in the analysis, with a significance of 4.9 standard deviations compared to an expectation of 4.3, corresponding to a signal strength relative to the SM prediction measured at $\mu_{VH}^{bb} = 1.16 \pm 0.16(\text{stat.})^{+0.21}_{-0.19}(\text{syst.})$. This result is then combined, first with previous results based on the Run-1 dataset, yielding an excess observed with a significance of 4.9 standard deviations for an expectation of 5.1. A further combination with the results for the SM Higgs boson decaying into a pair of b-quarks in the $t\bar{t}H$ and in the VBF+ggF production modes is performed, assuming the relative production cross-sections of the processes to be as predicted by the SM. The observed excess over the predicted SM background has a significance of 5.4 standard deviations compared to an expectation of 5.5, which constitutes the first observation of the $H \to b\bar{b}$ decays. The measured signal strength is $\mu_{H\to bb} = 1.01 \pm 0.12(\text{stat.})^{+0.16}_{-0.15}(\text{syst.})$, perfectly consistent with the value of the Yukawa coupling to bottom quarks in the SM. Finally, a combination of the Run-2 $VH(b\bar{b})$ result is performed with the results of other Run-2 searches in the VH production mode, in either four leptons or diphoton decays. Assuming the relative branching fractions of the three decay modes to be as predicted by the SM, an excess is observed with a significance of 5.3 standard deviations, compared to an expectation of 4.8. This provides the first observation of the associated production of the Higgs boson with a vector boson.

The long search for the Higgs boson decays into b-quark pairs found therefore its conclusion in Summer 2018, and this observation was one of the highlights of the ICHEP 2018 conference [181]. A month later, the CMS collaboration presented a very similar observation [23]: the search in the VH, $H \to b\bar{b}$ channel alone showed an excess of events with a significance of 4.8 standard deviations, and only the combination with the search for $H \to b\bar{b}$ in other production modes allowed to perform an observation with a significance of 5.6 standard deviations, and a measured signal strength 1.04 ± 0.20. Once again, the ATLAS and CMS experiments obtain very similar performance for a Higgs analysis, despite being two completely different detectors and using different analysis techniques (in particular the event categorisation and the Higgs boson mass reconstruction in this case).

Beyond this observation, the sensitivity of the $VH(b\bar{b})$ analysis enables the first measurements of the Higgs boson cross-section in its associated production with a vector boson, as function of the vector boson transverse momentum. The cross-sections are measured in the *Simplified Template Cross-Section* framework in a fiducial volume $|y_H| < 2.5$, in coarse p_{T}^V intervals that lead to relative uncertainties between 30% and 125%. The results are in good agreement with the SM predictions, and are used to set limits on four linear combinations of coefficients of effective Lagrangian operators affecting the Higgs boson couplings to the electroweak bosons and to down-type quarks.

If the results shown in this document are definitely landmarks for the study of the Higgs boson in its decays into b-quark pairs and of the VH production, they can still be improved upon, beyond the simple luminosity increase brought by the full Run-2 dataset. The need for continuous improvements is understood when looking again at table 2.10: the impacts of statistical and systematic uncertainties are of the same order of magnitude, and within systematic uncertainties many sources contribute significantly. The time devoted to the preparation of the publication using the full Run-2 luminosity [3] was therefore spent to improve upon several aspects of the analysis.

An interesting observation about the $t\bar{t}$ background in the 0- and 1-lepton channels is that, as shown for instance in Charles Delporte's thesis [130], the most signal-like events have the Higgs boson candidate reconstructed from a b-quark (coming from a top-quark) and a c-quark coming from the hadronic W decay. Any improvement in the c-jet rejection of the b-tagging algorithm therefore directly impacts the sensitivity of the analysis in these two channels. In addition, furher gain is achieved by adding the b-tagging discriminant scores of the tagged jets as inputs of the analysis multivariate discriminant. This improvement was used in the analysis of the Run-1 data, but could only be reintroduced for the analysis of the full Run-2 dataset given the difficulty to properly calibrate the full b-tagging discriminant distribution for b, c and light-flavour jets.

As the uncertainties in the results decrease in consecutive iterations of the analysis, the background modelling uncertainties need to be set more and more precisely. In particular, the shape effects parametrised in variations of p_{T}^V and m_{bb} may not capture the full shape differences between the samples produced with the nominal and alternative generators. Improvements have been obtained by training boosted decision trees to separate between generators, and parametrising variations in the resulting discriminant variable. The end result are smooth background modelling systematic uncertainties that reproduce shape effects on all kinematic variables. The work leading to this improvement is for instance described in Konie Al Khoury's PhD thesis [4].

Overall, the efforts put into the analysis of the complete Run-2 data allowed to decrease the systematic uncertainties in the measurements sufficiently to keep statistical uncertainties (which have decreased with the larger integrated luminosity) and systematic uncertainties at a similar level. The ZH process has been observed at the 5.3σ level, while a strong evidence for WH has been established at the 4.0σ level. The differential cross-sections have been measured in the five STXS categories with about 30% uncertainty in the higher-p_{T} categories and with low correlations between the measurements.

In addition to bringing more sensitvity to the bulk of the phase space, the larger statistics of the full Run-2 dataset open the possibilities for measurement at higher energies. However the analysis acceptance start to decrease for $p_{\mathrm{T}}^{V} > 400\,\mathrm{GeV}$, as the two b-jets tend to merge into a single large-R jet. A new analysis was therefore set up to look at these boosted topologies with a large-R jet to which two b-tags can be associated. A first exploratory analysis, not orthogonal in selections to the *standard* $VH(b\bar{b})$ analysis, was published [182]. Although its inclusive performance is much worse, the 2-σ sensitivity achieved for $p_{\mathrm{T}}^{V} > 400\,\mathrm{GeV}$ is extremely interesting for the differential measurements of the VH production mode, and for the subsequent constraints on operators in effective Lagrangians. A proper combined analysis taking the best of both the resolved and boosted topologies without any overlap in the phase space is therefore an important goal for the next years.

As the amount of available data will not increase significantly before a few years it is crucial to extract as much information from the Run-2 dataset as possible, building upon the work already performed for these first papers published using the full luminosity. After years of work into this channel, there do not seem to be any low hanging fruits left, so the path forward for the $VH(b\bar{b})$ analysis lies along the three directions mentioned in the previous paragraphs: inclusion of small improvements to squeeze a little bit of sensitivity, work on all sources of systematic uncertainties to try reducing them, and inclusion of the boosted topologies to extend the sensitivity at higher energies. New measurements, such as that of the CP structure of the HVV vertex, can also be attempted. In all cases, it will be important to keep in mind that the statistical analysis and more precisely the quality of the likelihood function should remain under control, as adding complexity in an already complex analysis with low signal-to-background ratio can easily lead to significant issues.

On a more personal note, keeping such a long-standing focus on a single analysis brought a lot of satisfaction as I have been able to participate (directly or through the supervision of students) in all aspects of the analysis, and I therefore take some pride in the significant progress that has been achieved in the past years. Maintaining my physics analysis activity on a single topic also allowed me to develop new skills, with an increasing involvement in the ATLAS liquid-argon calorimeter (LAr) electronics upgrade. The whole readout electronics of the calorimeter have to be replaced as part of the Phase-II upgrade of ATLAS for the high-luminosity LHC. My involvement began with the physics requirements for the calorimeter, under the assumptions of 200 pile-up events per bunch-crossing and up to $4000\mathrm{fb}^{-1}$ of integrated luminosity. This led me to set the main specifications for the readout electronics, in particular for the large-dynamic-range low-noise frontend preamplifier/shaper chip. I have then taken in charge the project of this preamplifier/shaper ASIC for the LAr Phase-II upgrade, with the coordination of the R&Ds taking place at BNL and at OMEGA (IN2P3's micro-electronics laboratory), and the direct supervision of the latter. The fact that I now spend half of my research time on this project comes from its necessity for the ATLAS collaboration, but also from a true interest in hardware activities that has grown in the past years, as I enjoy working with engineers to create our future detectors. The balance between physics analysis and detector activities is a key aspect for my interest in keeping working in particle physics at accelerators in the next years.

References

[1] ATLAS Collaboration. “Observation of $H \to b\bar{b}$ decays and VH production with the ATLAS detector.” *Phys. Lett. B* 786 (2018), p. 59. DOI: `10.1016/j.physletb.2018.09.013`. arXiv: `1808.08238 [hep-ex]` (Cited on pages 7, 11, 17)

[2] ATLAS Collaboration. “Measurement of VH, $H \to b\bar{b}$ production as a function of the vector-boson transverse momentum in 13 TeV pp collisions with the ATLAS detector.” *JHEP* 05 (2019), p. 141. DOI: `10.1007/JHEP05(2019)141`. arXiv: `1903.04618 [hep-ex]` (Cited on pages 7, 17)

[3] ATLAS Collaboration. “Measurements of WH and ZH production in the $H \to b\bar{b}$ decay channel in pp collisions at 13 TeV with the ATLAS detector.” *Eur. Phys. J. C* 81.2 (2021), p. 178. DOI: `10.1140/epjc/s10052-020-08677-2`. arXiv: `2007.02873 [hep-ex]` (Cited on pages 8, 17, 90)

[4] Konie Al Khoury. “Measurements of the Higgs boson produced in association with a vector boson and decaying to a pair of b-quarks with the ATLAS detector.” Theses. Université Paris-Saclay, Sept. 2020. URL: `https://tel.archives-ouvertes.fr/tel-03027930` (Cited on pages 8, 90)

[5] Lyndon Evans and Philip Bryant. “LHC Machine.” *JINST* 3 (2008), S08001. DOI: `10.1088/1748-0221/3/08/S08001` (Cited on page 8)

[6] ATLAS Collaboration. “The ATLAS Experiment at the CERN Large Hadron Collider.” *JINST* 3 (2008), S08003. DOI: `10.1088/1748-0221/3/08/S08003` (Cited on page 8)

[7] LHC Higgs Cross Section Working Group, S. Dittmaier, C. Mariotti, G. Passarino, and R. Tanaka (Eds.) “Handbook of LHC Higgs Cross Sections: 1. Inclusive Observables.” *CERN-2011-002* (2011). DOI: `10.5170/CERN-2011-002`. arXiv: `1101.0593 [hep-ph]` (Cited on pages 9, 19)

[8] LHC Higgs Cross Section Working Group, S. Dittmaier, C. Mariotti, G. Passarino, and R. Tanaka (Eds.) “Handbook of LHC Higgs Cross Sections: 2. Differential Distributions.” *CERN-2012-002* (2012). DOI: `10.5170/CERN-2012-002`. arXiv: `1201.3084 [hep-ph]` (Cited on pages 9, 19)

[9] LHC Higgs Cross Section Working Group, S. Heinemeyer, C. Mariotti, G. Passarino, and R. Tanaka (Eds.) “Handbook of LHC Higgs Cross Sections: 3. Higgs Properties.” *CERN-2013-004* (2013). DOI: `10.5170/CERN-2013-004`. arXiv: `1307.1347 [hep-ph]` (Cited on pages 9, 19)

[10] D. de Florian et al. “Handbook of LHC Higgs Cross Sections: 4. Deciphering the Nature of the Higgs Sector” (2016). DOI: `10.2172/1345634`, `10.23731/CYRM-2017-002`. arXiv: `1610.07922 [hep-ph]` (Cited on pages 9, 12, 14)

[11] F. Englert and R. Brout. "Broken Symmetry and the Mass of Gauge Vector Mesons." *Phys. Rev. Lett.* 13 (9 Aug. 1964), pp. 321–323. DOI: `10.1103/PhysRevLett.13.321`. URL: `http://link.aps.org/doi/10.1103/PhysRevLett.13.321` (Cited on page 9)

[12] P. W. Higgs. "Broken symmetries, massless particles and gauge fields." *Physics Letters* 12 (Sept. 1964), pp. 132–133. DOI: `10.1016/0031-9163(64)91136-9`. URL: `http://dx.doi.org/10.1016/0031-9163(64)91136-9` (Cited on page 9)

[13] M. Tanabashi et al. "Review of Particle Physics." *Phys. Rev. D* 98.3 (2018), p. 030001. DOI: `10.1103/PhysRevD.98.030001` (Cited on page 10)

[14] ATLAS and CMS Collaborations. "Combined Measurement of the Higgs Boson Mass in pp Collisions at $\sqrt{s} = 7$ and 8 TeV with the ATLAS and CMS Experiments." *Phys. Rev. Lett.* 114 (2015), p. 191803. DOI: `10.1103/PhysRevLett.114.191803`. arXiv: `1503.07589 [hep-ex]` (Cited on page 10)

[15] ATLAS Collaboration. "Measurement of the Higgs boson mass in the $H \to ZZ^* \to 4\ell$ and $H \to \gamma\gamma$ channels with $\sqrt{s} = 13$ TeV pp collisions using the ATLAS detector." *Phys. Lett. B* 784 (2018), p. 345. DOI: `10.1016/j.physletb.2018.07.050`. arXiv: `1806.00242 [hep-ex]` (Cited on page 10)

[16] CMS Collaboration. "A measurement of the Higgs boson mass in the diphoton decay channel" (Feb. 2020). arXiv: `2002.06398 [hep-ex]` (Cited on page 10)

[17] ATLAS Collaboration. "Observation of a new particle in the search for the Standard Model Higgs boson with the ATLAS detector at the LHC." *Phys. Lett. B* 716 (2012), p. 1. DOI: `10.1016/j.physletb.2012.08.020`. arXiv: `1207.7214 [hep-ex]` (Cited on page 10)

[18] ATLAS Collaboration. "Observation and measurement of Higgs boson decays to WW^* with the ATLAS detector." *Phys. Rev. D* 92 (2015), p. 012006. DOI: `10.1103/PhysRevD.92.012006`. arXiv: `1412.2641 [hep-ex]` (Cited on page 10)

[19] CMS Collaboration. "Observation of a new boson at a mass of 125 GeV with the CMS experiment at the LHC." *Phys. Lett. B* 716 (2012), p. 30. DOI: `10.1016/j.physletb.2012.08.021`. arXiv: `1207.7235 [hep-ex]` (Cited on page 10)

[20] ATLAS and CMS Collaborations. "Measurements of the Higgs boson production and decay rates and constraints on its couplings from a combined ATLAS and CMS analysis of the LHC pp collision data at $\sqrt{s} = 7$ and 8 TeV." *JHEP* 08 (2016), p. 045. DOI: `10.1007/JHEP08(2016)045`. arXiv: `1606.02266 [hep-ex]` (Cited on pages 10, 11, 17, 76)

[21] ATLAS Collaboration. "Cross-section measurements of the Higgs boson decaying into a pair of τ-leptons in proton–proton collisions at $\sqrt{s} = 13$ TeV with the ATLAS detector." *Phys. Rev. D* 99 (2019), p. 072001. DOI: `10.1103/PhysRevD.99.072001`. arXiv: `1811.08856 [hep-ex]` (Cited on page 10)

[22] CMS Collaboration. "Observation of the Higgs boson decay to a pair of τ leptons." *Phys. Lett. B* 779 (2018), p. 283. DOI: `10.1016/j.physletb.2018.02.004`. arXiv: `1708.00373 [hep-ex]` (Cited on page 10)

[23] CMS Collaboration. "Observation of Higgs Boson Decay to Bottom Quarks." *Phys. Rev. Lett.* 121 (2018), p. 121801. DOI: `10.1103/PhysRevLett.121.121801`. arXiv: `1808.08242 [hep-ex]` (Cited on pages 11, 17, 90)

[24] ATLAS Collaboration. *A search for the dimuon decay of the Standard Model Higgs boson in pp collisions at $\sqrt{s} = 13$ TeV with the ATLAS Detector.* ATLAS-CONF-2019-028. 2019. URL: `https://cds.cern.ch/record/2682155` (Cited on page 11)

[25] CMS Collaboration. "Search for the Higgs Boson Decaying to Two Muons in Proton–Proton Collisions at $\sqrt{s} = 13\,\text{TeV}$." *Phys. Rev. Lett.* 122 (2019), p. 021801. DOI: `10.1103/PhysRevLett.122.021801`. arXiv: `1807.06325 [hep-ex]` (Cited on page 11)

[26] ATLAS Collaboration. "Search for the Decay of the Higgs Boson to Charm Quarks with the ATLAS Experiment." *Phys. Rev. Lett.* 120 (2018), p. 211802. DOI: `10.1103/PhysRevLett.120.211802`. arXiv: `1802.04329 [hep-ex]` (Cited on page 11)

[27] CMS Collaboration. "A search for the standard model Higgs boson decaying to charm quarks." *JHEP* 03 (2020), p. 131. DOI: `10.1007/JHEP03(2020)131`. arXiv: `1912.01662 [hep-ex]` (Cited on page 11)

[28] CMS Collaboration. "Search for the decay of a Higgs boson in the $\ell\ell\gamma$ channel in proton–proton collisions at $\sqrt{s} = 13\,\text{TeV}$." *JHEP* 11 (2018), p. 152. DOI: `10.1007/JHEP11(2018)152`. arXiv: `1806.05996 [hep-ex]` (Cited on page 11)

[29] ATLAS Collaboration. "Searches for the $Z\gamma$ decay mode of the Higgs boson and for new high-mass resonances in pp collisions at $\sqrt{s} = 13\,\text{TeV}$ with the ATLAS detector." *JHEP* 10 (2017), p. 112. DOI: `10.1007/JHEP10(2017)112`. arXiv: `1708.00212 [hep-ex]` (Cited on page 11)

[30] ATLAS Collaboration. "Combined measurements of Higgs boson production and decay using up to $80\,\text{fb}^{-1}$ of proton–proton collision data at $\sqrt{s} = 13\,\text{TeV}$ collected with the ATLAS experiment" (2019). arXiv: `1909.02845 [hep-ex]` (Cited on pages 11, 13, 76, 77)

[31] CMS Collaboration. "Combined measurements of Higgs boson couplings in proton–proton collisions at $\sqrt{s} = 13\,\text{TeV}$." *Eur. Phys. J. C* 79 (2019), p. 421. DOI: `10.1140/epjc/s10052-019-6909-y`. arXiv: `1809.10733 [hep-ex]` (Cited on page 11)

[32] ATLAS Collaboration. "Observation of Higgs boson production in association with a top quark pair at the LHC with the ATLAS detector." *Phys. Lett. B* 784 (2018), p. 173. DOI: `10.1016/j.physletb.2018.07.035`. arXiv: `1806.00425 [hep-ex]` (Cited on pages 11, 76)

[33] CMS Collaboration. "Observation of $t\bar{t}H$ Production." *Phys. Rev. Lett.* 120 (2018), p. 231801. DOI: `10.1103/PhysRevLett.120.231801`. arXiv: `1804.02610 [hep-ex]` (Cited on page 11)

[34] ATLAS Collaboration. "Study of the spin and parity of the Higgs boson in diboson decays with the ATLAS detector." *Eur. Phys. J. C* 75 (2015), p. 476. DOI: `10.1140/epjc/s10052-015-3685-1`. arXiv: `1506.05669 [hep-ex]`. Erratum: Eur. Phys. J. C **76** (2016) 152 (Cited on page 11)

[35] ATLAS Collaboration. "Constraints on off-shell Higgs boson production and the Higgs boson total width in $ZZ \to 4\ell$ and $ZZ \to 2\ell 2\nu$ final states with the ATLAS detector." *Phys. Lett. B* 786 (2018), p. 223. DOI: `10.1016/j.physletb.2018.09.048`. arXiv: `1808.01191 [hep-ex]` (Cited on page 11)

[36] ATLAS Collaboration. "Search for Higgs boson pair production in the $\gamma\gamma b\bar{b}$ final state with 13 TeV pp collision data collected by the ATLAS experiment." *JHEP* 11 (2018), p. 040. DOI: `10.1007/JHEP11(2018)040`. arXiv: `1807.04873 [hep-ex]` (Cited on pages 11, 15)

[37] ATLAS Collaboration. "A search for resonant and non-resonant Higgs boson pair production in the $b\bar{b}\tau^+\tau^-$ decay channel in pp collisions at $\sqrt{s} = 13\,\text{TeV}$ with the ATLAS detector." *Phys. Rev. Lett.* 121 (2018), p. 191801. DOI: `10.1103/PhysRevLett.121.191801`. arXiv: `1808.00336 [hep-ex]` (Cited on pages 11, 15). Erratum: *Phys. Rev. Lett.* 122 (2019), p. 089901. DOI: `10.1103/PhysRevLett.122.089901`

[38] ATLAS Collaboration. *Constraints on the Higgs boson self-coupling from the combination of single-Higgs and double-Higgs production analyses performed with the ATLAS experiment.* ATLAS-CONF-2019-049. 2019. URL: `http://cdsweb.cern.ch/record/2693958` (Cited on page 11)

[39] ATLAS Collaboration. “Search for heavy resonances decaying to a W or Z boson and a Higgs boson in the $q\bar{q}^{(\prime)}b\bar{b}$ final state in pp collisions at $\sqrt{s} = 13\,\text{TeV}$ with the ATLAS detector.” *Phys. Lett. B* 774 (2017), p. 494. DOI: `10.1016/j.physletb.2017.09.066`. arXiv: `1707.06958 [hep-ex]` (Cited on pages 12, 15)

[40] J. R. Andersen et al. “Les Houches 2015: Physics at TeV Colliders Standard Model Working Group Report.” *9th Les Houches Workshop on Physics at TeV Colliders (PhysTeV 2015) Les Houches, France, June 1-19, 2015.* 2016. arXiv: `1605.04692 [hep-ph]`. URL: `http://lss.fnal.gov/archive/2016/conf/fermilab-conf-16-175-ppd-t.pdf` (Cited on page 14)

[41] ATLAS Collaboration. *Constraints on an effective Lagrangian from the combined $H \to ZZ^* \to 4\ell$ and $H \to \gamma\gamma$ channels using 36.1 fb^{-1} of $\sqrt{s} = 13$ TeV pp collision data collected with the ATLAS detector.* ATL-PHYS-PUB-2017-018. 2017. URL: `https://cds.cern.ch/record/2293084` (Cited on page 14)

[42] B. Grzadkowski, M. Iskrzynski, M. Misiak, and J. Rosiek. “Dimension-Six Terms in the Standard Model Lagrangian.” *JHEP* 10 (2010), p. 085. DOI: `10.1007/JHEP10(2010)085`. arXiv: `1008.4884 [hep-ph]` (Cited on page 14)

[43] Adam Falkowski. “Higgs Basis: Proposal for an EFT basis choice for LHC HXSWG” (Mar. 2015). URL: `https://cds.cern.ch/record/2001958` (Cited on page 14)

[44] ATLAS Collaboration. “Measurements of the Higgs boson production and decay rates and coupling strengths using pp collision data at $\sqrt{s} = 7$ and $8\,\text{TeV}$ in the ATLAS experiment.” *Eur. Phys. J. C* 76 (2016), p. 6. DOI: `10.1140/epjc/s10052-015-3769-y`. arXiv: `1507.04548 [hep-ex]` (Cited on pages 15, 16)

[45] ATLAS Collaboration. “Search for heavy resonances decaying into a W or Z boson and a Higgs boson in final states with leptons and b-jets in $36\,\text{fb}^{-1}$ of $\sqrt{s} = 13\,\text{TeV}$ pp collisions with the ATLAS detector.” *JHEP* 03 (2018), p. 174. DOI: `10.1007/JHEP03(2018)174`. arXiv: `1712.06518 [hep-ex]` (Cited on page 15). Erratum: *JHEP* 11 (2018), p. 051. DOI: `10.1007/JHEP11(2018)051`

[46] ATLAS Collaboration. “Search for heavy resonances decaying to a photon and a hadronically decaying $Z/W/H$ boson in pp collisions at $\sqrt{s} = 13\,\text{TeV}$ with the ATLAS detector.” *Phys. Rev. D* 98 (2018), p. 032015. DOI: `10.1103/PhysRevD.98.032015`. arXiv: `1805.01908 [hep-ex]` (Cited on page 15)

[47] ATLAS Collaboration. “Search for non-resonant Higgs boson pair production in the $bb\ell\nu\ell\nu$ final state with the ATLAS detector in pp collisions at $\sqrt{s} = 13\,\text{TeV}$” (2019). arXiv: `1908.06765 [hep-ex]` (Cited on page 15)

[48] ATLAS Collaboration. “Search for pair production of Higgs bosons in the $b\bar{b}b\bar{b}$ final state using proton–proton collisions at $\sqrt{s} = 13\,\text{TeV}$ with the ATLAS detector.” *JHEP* 01 (2019), p. 030. DOI: `10.1007/JHEP01(2019)030`. arXiv: `1804.06174 [hep-ex]` (Cited on page 15)

[49] J. Stirling. 2012. URL: `https://twiki.cern.ch/twiki/pub/LHCPhysics/HiggsEuropeanStrategy2012/` (Cited on page 16)

[50] CDF and D0 Collaborations. “Evidence for a Particle Produced in Association with Weak Bosons and Decaying to a Bottom-Antibottom Quark Pair in Higgs Boson Searches at the Tevatron.” *Phys. Rev. Lett.* 109 (2012), p. 071804. DOI: `10.1103/PhysRevLett.109.071804`. arXiv: `1207.6436 [hep-ex]` (Cited on page 17)

[51] ATLAS Collaboration. “Search for the $b\bar{b}$ decay of the Standard Model Higgs boson in associated $(W/Z)H$ production with the ATLAS detector.” *JHEP* 01 (2015), p. 069. DOI: `10.1007/JHEP01(2015)069`. arXiv: `1409.6212 [hep-ex]` (Cited on pages 17, 32, 35, 44, 60, 61, 75)

[52] CMS Collaboration. "Search for the standard model Higgs boson produced in association with a W or a Z boson and decaying to bottom quarks." *Phys. Rev. D* 89 (2014), p. 012003. DOI: `10.1103/PhysRevD.89.012003`. arXiv: `1310.3687 [hep-ex]` (Cited on page 17)

[53] ATLAS Collaboration. "Evidence for the $H \to b\bar{b}$ decay with the ATLAS detector." *JHEP* 12 (2017), p. 024. DOI: `10.1007/JHEP12(2017)024`. arXiv: `1708.03299 [hep-ex]` (Cited on pages 17, 33, 35, 46–48, 66, 75)

[54] CMS Collaboration. "Evidence for the Higgs boson decay to a bottom quark–antiquark pair." *Phys. Lett. B* 780 (2018), p. 501. DOI: `10.1016/j.physletb.2018.02.050`. arXiv: `1709.07497 [hep-ex]` (Cited on page 17)

[55] ATLAS Collaboration. "Search for the Standard Model Higgs boson produced by vector-boson fusion and decaying to bottom quarks in $\sqrt{s} = 8$ TeV pp collisions with the ATLAS detector." *JHEP* 11 (2016), p. 112. DOI: `10.1007/JHEP11(2016)112`. arXiv: `1606.02181 [hep-ex]` (Cited on pages 17, 76)

[56] CMS Collaboration. "Search for the standard model Higgs boson produced through vector boson fusion and decaying to $b\bar{b}$." *Phys. Rev. D* 92 (2015), p. 032008. DOI: `10.1103/PhysRevD.92.032008`. arXiv: `1506.01010 [hep-ex]` (Cited on page 17)

[57] ATLAS Collaboration. "Search for Higgs bosons produced via vector-boson fusion and decaying into bottom quark pairs in $\sqrt{s} = 13$ TeV pp collisions with the ATLAS detector." *Phys. Rev. D* 98 (2018), p. 052003. DOI: `10.1103/PhysRevD.98.052003`. arXiv: `1807.08639 [hep-ex]` (Cited on pages 17, 76)

[58] ATLAS Collaboration. "Search for Higgs boson production in association with a high-energy photon via vector-boson fusion with decay into bottom quark pairs at $\sqrt{s}$=13 TeV with the ATLAS detector" (Oct. 2020). arXiv: `2010.13651 [hep-ex]` (Cited on page 17)

[59] ATLAS Collaboration. "Measurements of Higgs Bosons Decaying to Bottom Quarks from Vector Boson Fusion Production with the ATLAS Experiment at $\sqrt{s} = 13$ TeV" (Nov. 2020). arXiv: `2011.08280 [hep-ex]` (Cited on page 17)

[60] ATLAS Collaboration. "Search for the Standard Model Higgs boson produced in association with top quarks and decaying into $b\bar{b}$ in pp collisions at $\sqrt{s} = 8$ TeV with the ATLAS detector." *Eur. Phys. J. C* 75 (2015), p. 349. DOI: `10.1140/epjc/s10052-015-3543-1`. arXiv: `1503.05066 [hep-ex]` (Cited on pages 18, 76)

[61] CMS Collaboration. "Search for a standard model Higgs boson produced in association with a top-quark pair and decaying to bottom quarks using a matrix element method." *Eur. Phys. J. C* 75 (2015), p. 251. DOI: `10.1140/epjc/s10052-015-3454-1`. arXiv: `1502.02485 [hep-ex]` (Cited on page 18)

[62] ATLAS Collaboration. "Search for the standard model Higgs boson produced in association with top quarks and decaying into a $b\bar{b}$ pair in pp collisions at $\sqrt{s} = 13$ TeV with the ATLAS detector." *Phys. Rev. D* 97 (2018), p. 072016. DOI: `10.1103/PhysRevD.97.072016`. arXiv: `1712.08895 [hep-ex]` (Cited on pages 18, 76)

[63] CMS Collaboration. "Search for $t\bar{t}H$ production in the $H \to b\bar{b}$ decay channel with leptonic $t\bar{t}$ decays in proton–proton collisions at $\sqrt{s} = 13$ TeV." *JHEP* 03 (2019), p. 026. DOI: `10.1007/JHEP03(2019)026`. arXiv: `1804.03682 [hep-ex]` (Cited on page 18)

[64] ATLAS Collaboration. *Measurement of the Higgs boson decaying to b-quarks produced in association with a top-quark pair in pp collisions at $\sqrt{s} = 13$ TeV with the ATLAS detector.* ATLAS-CONF-2020-058. 2020. URL: `http://cdsweb.cern.ch/record/2743685` (Cited on page 18)

[65] ATLAS Collaboration. “Search for the Standard Model Higgs boson decaying into $b\bar{b}$ produced in association with top quarks decaying hadronically in pp collisions at $\sqrt{s} = 8$ TeV with the ATLAS detector.” *JHEP* 05 (2016), p. 160. DOI: `10.1007/JHEP05(2016)160`. arXiv: `1604.03812 [hep-ex]` (Cited on page 18)

[66] CMS Collaboration. “Search for $t\bar{t}H$ production in the all-jet final state in proton–proton collisions at $\sqrt{s} = 13$ TeV.” *JHEP* 06 (2018), p. 101. DOI: `10.1007/JHEP06(2018)101`. arXiv: `1803.06986 [hep-ex]` (Cited on page 18)

[67] CMS Collaboration. “Inclusive Search for a Highly Boosted Higgs Boson Decaying to a Bottom Quark–Antiquark Pair.” *Phys. Rev. Lett.* 120 (2018), p. 071802. DOI: `10.1103/PhysRevLett.120.071802`. arXiv: `1709.05543 [hep-ex]` (Cited on page 18)

[68] ATLAS Collaboration. *Study of Higgs-boson production with large transverse momentum using the $H \to b\bar{b}$ decay with the ATLAS detector.* ATLAS-CONF-2021-010. 2021. URL: `http://cdsweb.cern.ch/record/2759284` (Cited on page 18)

[69] CMS Collaboration. “Measurement and interpretation of differential cross sections for Higgs boson production at $\sqrt{s} = 13$ TeV.” *Phys. Lett. B* 792 (2019), p. 369. DOI: `10.1016/j.physletb.2019.03.059`. arXiv: `1812.06504 [hep-ex]` (Cited on page 18)

[70] M.L. Ciccolini, S. Dittmaier, and M. Krämer. “Electroweak radiative corrections to associated WH and ZH production at hadron colliders.” *Phys. Rev. D* 68 (2003), p. 073003. DOI: `10.1103/PhysRevD.68.073003`. arXiv: `hep-ph/0306234 [hep-ph]` (Cited on pages 19, 32)

[71] Oliver Brein, Abdelhak Djouadi, and Robert Harlander. “NNLO QCD corrections to the Higgs-strahlung processes at hadron colliders.” *Phys. Lett. B* 579 (2004), pp. 149–156. DOI: `10.1016/j.physletb.2003.10.112`. arXiv: `hep-ph/0307206 [hep-ph]` (Cited on pages 19, 32)

[72] Giancarlo Ferrera, Massimiliano Grazzini, and Francesco Tramontano. “Associated WH production at hadron colliders: a fully exclusive QCD calculation at NNLO.” *Phys. Rev. Lett.* 107 (2011), p. 152003. DOI: `10.1103/PhysRevLett.107.152003`. arXiv: `1107.1164 [hep-ph]` (Cited on pages 19, 32)

[73] Oliver Brein, Robert Harlander, Marius Wiesemann, and Tom Zirke. “Top-quark mediated effects in hadronic Higgs-Strahlung.” *Eur. Phys. J. C* 72 (2012), p. 1868. DOI: `10.1140/epjc/s10052-012-1868-6`. arXiv: `1111.0761 [hep-ph]` (Cited on pages 19, 32)

[74] Giancarlo Ferrera, Massimiliano Grazzini, and Francesco Tramontano. “Higher-order QCD effects for associated WH production and decay at the LHC.” *JHEP* 04 (2014), p. 039. DOI: `10.1007/JHEP04(2014)039`. arXiv: `1312.1669 [hep-ph]` (Cited on pages 19, 32)

[75] Giancarlo Ferrera, Massimiliano Grazzini, and Francesco Tramontano. “Associated ZH production at hadron colliders: the fully differential NNLO QCD calculation.” *Phys. Lett. B* 740 (2015), pp. 51–55. DOI: `10.1016/j.physletb.2014.11.040`. arXiv: `1407.4747 [hep-ph]` (Cited on pages 19, 32)

[76] John M. Campbell, R. Keith Ellis, and Ciaran Williams. “Associated production of a Higgs boson at NNLO.” *JHEP* 06 (2016), p. 179. DOI: `10.1007/JHEP06(2016)179`. arXiv: `1601.00658 [hep-ph]` (Cited on pages 19, 32)

[77] Ansgar Denner, Stefan Dittmaier, Stefan Kallweit, and Alexander Mück. “Electroweak corrections to Higgs-strahlung off W/Z bosons at the Tevatron and the LHC with Hawk.” *JHEP* 03 (2012), p. 075. DOI: `10.1007/JHEP03(2012)075`. arXiv: `1112.5142 [hep-ph]` (Cited on pages 19, 31)

[78] Ansgar Denner, Stefan Dittmaier, Stefan Kallweit, and Alexander Mück. "HAWK 2.0: A Monte Carlo program for Higgs production in vector-boson fusion and Higgs strahlung at hadron colliders." *Comput. Phys. Commun.* 195 (2015), pp. 161–171. DOI: `10.1016/j.cpc.2015.04.021`. arXiv: `1412.5390 [hep-ph]` (Cited on pages 19, 31)

[79] J. de Favereau de Jeneret, V. Lemaitre, Y. Liu, S. Ovyn, T. Pierzchala, K. Piotrzkowski, X. Rouby, N. Schul, and M. Vander Donckt. "High energy photon interactions at the LHC" (2009). arXiv: `0908.2020 [hep-ph]` (Cited on page 19)

[80] Lukas Altenkamp, Stefan Dittmaier, Robert V. Harlander, Heidi Rzehak, and Tom J. E. Zirke. "Gluon-induced Higgs-strahlung at next-to-leading order QCD." *JHEP* 02 (2013), p. 078. DOI: `10.1007/JHEP02(2013)078`. arXiv: `1211.5015 [hep-ph]` (Cited on pages 19, 32)

[81] B. Hespel, F. Maltoni, and E. Vryonidou. "Higgs and Z boson associated production via gluon fusion in the SM and the 2HDM." *JHEP* 06 (2015), p. 065. DOI: `10.1007/JHEP06(2015)065`. arXiv: `1503.01656 [hep-ph]` (Cited on pages 19, 32)

[82] Robert V. Harlander, Anna Kulesza, Vincent Theeuwes, and Tom Zirke. "Soft gluon resummation for gluon-induced Higgs Strahlung." *JHEP* 11 (2014), p. 082. DOI: `10.1007/JHEP11(2014)082`. arXiv: `1410.0217 [hep-ph]` (Cited on pages 19, 32)

[83] Robert V. Harlander, Stefan Liebler, and Tom Zirke. "Higgs Strahlung at the Large Hadron Collider in the 2-Higgs-doublet model." *JHEP* 02 (2014), p. 023. DOI: `10.1007/JHEP02(2014)023`. arXiv: `1307.8122 [hep-ph]` (Cited on pages 19, 32)

[84] Oliver Brein, Robert V. Harlander, and Tom J. E. Zirke. "vh@nnlo - Higgs Strahlung at hadron colliders." *Comput. Phys. Commun.* 184 (2013), pp. 998–1003. DOI: `10.1016/j.cpc.2012.11.002`. arXiv: `1210.5347 [hep-ph]` (Cited on pages 19, 32)

[85] Christoph Englert, Matthew McCullough, and Michael Spannowsky. "Gluon-initiated associated production boosts Higgs physics." *Phys. Rev.* D89.1 (2014), p. 013013. DOI: `10.1103/PhysRevD.89.013013`. arXiv: `1310.4828 [hep-ph]` (Cited on page 20)

[86] Matteo Cacciari, Gavin P. Salam, and Gregory Soyez. "The anti-k_t jet clustering algorithm." *JHEP* 04 (2008), p. 063. DOI: `10.1088/1126-6708/2008/04/063`. arXiv: `0802.1189 [hep-ph]` (Cited on pages 22, 35)

[87] ATLAS Collaboration. *Evaluation of theoretical uncertainties for simplified template cross section measurements of V-associated production of the Higgs boson.* ATL-PHYS-PUB-2018-035. 2018. URL: `https://cds.cern.ch/record/2649241` (Cited on page 23)

[88] Gionata Luisoni, Paolo Nason, Carlo Oleari, and Francesco Tramontano. "$HW^{\pm}$/HZ + 0 and 1 jet at NLO with the POWHEG BOX interfaced to GoSam and their merging within MiNLO." *JHEP* 10 (2013), p. 083. DOI: `10.1007/JHEP10(2013)083`. arXiv: `1306.2542 [hep-ph]` (Cited on pages 23, 31, 32)

[89] Torbjörn Sjöstrand, Stefan Ask, Jesper R. Christiansen, Richard Corke, Nishita Desai, Philip Ilten, Stephen Mrenna, Stefan Prestel, Christine O. Rasmussen, and Peter Z. Skands. "An Introduction to PYTHIA 8.2." *Comput. Phys. Commun.* 191 (2015), p. 159. DOI: `10.1016/j.cpc.2015.01.024`. arXiv: `1410.3012 [hep-ph]` (Cited on pages 23, 31)

[90] ATLAS Collaboration. "Measurement of the Z/γ^* boson transverse momentum distribution in pp collisions at $\sqrt{s} = 7$ TeV with the ATLAS detector." *JHEP* 09 (2014), p. 145. DOI: `10.1007/JHEP09(2014)145`. arXiv: `1406.3660 [hep-ex]` (Cited on pages 23, 31)

[91] Jon Butterworth et al. "PDF4LHC recommendations for LHC Run II." *J. Phys. G* 43 (2016), p. 023001. DOI: `10.1088/0954-3899/43/2/023001`. arXiv: `1510.03865 [hep-ph]` (Cited on pages 23, 31)

[92] Iain W. Stewart and Frank J. Tackmann. “Theory uncertainties for Higgs and other searches using jet bins.” *Phys. Rev.* D85 (2012), p. 034011. DOI: `10.1103/PhysRevD.85.034011`. arXiv: `1107.2117 [hep-ph]` (Cited on pages 24, 53)

[93] G. F. Giudice, C. Grojean, A. Pomarol, and R. Rattazzi. “The Strongly-Interacting Light Higgs.” *JHEP* 06 (2007), p. 045. DOI: `10.1088/1126-6708/2007/06/045`. arXiv: `hep-ph/0703164 [hep-ph]` (Cited on page 24)

[94] Roberto Contino, Margherita Ghezzi, Christophe Grojean, Margarete Muhlleitner, and Michael Spira. “Effective Lagrangian for a light Higgs-like scalar.” *JHEP* 07 (2013), p. 035. DOI: `10.1007/JHEP07(2013)035`. arXiv: `1303.3876 [hep-ph]` (Cited on page 24)

[95] Céline Degrande, Gauthier Durieux, Fabio Maltoni, Ken Mimasu, Eleni Vryonidou, and Cen Zhang. “Automated one-loop computations in the SMEFT” (Aug. 2020). arXiv: `2008.11743 [hep-ph]` (Cited on page 27)

[96] Adam Alloul, Benjamin Fuks, and Verónica Sanz. “Phenomenology of the Higgs effective Lagrangian via FeynRules.” *JHEP* 04 (2014), p. 110. DOI: `10.1007/JHEP04(2014)110`. arXiv: `1310.5150 [hep-ph]` (Cited on page 27)

[97] Chris Hays, Veronica Sanz Gonzalez, and Gabija Zemaityte. “Constraining EFT parameters using simplified template cross sections” (2017). URL: `https://cds.cern.ch/record/2290628` (Cited on pages 27, 84)

[98] John Ellis, Christopher W. Murphy, Verónica Sanz, and Tevong You. “Updated Global SMEFT Fit to Higgs, Diboson and Electroweak Data.” *JHEP* 06 (2018), p. 146. DOI: `10.1007/JHEP06(2018)146`. arXiv: `1803.03252 [hep-ph]` (Cited on page 27)

[99] D.C Kennedy and B.W. Lynn. “Electroweak radiative corrections with an effective lagrangian: Four-fermions processes.” *Nuclear Physics B* 322.1 (1989), pp. 1–54. ISSN: 0550-3213. DOI: `10.1016/0550-3213(89)90483-5`. URL: `https://www.sciencedirect.com/science/article/pii/0550321389904835` (Cited on page 28)

[100] ATLAS Collaboration. “Luminosity determination in pp collisions at $\sqrt{s} = 8\,\text{TeV}$ using the ATLAS detector at the LHC.” *Eur. Phys. J. C* 76 (2016), p. 653. DOI: `10.1140/epjc/s10052-016-4466-1`. arXiv: `1608.03953 [hep-ex]` (Cited on page 31)

[101] ATLAS Collaboration. “The new LUCID-2 detector for luminosity measurement and monitoring in ATLAS.” *JINST* 13.07 (2018), P07017. DOI: `10.1088/1748-0221/13/07/P07017` (Cited on page 31)

[102] Simone Alioli, Paolo Nason, Carlo Oleari, and Emanuele Re. “A general framework for implementing NLO calculations in shower Monte Carlo programs: the POWHEG BOX.” *JHEP* 06 (2010), p. 043. DOI: `10.1007/JHEP06(2010)043`. arXiv: `1002.2581 [hep-ph]` (Cited on pages 31, 32)

[103] Gavin Cullen, Nicolas Greiner, Gudrun Heinrich, Gionata Luisoni, Pierpaolo Mastrolia, Giovanni Ossola, Thomas Reiter, and Francesco Tramontano. “Automated one-loop calculations with GoSam.” *Eur. Phys. J. C* 72 (2012), p. 1889. DOI: `10.1140/epjc/s10052-012-1889-1`. arXiv: `1111.2034 [hep-ph]` (Cited on pages 31, 32)

[104] Keith Hamilton, Paolo Nason, Carlo Oleari, and Giulia Zanderighi. “Merging H/W/Z + 0 and 1 jet at NLO with no merging scale: a path to parton shower + NNLO matching.” *JHEP* 05 (2013), p. 082. DOI: `10.1007/JHEP05(2013)082`. arXiv: `1212.4504 [hep-ph]` (Cited on page 31)

[105] Richard D. Ball et al. “Parton distributions for the LHC Run II.” *JHEP* 04 (2015), p. 040. DOI: `10.1007/JHEP04(2015)040`. arXiv: `1410.8849 [hep-ph]` (Cited on pages 31, 32)

[106] Stefano Frixione, Paolo Nason, and Giovanni Ridolfi. “A Positive-weight next-to-leading-order Monte Carlo for heavy flavour hadroproduction.” *JHEP* 09 (2007), p. 126. DOI: `10.1088/1126-6708/2007/09/126`. arXiv: `0707.3088 [hep-ph]` (Cited on pages 31, 32)

[107] Simone Alioli, Paolo Nason, Carlo Oleari, and Emanuele Re. “NLO single-top production matched with shower in POWHEG: s- and t-channel contributions.” *JHEP* 09 (2009). [Erratum: JHEP 02 (2010) 011], p. 111. DOI: `10.1088/1126-6708/2009/09/111`. arXiv: `0907.4076 [hep-ph]` (Cited on pages 31, 32)

[108] Emanuele Re. “Single-top Wt-channel production matched with parton showers using the POWHEG method.” *Eur. Phys. J. C* 71 (2011), p. 1547. DOI: `10.1140/epjc/s10052-011-1547-z`. arXiv: `1009.2450 [hep-ph]` (Cited on pages 31, 32, 53)

[109] ATLAS Collaboration. *ATLAS Pythia 8 tunes to* 7 *TeV data.* ATL-PHYS-PUB-2014-021. 2014. URL: `https://cds.cern.ch/record/1966419` (Cited on pages 31, 32)

[110] Michal Czakon and Alexander Mitov. “Top++: A Program for the Calculation of the Top-Pair Cross-Section at Hadron Colliders.” *Comput. Phys. Commun.* 185 (2014), p. 2930. DOI: `10.1016/j.cpc.2014.06.021`. arXiv: `1112.5675 [hep-ph]` (Cited on pages 31, 32)

[111] Nikolaos Kidonakis. “Next-to-next-to-leading-order collinear and soft gluon corrections for t-channel single top quark production.” *Phys. Rev. D* 83 (2011), p. 091503. DOI: `10.1103/PhysRevD.83.091503`. arXiv: `1103.2792 [hep-ph]` (Cited on pages 31, 32)

[112] Nikolaos Kidonakis. “NNLL resummation for s-channel single top quark production.” *Phys. Rev. D* 81 (2010), p. 054028. DOI: `10.1103/PhysRevD.81.054028`. arXiv: `1001.5034 [hep-ph]` (Cited on pages 31, 32)

[113] Nikolaos Kidonakis. “Two-loop soft anomalous dimensions for single top quark associated production with a W- or H-.” *Phys. Rev. D* 82 (2010), p. 054018. DOI: `10.1103/PhysRevD.82.054018`. arXiv: `1005.4451 [hep-ph]` (Cited on pages 31, 32)

[114] T. Gleisberg, S. Höche, F. Krauss, M. Schönherr, S. Schumann, et al. “Event generation with SHERPA 1.1.” *JHEP* 02 (2009), p. 007. DOI: `10.1088/1126-6708/2009/02/007`. arXiv: `0811.4622 [hep-ph]` (Cited on page 31)

[115] Fabio Cascioli, Philipp Maierhofer, and Stefano Pozzorini. “Scattering Amplitudes with Open Loops.” *Phys. Rev. Lett.* 108 (2012), p. 111601. DOI: `10.1103/PhysRevLett.108.111601`. arXiv: `1111.5206 [hep-ph]` (Cited on pages 31, 32)

[116] Tanju Gleisberg and Stefan Höche. “Comix, a new matrix element generator.” *JHEP* 12 (2008), p. 039. DOI: `10.1088/1126-6708/2008/12/039`. arXiv: `0808.3674 [hep-ph]` (Cited on pages 31, 32)

[117] Steffen Schumann and Frank Krauss. “A Parton shower algorithm based on Catani-Seymour dipole factorisation.” *JHEP* 03 (2008), p. 038. DOI: `10.1088/1126-6708/2008/03/038`. arXiv: `0709.1027 [hep-ph]` (Cited on pages 31, 32)

[118] Stefan Höche, Frank Krauss, Marek Schönherr, and Frank Siegert. “QCD matrix elements + parton showers: The NLO case.” *JHEP* 04 (2013), p. 027. DOI: `10.1007/JHEP04(2013)027`. arXiv: `1207.5030 [hep-ph]` (Cited on pages 31, 32)

[119] Stefano Catani, Leandro Cieri, Giancarlo Ferrera, Daniel de Florian, and Massimiliano Grazzini. “Vector Boson Production at Hadron Colliders: A Fully Exclusive QCD Calculation at Next-to-Next-to-Leading Order.” *Phys. Rev. Lett.* 103 (2009), p. 082001. DOI: `10.1103/PhysRevLett.103.082001`. arXiv: `0903.2120 [hep-ph]` (Cited on pages 31, 32)

[120] ATLAS Collaboration. “Study of jets produced in association with a W boson in pp collisions at $\sqrt{s} = 7$ TeV with the ATLAS detector.” *Phys. Rev. D* 85 (2012), p. 092002. DOI: `10.1103/PhysRevD.85.092002`. arXiv: `1201.1276 [hep-ex]` (Cited on page 32)

[121] Torbjorn Sjöstrand, Stephen Mrenna, and Peter Z. Skands. “A brief introduction to PYTHIA 8.1.” *Comput. Phys. Commun.* 178 (2008), pp. 852–867. DOI: `10.1016/j.cpc.2008.01.036`. arXiv: `0710.3820 [hep-ph]` (Cited on page 32)

[122] ATLAS Collaboration. “Measurement of the Z/γ^* boson transverse momentum distribution in pp collisions at $\sqrt{s} = 7$ TeV with the ATLAS detector.” *JHEP* 09 (2014), p. 145. DOI: `10.1007/JHEP09(2014)145`. arXiv: `1406.3660 [hep-ex]` (Cited on page 32)

[123] Keith Hamilton, Paolo Nason, and Giulia Zanderighi. “MINLO: multi-scale improved NLO.” *JHEP* 10 (2012), p. 155. DOI: `10.1007/JHEP10(2012)155`. arXiv: `1206.3572 [hep-ph]` (Cited on page 32)

[124] T. Gleisberg et al. “Event generation with SHERPA 1.1.” *JHEP* 02 (2009), p. 007. DOI: `10.1088/1126-6708/2009/02/007`. arXiv: `0811.4622 [hep-ph]` (Cited on page 32)

[125] ATLAS Collaboration. “The ATLAS Simulation Infrastructure.” *Eur. Phys. J. C* 70 (2010), p. 823. DOI: `10.1140/epjc/s10052-010-1429-9`. arXiv: `1005.4568 [physics.ins-det]` (Cited on page 32)

[126] S. Agostinelli et al. “GEANT4: A Simulation toolkit.” *Nucl. Instrum. Meth. A* 506 (2003), p. 250. DOI: `10.1016/S0168-9002(03)01368-8` (Cited on page 32)

[127] ATLAS Collaboration. *Summary of ATLAS Pythia 8 tunes*. ATL-PHYS-PUB-2012-003. 2012. URL: `https://cds.cern.ch/record/1474107` (Cited on page 33)

[128] A. D. Martin, W. J. Stirling, R. S. Thorne, and G. Watt. “Parton distributions for the LHC.” *Eur. Phys. J.* C63 (2009), pp. 189–285. DOI: `10.1140/epjc/s10052-009-1072-5`. arXiv: `0901.0002 [hep-ph]` (Cited on page 33)

[129] D. J. Lange. “The EvtGen particle decay simulation package.” *Nucl. Instrum. Meth. A* 462 (2001), p. 152. DOI: `10.1016/S0168-9002(01)00089-4` (Cited on page 33)

[130] Charles Delporte. “Study of the Higgs boson decay into b-quarks with the ATLAS experiment - run 2.” Theses. Université Paris-Saclay, Oct. 2018. URL: `https://tel.archives-ouvertes.fr/tel-02459260` (Cited on pages 33, 39, 42, 44, 46, 90)

[131] ATLAS Collaboration. “Reconstruction of primary vertices at the ATLAS experiment in Run 1 proton–proton collisions at the LHC.” *Eur. Phys. J. C* 77 (2017), p. 332. DOI: `10.1140/epjc/s10052-017-4887-5`. arXiv: `1611.10235 [hep-ex]` (Cited on page 34)

[132] ATLAS Collaboration. *Electron and photon reconstruction and performance in ATLAS using a dynamical, topological cell clustering-based approach*. ATL-PHYS-PUB-2017-022. 2017. URL: `https://cds.cern.ch/record/2298955` (Cited on page 34)

[133] ATLAS Collaboration. *Jet Calibration and Systematic Uncertainties for Jets Reconstructed in the ATLAS Detector at* $\sqrt{s} = 13$ *TeV*. ATL-PHYS-PUB-2015-015. 2015. URL: `https://cds.cern.ch/record/2037613` (Cited on page 34)

[134] ATLAS Collaboration. “Electron efficiency measurements with the ATLAS detector using 2012 LHC proton–proton collision data.” *Eur. Phys. J. C* 77 (2017), p. 195. DOI: `10.1140/epjc/s10052-017-4756-2`. arXiv: `1612.01456 [hep-ex]` (Cited on page 34)

[135] Yanhui Ma. “Observation of H→bb decays and VH production with the ATLAS detector.” Theses. Université Paris-Saclay ; Shandong University (Jinan, Chine), May 2019. URL: `https://tel.archives-ouvertes.fr/tel-02157898` (Cited on pages 34, 35, 38, 42, 45, 47)

[136] ATLAS Collaboration. “Measurement of the muon reconstruction performance of the ATLAS detector using 2011 and 2012 LHC proton–proton collision data.” *Eur. Phys. J. C* 74 (2014), p. 3130. DOI: `10.1140/epjc/s10052-014-3130-x`. arXiv: `1407.3935 [hep-ex]` (Cited on page 34)

[137] ATLAS Collaboration. “Muon reconstruction performance of the ATLAS detector in proton–proton collision data at $\sqrt{s} = 13\,\mathrm{TeV}$.” *Eur. Phys. J. C* 76 (2016), p. 292. DOI: `10.1140/epjc/s10052-016-4120-y`. arXiv: `1603.05598 [hep-ex]` (Cited on pages 34, 35, 50)

[138] ATLAS Collaboration. “Reconstruction of hadronic decay products of tau leptons with the ATLAS experiment.” *Eur. Phys. J. C* 76 (2016), p. 295. DOI: `10.1140/epjc/s10052-016-4110-0`. arXiv: `1512.05955 [hep-ex]` (Cited on page 35)

[139] ATLAS Collaboration. *Measurement of the tau lepton reconstruction and identification performance in the ATLAS experiment using pp collisions at $\sqrt{s} = 13$ TeV.* ATLAS-CONF-2017-029. 2017. URL: `https://cds.cern.ch/record/2261772` (Cited on page 35)

[140] Walter Lampl et al. *Calorimeter Clustering Algorithms: Description and Performance.* ATL-LARG-PUB-2008-002. 2008. URL: `https://cds.cern.ch/record/1099735` (Cited on page 35)

[141] ATLAS Collaboration. “Jet energy measurement and its systematic uncertainty in proton–proton collisions at $\sqrt{s} = 7\,\mathrm{TeV}$ with the ATLAS detector.” *Eur. Phys. J. C* 75 (2015), p. 17. DOI: `10.1140/epjc/s10052-014-3190-y`. arXiv: `1406.0076 [hep-ex]` (Cited on page 35)

[142] ATLAS Collaboration. “Jet energy scale measurements and their systematic uncertainties in proton–proton collisions at $\sqrt{s} = 13\,\mathrm{TeV}$ with the ATLAS detector.” *Phys. Rev. D* 96 (2017), p. 072002. DOI: `10.1103/PhysRevD.96.072002`. arXiv: `1703.09665 [hep-ex]` (Cited on pages 35, 36, 50)

[143] ATLAS Collaboration. “Performance of pile-up mitigation techniques for jets in pp collisions at $\sqrt{s} = 8\,\mathrm{TeV}$ using the ATLAS detector.” *Eur. Phys. J. C* 76 (2016), p. 581. DOI: `10.1140/epjc/s10052-016-4395-z`. arXiv: `1510.03823 [hep-ex]` (Cited on page 35)

[144] ATLAS Collaboration. *Selection of jets produced in* 13 *TeV proton–proton collisions with the ATLAS detector.* ATLAS-CONF-2015-029. 2015. URL: `https://cds.cern.ch/record/2037702` (Cited on page 35)

[145] ATLAS Collaboration. *Optimisation and performance studies of the ATLAS b-tagging algorithms for the 2017-18 LHC run.* ATL-PHYS-PUB-2017-013. 2017. URL: `https://cds.cern.ch/record/2273281` (Cited on page 35)

[146] ATLAS Collaboration. “ATLAS b-jet identification performance and efficiency measurement with $t\bar{t}$ events in pp collisions at $\sqrt{s} = 13\,\mathrm{TeV}$” (2019). arXiv: `1907.05120 [hep-ex]` (Cited on page 35)

[147] ATLAS Collaboration. *Calibration of light-flavour b-jet mistagging rates using ATLAS proton–proton collision data at $\sqrt{s} = 13$ TeV.* ATLAS-CONF-2018-006. 2018. URL: `https://cds.cern.ch/record/2314418` (Cited on pages 35, 49)

[148] ATLAS Collaboration. *ATLAS Insertable B-Layer Technical Design Report.* ATLAS-TDR-19. 2010. URL: `https://cds.cern.ch/record/1291633` (Cited on page 35). Addendum: ATLAS-TDR-19-ADD-1. 2012. URL: `https://cds.cern.ch/record/1451888`

[149] ATLAS Collaboration. *Optimisation of the ATLAS b-tagging performance for the 2016 LHC Run.* ATL-PHYS-PUB-2016-012. 2016. URL: `https://cds.cern.ch/record/2160731` (Cited on page 35)

[150] A. D. Bukin. “Fitting function for asymmetric peaks” (2007). arXiv: `0711.4449 [physics.data-an]` (Cited on page 37)

[151] ATLAS Collaboration. “Performance of missing transverse momentum reconstruction with the ATLAS detector using proton–proton collisions at $\sqrt{s} = 13\,\mathrm{TeV}$.” *Eur. Phys. J. C* 78 (2018), p. 903. DOI: `10.1140/epjc/s10052-018-6288-9`. arXiv: `1802.08168 [hep-ex]` (Cited on pages 37, 50)

[152] David Delgove. “Measurement of the Higgs boson properties with ATLAS experiment at the LHC.” Theses. Université Paris-Saclay, Oct. 2016. URL: `https://tel.archives-ouvertes.fr/tel-01494070` (Cited on pages 39, 45, 46)

[153] Tasneem Saleem. “Development of pixel detector for ATLAS Inner Tracker(ITK) upgrade at HL-LHC and Searching for the Standard Model Higgs boson decay into b-quark pair with ATLAS experiment.” Theses. Université Paris-Saclay, Jan. 2019. URL: `https://tel.archives-ouvertes.fr/tel-02275808` (Cited on pages 43, 47)

[154] Andreas Hoecker et al. *TMVA - Toolkit for Multivariate Data Analysis.* 2007. arXiv: `physics/0703039 [physics.data-an]` (Cited on page 44)

[155] ATLAS Collaboration. “Measurements of b-jet tagging efficiency with the ATLAS detector using $t\bar{t}$ events at $\sqrt{s} = 13$ TeV.” *JHEP* 08 (2018), p. 089. DOI: `10.1007/JHEP08(2018)089`. arXiv: `1805.01845 [hep-ex]` (Cited on page 49)

[156] ATLAS Collaboration. *Measurement of b-tagging efficiency of c-jets in $t\bar{t}$ events using a likelihood approach with the ATLAS detector.* ATLAS-CONF-2018-001. 2018. URL: `https://cds.cern.ch/record/2306649` (Cited on page 49)

[157] ATLAS Collaboration. “Jet energy resolution in proton–proton collisions at $\sqrt{s} = 7$ TeV recorded in 2010 with the ATLAS detector.” *Eur. Phys. J. C* 73 (2013), p. 2306. DOI: `10.1140/epjc/s10052-013-2306-0`. arXiv: `1210.6210 [hep-ex]` (Cited on page 50)

[158] ATLAS Collaboration. *Electron efficiency measurements with the ATLAS detector using the 2015 LHC proton–proton collision data.* ATLAS-CONF-2016-024. 2016. URL: `https://cds.cern.ch/record/2157687` (Cited on page 50)

[159] ATLAS Collaboration. “Luminosity determination in pp collisions at $\sqrt{s} = 8$ TeV using the ATLAS detector at the LHC.” *Eur. Phys. J. C* 76.12 (2016), p. 653. DOI: `10.1140/epjc/s10052-016-4466-1`. arXiv: `1608.03953 [hep-ex]` (Cited on page 50)

[160] ATLAS Collaboration. “Measurement of the Inelastic Proton–Proton Cross Section at $\sqrt{s} = 13$ TeV with the ATLAS Detector at the LHC.” *Phys. Rev. Lett.* 117 (2016), p. 182002. DOI: `10.1103/PhysRevLett.117.182002`. arXiv: `1606.02625 [hep-ex]` (Cited on page 50)

[161] Andy Buckley, Jonathan Butterworth, Leif Lonnblad, David Grellscheid, Hendrik Hoeth, James Monk, Holger Schulz, and Frank Siegert. “Rivet user manual.” *Comput. Phys. Commun.* 184 (2013), pp. 2803–2819. DOI: `10.1016/j.cpc.2013.05.021`. arXiv: `1003.0694 [hep-ph]` (Cited on page 50)

[162] J. Alwall, R. Frederix, S. Frixione, V. Hirschi, F. Maltoni, et al. “The automated computation of tree-level and next-to-leading order differential cross sections, and their matching to parton shower simulations.” *JHEP* 07 (2014), p. 079. DOI: `10.1007/JHEP07(2014)079`. arXiv: `1405.0301 [hep-ph]` (Cited on page 51)

[163] M. Bahr et al. “Herwig++ Physics and Manual.” *Eur. Phys. J. C* 58 (2008), p. 639. DOI: `10.1140/epjc/s10052-008-0798-9`. arXiv: `0803.0883 [hep-ph]` (Cited on page 52)

[164] Johannes Bellm et al. “Herwig 7.0/Herwig++ 3.0 release note.” *Eur. Phys. J. C* 76.4 (2016), p. 196. DOI: `10.1140/epjc/s10052-016-4018-8`. arXiv: `1512.01178 [hep-ph]` (Cited on page 52)

[165] Stefano Frixione, Eric Laenen, Patrick Motylinski, Bryan R. Webber, and Chris D. White. “Single-top hadroproduction in association with a W boson.” *JHEP* 07 (2008), p. 029. DOI: `10.1088/1126-6708/2008/07/029`. arXiv: `0805.3067 [hep-ph]` (Cited on page 53)

[166] Kyle Cranmer, George Lewis, Lorenzo Moneta, Akira Shibata, and Wouter Verkerke. “HistFactory: A tool for creating statistical models for use with RooFit and RooStats” (June 2012) (Cited on page 56)

[167] Lorenzo Moneta et al. *The RooStats Project.* 2010. arXiv: `1009.1003 [physics.data-an]` (Cited on page 56)

[168] Roger J. Barlow and Christine Beeston. "Fitting using finite Monte Carlo samples." *Comput. Phys. Commun.* 77 (1993), pp. 219–228. DOI: `10.1016/0010-4655(93)90005-W` (Cited on page 57)

[169] Glen Cowan, Kyle Cranmer, Eilam Gross, and Ofer Vitells. "Asymptotic formulae for likelihood-based tests of new physics." *Eur. Phys. J. C* 71 (2011), p. 1554. DOI: `10.1140/epjc/s10052-011-1554-0`. arXiv: `1007.1727 [physics.data-an]` (Cited on pages 57, 58). Erratum: *Eur. Phys. J. C* 73 (2013), p. 2501. DOI: `10.1140/epjc/s10052-013-2501-z`

[170] A Wald. "Tests of Statistical Hypotheses Concerning Several Parameters When the Number of Observations is Large." *Transactions of the American Mathematical Society* Vol. 54.3 (1943), pp. 426–482. DOI: `10.1090/S0002-9947-1943-0012401-3` (Cited on page 59)

[171] Glen Cowan. "Statistical Models with Uncertain Error Parameters." *Eur. Phys. J. C* 79.2 (2019), p. 133. DOI: `10.1140/epjc/s10052-019-6644-4`. arXiv: `1809.05778 [physics.data-an]` (Cited on page 60)

[172] B. Efron. "Bootstrap Methods: Another Look at the Jackknife." *Ann. Statist.* 7.1 (Jan. 1979), pp. 1–26. DOI: `10.1214/aos/1176344552`. URL: `https://doi.org/10.1214/aos/1176344552` (Cited on page 60)

[173] B. Efron and R.J. Tibshirani. *An Introduction to the Bootstrap.* Chapman & Hall/CRC Monographs on Statistics & Applied Probability. Taylor & Francis, 1994. ISBN: 9780412042317. URL: `https://books.google.fr/books?id=gLlpIUxRntoC` (Cited on page 60)

[174] Daniel Buscher. "Search for Higgs bosons with b-jets in the final state in proton-proton collisions with the ATLAS experiment." Presented 26 Oct 2016. PhD thesis. Nov. 2016. URL: `https://cds.cern.ch/record/2232472` (Cited on page 61)

[175] S. S. Wilks. "The Large-Sample Distribution of the Likelihood Ratio for Testing Composite Hypotheses." *Annals Math. Statist.* 9.1 (1938), pp. 60–62. DOI: `10.1214/aoms/1177732360` (Cited on page 72)

[176] ATLAS Collaboration. *Measurement of Higgs boson properties in the diphoton decay channel using* 80 fb^{-1} *of* pp *collision data at* $\sqrt{s} = 13$ *TeV with the ATLAS detector.* ATLAS-CONF-2018-028. 2018. URL: `https://cds.cern.ch/record/2628771` (Cited on page 77)

[177] ATLAS Collaboration. *Measurements of the Higgs boson production, fiducial and differential cross sections in the* 4ℓ *decay channel at* $\sqrt{s} = 13$ *TeV with the ATLAS detector.* ATLAS-CONF-2018-018. 2018. URL: `https://cds.cern.ch/record/2621479` (Cited on page 77)

[178] ATLAS Collaboration. "Measurements of Higgs boson properties in the diphoton decay channel with $36\,\text{fb}^{-1}$ of pp collision data at $\sqrt{s} = 13\,\text{TeV}$ with the ATLAS detector." *Phys. Rev. D* 98 (2018), p. 052005. DOI: `10.1103/PhysRevD.98.052005`. arXiv: `1802.04146 [hep-ex]` (Cited on pages 77, 86)

[179] ATLAS Collaboration. "Measurement of the Higgs boson coupling properties in the $H \to ZZ^* \to 4\ell$ decay channel at $\sqrt{s} = 13\,\text{TeV}$ with the ATLAS detector." *JHEP* 03 (2018), p. 095. DOI: `10.1007/JHEP03(2018)095`. arXiv: `1712.02304 [hep-ex]` (Cited on page 77)

[180] Andreas Helset, Adam Martin, and Michael Trott. "The Geometric Standard Model Effective Field Theory." *JHEP* 03 (2020), p. 163. DOI: `10.1007/JHEP03(2020)163`. arXiv: `2001.01453 [hep-ph]` (Cited on page 86)

[181] Tancredi Carli. "High-lights of the ATLAS and ALICE experiments." *PoS* ICHEP2018 (2019), p. 693. DOI: `10.22323/1.340.0693` (Cited on page 90)

[182] ATLAS Collaboration. “Measurement of the associated production of a Higgs boson decaying into b-quarks with a vector boson at high transverse momentum in pp collisions at $\sqrt{s} = 13$ TeV with the ATLAS detector.” *Phys. Lett. B* 816 (2021), p. 136204. DOI: `10.1016/j.physletb.2021.136204`. arXiv: `2008.02508 [hep-ex]` (Cited on page 91)

[183] A. Glazov. “Averaging of DIS Cross Section Data.” *AIP Conference Proceedings* 792 (2005), pp. 237–240. DOI: `10.1063/1.2122026` (Cited on page 111)

Remerciements

Voici donc le moment tant attendu des remerciements. Attendu au moins par l'auteur, puisque leur rédaction marque l'achèvement de ce document. Même si cette section est quelque peu cachée entre la bibliographie et les appendices, je ne doute pas que ce sera la page de cette HDR qui aura le plus de lecteurs, alors je vais essayer de n'oublier personne !

Je tiens tout d'abord à remercier chaleureusement, pour avoir accepté d'être rapporteurs de mon habilitation, Gustaaf Brooijmans, Pierre Savard et Isabelle Wingerter (9 ans après sa participation à mon jury de thèse !). Un grand merci également aux autres membres de mon jury : Gautier Hamel de Monchenault, Marie-Hélène Schune et Laurent Vacavant.

L'ensemble du travail présenté dans ce manuscrit est comme toujours en physique des particules une œuvre éminemment collective. En particulier, l'intense productivité de ces sept ans passés sur le sujet depuis mon arrivée au LAL doit beaucoup à l'ensemble des collègues du laboratoire qui ont gravité autour de l'analyse $VH, H \to b\bar{b}$. Merci donc à Jean-Baptiste, Marumi et Luc pour leurs échanges sur le sujet. J'ai une immense gratitude envers Jean-François : j'ai énormément appris à travers ta connaissance encyclopédique de la physique au LHC et des analyses, et ta capacité à passer en revue des catalogues de plots pour en tirer les points intéressants ou suspicieux. Un grand merci à Camilla pour la bonne humeur permanente que tu as apportée dans l'année que tu as passé au LAL avant de te tourner vers la communication scientifique, et à Arthur pour le travail sans relâche que tu as mené en vue de l'observation, en toute discrétion et modestie. Les résultats présentés dans ce document ne pourraient pas voir le jour sans le travail quotidien des doctorants impliqués sur le sujet. Ça a été un véritable plaisir de travailler avec David, Charles, Yanhui et Tasneem. Merci enfin à Konie qui a accepté de s'engager sur un sujet de thèse sous ma direction propre, et qui a toujours maintenu sa bonne humeur même dans les périodes de forte pression.

Nous avons étroitement collaboré au début du Run-2 avec nos collègues du LPNHE. Un très grand merci à Paolo pour son enthousiasme indéfectible et les discussions de physique toujours fructueuses. Merci également à Carlo, Changqiao, Louis et Ilaria pour la bonne ambiance dans laquelle cette collaboration s'est déroulée.

Au-delà de nos collègues franciliens, le travail présenté dans cette habilitation est le résultat de la collaboration entre tous les physiciens du groupe Hbb d'ATLAS. Qu'ils soient tous remerciés ici, et en particulier Gabriel, Tim, Yuji, Andy M., Valerio et Hannah. Cela a été un privilège de travailler dans un groupe capable de toujours tendre vers un but commun, où les désaccords se résolvent par des discussions et arguments scientifiques afin d'obtenir un consensus, et où toutes les nouvelles idées peuvent être discutées. Cette ambiance de travail apporte beaucoup d'émulation, et a largement contribué à la capacité du groupe de publier rapidement, plusieurs années de suite, des résultats sur une analyse pourtant complexe.

L'équipe ATLAS d'IJCLab ne se limite pas à la recherche sur VH, $H \to b\bar{b}$, loin de là. Je tiens à remercier l'ensemble de mes collègues, car c'est un vrai plaisir de travailler dans cette équipe. Je me suis découvert depuis quelques années un goût certain pour le travail sur nos chers (au sens propre comme au sens figuré) détecteurs, et en particulier pour l'électronique du calorimètre. Un immense merci à Laurent S. pour m'avoir entraîné dans cette voie, pour les innombrables conseils et discussions sur le sujet, et pour l'accès à la machine à café ! Le travail d'upgrade des préamplificateurs du calorimètre doit également beaucoup à Laurent D. et R.D. : merci ! Merci enfin à Daniel : mon activité sur un futur calorimètre pour FCC-ee n'irait pas bien loin sans tes 35 ans d'expertise sur les calorimètres à liquides nobles.

Le travail sur les détecteurs serait bien vain sans tous ceux qui font l'essentiel du « vrai » boulot. Je tiens à remercier chaleureusement toute l'équipe d'Omega pour votre accueil et pour le travail intense sur le projet LAUROC : Christophe, Nathalie, Selma, Sylvie (j'attends encore votre contribution pour le papier LAUROC !), Gisèle, sans oublier Pierrick. Merci à Aboud pour la mécanique du robot pour les tests séries des chips. Merci également à Ronic pour ton investissement dans le projet de calorimètre pour FCC.

Enfin, je souhaite exprimer toute ma sympathie pour l'ensemble des personnels administratifs du laboratoire, sans qui nos activités de recherche ne pourraient pas fonctionner.

Appendix A

Proofs of statistics results

A.1 Significance of pulls

It has been argued in section 2.6.1 that the post-fit value of a nuisance parameter with a Normal constraint term is not a measure in itself of the compatibility between the data and the constraint (which in frequentist terms is an auxiliary measurement of the parameter). Indeed, it is more likely for the post-fit value of the parameter to fluctuate around the value of the auxiliary measurement (which is conventionnally taken as 0) when the data is significantly sensitive to it than when the likelihood (constraint term excluded) shows very little dependence to this parameter. A consequence of the data having sensitivity to a parameter, is that the post-fit uncertainty in this parameter is constrained to a value lower than 1. Therefore, a quantification of the compatibility between the data and the auxiliary measurement is expected to depend at least on the post-fit value of the parameter (the farther from 0, the lower the compatibility) and on the post-fit uncertainty (the smaller the uncertainty, the larger the compatibility).

Starting from the expression of the likelihood function:

$$\mathscr{L}(\mu,\boldsymbol{\theta}) = \prod_{i\in\text{bins}} \text{Pois}\left(n_i|\mu s_i(\boldsymbol{\theta}) + b_i(\boldsymbol{\theta})\right) \prod_{\theta\in\boldsymbol{\theta}} \mathscr{C}(\theta), \tag{A.1}$$

a given nuisance parameter t with a Normal constraint can be explicitely taken out of the vector $\boldsymbol{\theta}$, and its constraint term can be singled out:

$$\begin{aligned}\mathscr{L}(\mu,\boldsymbol{\theta}) &= \left(\prod_{i\in\text{bins}} \text{Pois}\left(n_i|\mu, t,\boldsymbol{\theta}\right) \times \prod_{\theta\neq t} \mathscr{C}(\theta)\right) \times \mathscr{G}(t_0 = 0|t,\sigma_0 = 1) &\text{(A.2)}\\ &= \mathscr{L}_{\text{unc}}(\mu, t,\boldsymbol{\theta}) \times \mathscr{G}(t_0 = 0|t,\sigma_0 = 1). &\text{(A.3)}\end{aligned}$$

The last form makes it clear that the post-fit value that is taken by the parameter t is the result of the combination of the auxiliary measurement $\mathscr{G}(t_0 = 0|t,\sigma_0 = 1)$ with the measurement in data without the constraint, which is labelled as the unconstrained likelihood $\mathscr{L}_{\text{unc}}(\mu, t,\boldsymbol{\theta})$. The expression of the constraint as $\mathscr{G}(t_0 = 0|t,\sigma_0 = 1)$ makes it clear that t is a parameter of the gaussian probability density, along with the width σ_0, while the measurement is $t_0 = 0$. Assuming Wald's approximation holds for t around the maximum of the unconstrained likelihood, then this likelihood can be approximated by a gaussian distribution:

$$\mathscr{L}_{\text{unc}}(\mu, t, \boldsymbol{\theta}) \sim \mathscr{G}(\hat{t}_{\text{unc}}|t, \sigma_{\text{unc}}), \tag{A.4}$$

where $\hat{t}_{\text{unc}}$ is the value of t at the maximum of $\mathscr{L}_{\text{unc}}$. In that case, the combination of the auxiliary measurement with the unconstrained likelihood appears as a simple averaging of two gaussian measurements, and the post-fit value and uncertainty in t in the full likelihood are therefore:

$$\sigma_t^2 = \frac{1}{\frac{1}{\sigma_0^2} + \frac{1}{\sigma_{\text{unc}}^2}} \tag{A.5}$$

$$\hat{t} = \left(\frac{\hat{t}_{\text{unc}}}{\sigma_{\text{unc}}^2} + \frac{t_0}{\sigma_0^2}\right)\sigma_t^2. \tag{A.6}$$

An approximate quantification of the compatibility between the two measurements can then be achieved by comparing the value $\hat{t}_{\text{unc}} - t_0$ to the square root of its variance $\text{Var}(\hat{t}_{\text{unc}} - t_0)$, or equivalently by comparing $\hat{t} - t_0$ to the square root of its variance $\text{Var}(\hat{t} - t_0)$. It is worth emphasizing the importance of explicitely writing t_0 in these expressions, even though $t_0 = 0$. The fact that this value of 0 is always used is a conventionnal choice, that reflects that the likelihood has been calibrated to the value of the auxiliary measurement. If we were to do a pseudo-experiment, in which the n_i, t_0 and $\boldsymbol{\theta}_0$ would take new values, then we would use the fact that formally $\mathscr{G}(t_0|t, \sigma_0) = \mathscr{G}(0|t - t_0, \sigma_0)$ to define $t' = t - t_0$ and use it instead of t as the nuisance parameter, which corresponds to a re-calibration of the distributions of the s_i and b_i in the likelihood.

The calculation then easily concludes by using equation A.6:

$$\begin{aligned}
\text{Var}(\hat{t} - t_0) &= \text{Var}(\hat{t}) + \text{Var}(t_0) - 2\text{Cov}(\hat{t}, t_0) \\
&= \sigma_t^2 + 1 - 2\left(\frac{\sigma_t^2}{\sigma_{\text{unc}}^2}\text{Cov}(\hat{t}_{\text{unc}}, t_0) + \frac{\sigma_t^2}{\sigma_0^2}\text{Cov}(t_0, t_0)\right) \\
&= \sigma_t^2 + 1 - 2\left(0 + \sigma_t^2\right) \\
&= 1 - \sigma_t^2.
\end{aligned} \tag{A.7}$$

Therefore the compatibility of the auxiliary measurement with the data for the parameter t can be approximately quantified using the significance of the post-fit value of t, in number of standard deviations:

$$Z_t = \frac{\hat{t}}{\sqrt{1 - \sigma_t^2}}. \tag{A.8}$$

The accurateness of this evaluation has been checked using pseudo-experiments on a non-final version of the likelihood used in the $VH(b\bar{b})$ analysis. For the vast majority of nuisance parameters, Wald's approximation works well, and as a result eq. (A.8) is an accurate quantification of the likeliness of a pull. This equation can also apply to nuisance parameters related to the limited statistics in the simulated samples with a few simple modifications, at least when the number of simulated events is enough that the Poisson distribution can be approximated by a gaussian one. Deviations from a gaussian behaviour, sometimes significant, appear in several cases. They seem to occur for nuisance parameters associated to very large uncertainties, or to cases where the interpolation and extrapolation strategies of HistFactory discussed in section 2.6 do matter. Another cause of deviations from a gaussian distribution is the limited numerical precision in the likelihood maximisation, which can lead to issues for nuisance parameters with $\sigma_t^2 \sim 1$. In practice, the nuisance parameters mostly concerned by these numerical flucutations are the ones on energy scales and resolutions, that as discussed in section 2.6.1 need dedicated treatment due to the statistical uncertainties in their evaluation.

The abovementioned caveats somewhat limit the usefulness of the quantity Z_t: if all nuisance parameters had a gaussian behaviour, the distribution of Z_t built from the post-fit values of all nuisance parameters would be expected to be Normal, and a deviation from the normal distribution in the fit to data would be an indication of bad fit quality (a feature known from combination codes working only with gaussian uncertainties such as [183]). In practice, the few nuisance parameters with non-gaussian behaviour are enough to always create tails in the distribution of Z_t. Consequently the computation of Z_t for nuisance parameters is preferably used as a qualitative tool only, where nuisance parameters with a large significance of their post-fit value are brought to attention and further investigated.

A.2 Properties of the methods used to quantify the impact of systematic uncertainties

In section 2.6.2 the influence of the systematic uncertainties in the measurement of the signal strength of the multivariate analysis has been performed using two alternative methods: one is appropriate to quantify the impact of single nuisance parameters, the other one is used to assess the impact of groups of systematic uncertainties. The first method consists in evaluated the change in the fitted signal strength when profiling the likelihood at values corresponding to the parameter' $+1\sigma$ and -1σ post-fit values. The second method defines the uncertainty of a group of nuisance parameters as the difference in quadrature between the total uncertainty in the signal strength when the are profiled and this same total uncertainty when they are fixed to their best-fit values.

It has been argued that because of the correlations between nuisance parameters induced by the profile likelihood fit, there is no single unambiguous way to define the impact of a group of systematics. In this section the behaviour of the two methods is investigated in simplified cases and for single nuisance parameters, in order to compare their results between themselves and with what one expects a priori. The cases of systematic uncertainties affecting the signal expectation and those affecting the backgroudn expectation differ significantly and are therefore studied separately.

A.2.1 Systematic uncertainty in the background expectation

Simplified setup and naive expectation

As the goal is to study the impact of a nuisance parameter affecting only the background expectation, it is sufficient to setup a counting experiment, with a relative uncertainty δ in the background. The expected number of events is:

$$\nu(\mu,\theta) = \mu s + b(1+\delta\theta),$$

where s and b are the nominal expected signal and background yields, respectively, μ is the signal strength, and θ is the nuisance parameter related to the uncertainty in question. Naively, a 1σ-change in the background yield $b\delta$ has to be compensated by a change in μ of $b\delta/s$, thus the expected impact of the nuisance parameter is $b\delta/s$.

In the gaussian regime, the profile likelihood function can be replaced by a simpler χ^2 model that makes analytic calculations possible:

$$\chi^2(\mu,\theta) = \frac{\big(n-\nu(\mu,\theta)\big)^2}{\sigma_s^2} + \theta^2, \tag{A.9}$$

where σ_s represents the uncertainty in the number of signal events (μs) in the absence of any background uncertainty. The expected impact of the nuisance parameter is computed in the Asimov dataset, for which $n = s + b$. In this case $\hat{\mu} = 1$ and $\hat{\theta} = 0$.

Impact on the signal strength through profiling

The first step is to compute the post-fit uncertainty in θ. In this simple model the signal strength can always compensate any change in the nuisance parameter, i.e the term $n - \nu(\mu,\theta)$ can always be 0 for any value of θ. Therefore θ is not constrained at all by the fit, and $\sigma_\theta = 1$.

The profiled likelihood values of the signal strength $\hat{\hat{\mu}}(\theta = \pm 1)$ for $\theta = \pm 1$ are then found by solving for:

$$\frac{\partial \chi^2}{\partial \mu}(\mu, \theta = \pm 1) = 0,$$

and the impact of the systematic uncertainty is finally:

$$\Delta\mu_{\pm 1} = 1 - \hat{\hat{\mu}}(\theta = \pm 1) = \pm\frac{b\delta}{s}. \tag{A.10}$$

The result matches the naive expectation.

Impact on the signal strength through subtraction in quadrature

The total positive (resp. negative) uncertainty in μ is defined as the difference between $\hat{\mu}$ and the value larger than (resp. lower than) $\hat{\mu}$ for which the profiled χ^2 value is 1. The first step is therefore to compute the profiled value of the nuisance parameter $\hat{\hat{\theta}}(\mu)$, by solving for

$$\frac{\partial \chi^2}{\partial \theta}(\mu, \theta) = 0.$$

This leads to:

$$\hat{\hat{\theta}}(\mu) = \frac{\delta s b(1-\mu)}{\sigma_s^2 + (b\delta)^2}.$$

The total uncertainty in μ is finally found by computing $\mu^{\text{tot}}_{\pm 1}$ so that $\chi^2\left(\mu^{\text{tot}}_{\pm 1}, \hat{\hat{\theta}}(\mu^{\text{tot}}_{\pm 1})\right) = 1$:

$$1 - \mu^{\text{tot}}_{\pm 1} = \pm\frac{\sqrt{\sigma_s^2 + (b\delta)^2}}{s}. \tag{A.11}$$

The total uncertainty in μ when the nuisance parameter θ is fixed to its post-fit value 0 is by construction $\pm\sigma_s/s$.

The difference in quadrature between the two uncertainties is therefore:

$$\Delta\mu_{\pm 1} = \sqrt{\pm\frac{\sigma_s^2 + (b\delta)^2}{s^2} \mp \frac{\sigma_s^2}{s^2}} = \pm\frac{b\delta}{s}. \tag{A.12}$$

For uncertainties affecting the background estimation, both methods to evaluate the impact of systematic uncertainties thus yield the same result (equations A.10 and A.12), that furthermore matches the natural expectation.

A.2.2 Systematic uncertainty in the signal expectation

Simplified setup and naive expectation

In the case of a systematic uncertainty affecting the signal yield, the setup can be simplified further, and the impact of the background in the measurement can be absorbed in the definition of the total uncertainty in the number of signal events (before the addition of the signal systematic uncertainty):

$$\chi^2(\mu) = \frac{(n-\mu s)^2}{\sigma_s^2}.$$

When adding a relative uncertainty δ in the signal yield with a corresponding nuisance parameter, this becomes:

$$\chi^2(\mu,\theta) = \frac{\big(n-\mu s(1+\delta\theta)\big)^2}{\sigma_s^2} + \theta^2. \tag{A.13}$$

The Asimov dataset corresponds to $n = s$, and therefore $\hat{\mu} = 1$ and $\hat{\theta} = 0$.

In this case, the naive expectation is that the impact of the systematic uncertainty on the signal strength is simply δ.

Impact on the signal strength through profiling

Similarly to the case of a systematic uncertainty in the background yield, the signal strength can compensate for any change in the signal yield from the systematic uncertainty, so that the nuisance parameter θ is not constrained post-fit. The profiled values $\hat{\hat{\mu}}(\theta = \pm 1)$ are then easily found, and yield:

$$\Delta\mu_{\pm 1} = 1 - \hat{\hat{\mu}}(\theta = \pm 1) = \frac{\pm\delta}{1\pm\delta}. \tag{A.14}$$

This result is a bit different from the naive expectation and shows some asymmetry between the positive and negative impacts, with a correction of the order δ^2. This is easily explained as the result of setting θ to ±1 changing the number of signal events by a given number, which has to be compensated by the multiplicative parameter μ. The average of the up and down variations is:

$$\Delta\mu_{\text{avg}} = \frac{\delta}{1-\delta^2}. \tag{A.15}$$

Impact on the signal strength through subtraction in quadrature

As in the case of the systematic uncertainty in the background yield, the total uncertainty in μ when the nuisance parameter is fixed to its post-fit value of 0 is by construction $\pm\sigma_s/s$. The total uncertainty in the presence of the nuisance parameter requires the calculation of the profiled value $\hat{\hat{\theta}}(\mu)$:

$$\hat{\hat{\theta}}(\mu) = \frac{\delta\mu(1-\mu)}{\sigma_s^2/s^2 + (\delta\mu)^2}.$$

The resulting profiled χ^2 is displayed on fig. A.1 using example values of $\delta = 0.2$ and $\sigma_s/s = 0.5$. It can be observed that the addition of a (symmetric) relative uncertainty δ on the expected signal yield, on top of the symmetric uncertainty σ_s, yields a very asymmetric χ^2 profile. This can be understood by noticing that the first term in the χ^2 of eq. (A.13) increases according to a difference in *numbers of events*, while it can be dampened by pulling θ, that changes the number of events by a given *fraction*. Therefore pulling θ is more efficient at reducing the χ^2 when $\mu \sim 1 + \sigma_s/s$ than when $\mu \sim 1 - \sigma_s/s$. Solving for the total uncertainty in μ then gives:

$$1 - \mu_{\pm 1}^{\mathrm{tot}} = \frac{-\delta^2 \mp \sqrt{(\sigma_s/s)^2 + \delta^2 - (\delta\sigma_s/s)^2}}{1 - \delta^2}. \tag{A.16}$$

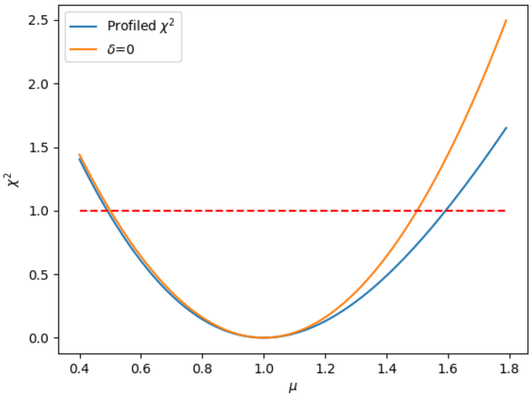

Figure A.1: Distribution of the profiled χ^2 in the absence of any systematic uncertainty (orange) and with the uncertainty added (blue), for a relative systematic uncertainty $\delta = 0.2$ and a total uncertainty without it $\sigma_s/s = 0.5$.

As the impact of the uncertainty is defined as the difference in quadrature between the two curves displayed on fig. A.1, it exhibits a very strong asymmetry:

$$\Delta\mu_{\pm 1} = \sqrt{(1 - \mu_{\pm 1}^{\mathrm{tot}})^2 - (\sigma_s/s)^2} = \delta\mu_{\pm 1}^{\mathrm{tot}}. \tag{A.17}$$

The impact therefore appears as the evaluation of the uncertainty δ at the $\pm 1\sigma$ positions of μ. The asymmetry is thus stronger both for larger values of σ_s/s and for larger values of δ. Although the asymmetry is real and is explained by the reasons discussed above, it can be seen as a mere artifact of the method used to estimate the impact of this systematic uncertainty. It conveys a somewhat misleading message on the real effect of the uncertainty, since the original signal uncertainty δ introduced in the χ^2 is fully symmetric. Fortunately, the average of the up and down effects is:

$$\Delta\mu_{\mathrm{avg}} = \frac{\delta}{1 - \delta^2}. \tag{A.18}$$

This value is equal to the one computed from the profiling method in eq. (A.15), and very close to the naive expectation δ. It seems therefore more appropriate to report the average value of the up and down effects at least for signal uncertainties, when providing the breakdown of the systematic uncertainties as in table 2.10.

Although the calculations performed in this section are based on very simplified models, the resulting analytic formulas match quite accurately the results of the evaluations on complete likelihoods such as that of the *VH*$(b\bar{b})$ analysis.

Appendix B

Additional post-fit figures and tables

B.1 Results of the multivariate analysis

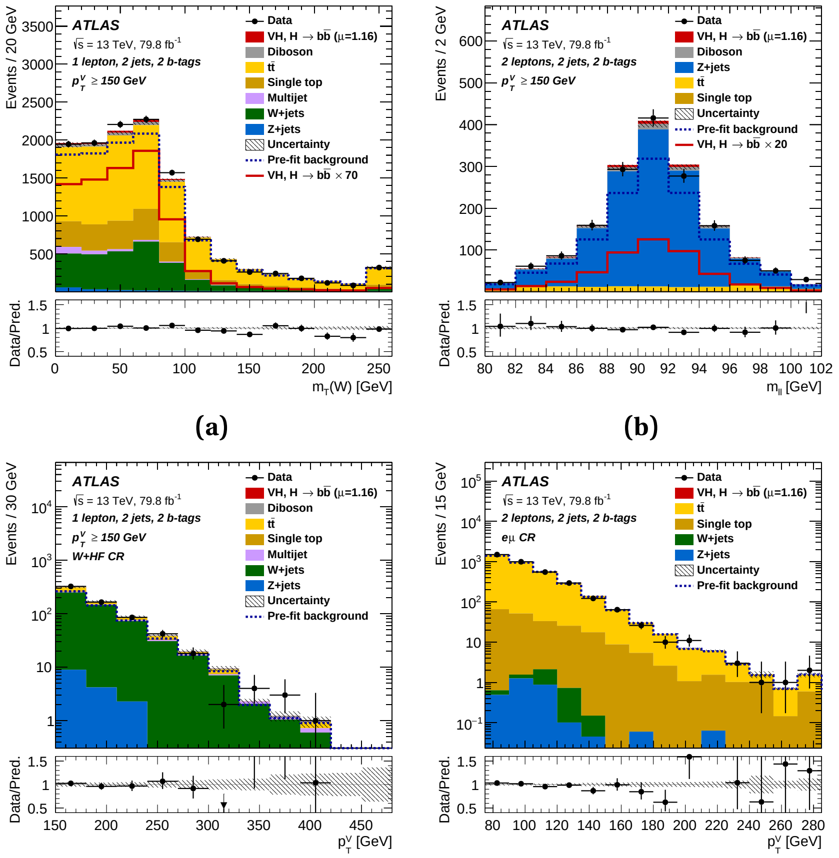

(a) **(b)**

(c) **(d)**

Figure B.1: The post-fit distributions for m_T^W in the 1-lepton channel (top left), $m_{\ell\ell}$ in the 2-lepton channel (top right), p_T^V in the W+hf control region (botton left) and p_T^V in the $e\mu$ control region (bottom right) for 2-jet, 2-b-tag events. The background contributions after the global likelihood fit are shown as filled histograms. The Higgs boson signal (m_H = 125 GeV) is shown as a filled histogram on top of the fitted backgrounds normalised to the signal yield extracted from data (μ = 1.16).

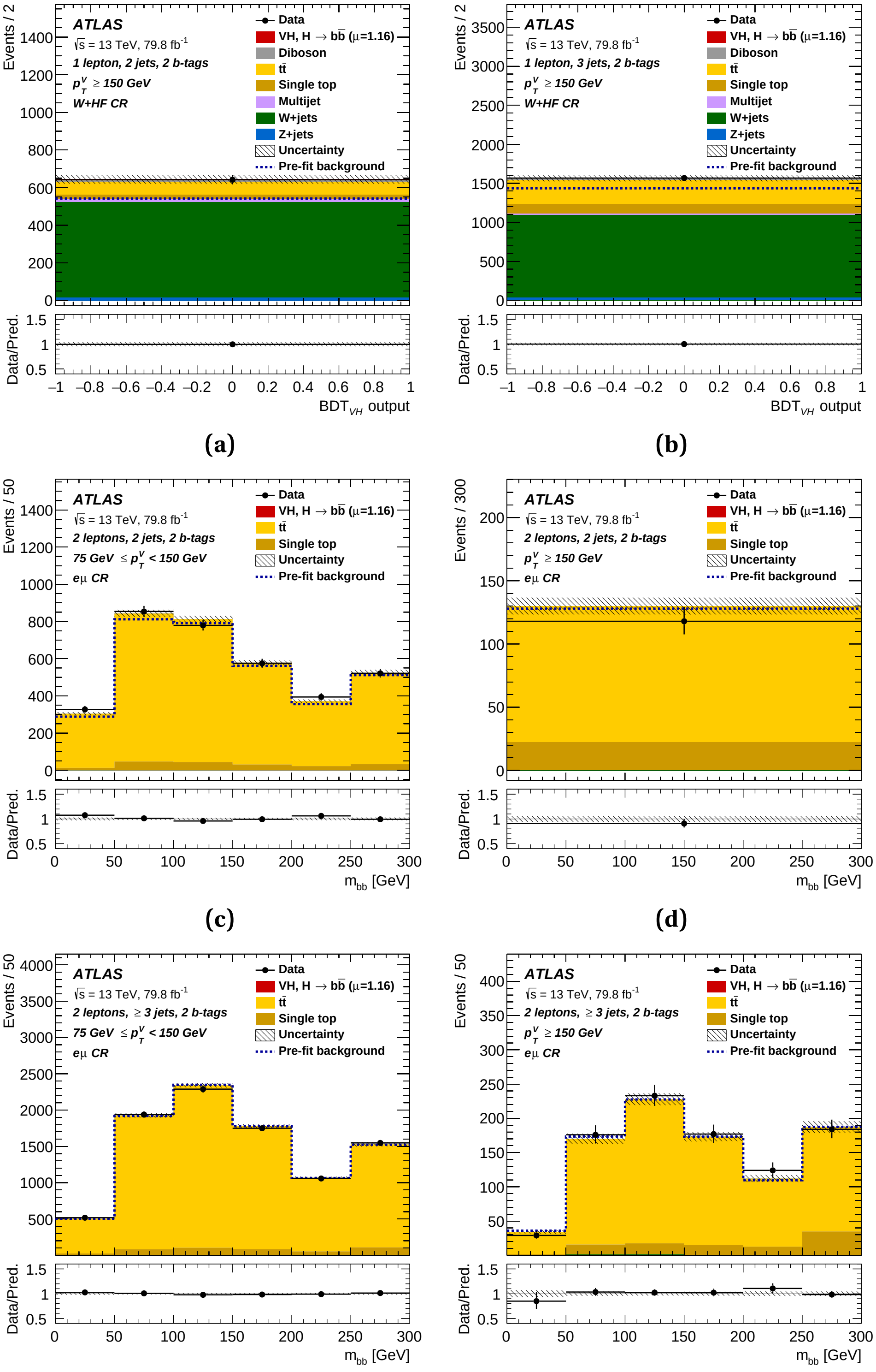

(a) (b)

(c) (d)

(e) (f)

Figure B.2: The post-fit distributions in the control regions of the analysis: yields in the $W+$hf control region (top), m_{bb} distribution or yield in the high-p_T^V $e\mu$ control region (middle) and m_{bb} distribution in the medium-p_T^V $e\mu$ control region (bottom), in the 2-jet (left) and 3-jet (right) categories. The background contributions after the global likelihood fit are shown as filled histograms. The Higgs boson signal (m_H = 125 GeV) is shown as a filled histogram on top of the fitted backgrounds normalised to the signal yield extracted from data (μ = 1.16), and unstacked as an unfilled histogram, scaled by the factor indicated in the legend. The dashed histogram shows the total pre-fit background. The size of the combined statistical and systematic uncertainty for the sum of the fitted signal and background is indicated by the hatched band. The ratio of the data to the sum of the fitted signal (μ = 1.16) and background is shown in the lower panel. The m_{bb} distributions are shown with the binning used in the global likelihood fit.

Table B.1: The fitted signal and background yields for each control region category in each channel ($W+$hf in the 1-lepton channel, $e\mu$ events in the 2-lepton channel), corresponding to the selection applied to the control regions for the multivariate analysis. The yields are normalised by the results of the global likelihood fit. All systematic uncertainties are included in the indicated uncertainties. An entry of "–" indicates that a specific background component is negligible in a certain region, or that no simulated events are left after the analysis selection.

	1-lepton		2-lepton			
	$p_\mathrm{T}^V > 150$ GeV, 2-b-tag		75 GeV $< p_\mathrm{T}^V <$ 150 GeV, 2-b-tag		$p_\mathrm{T}^V > 150$ GeV, 2-b-tag	
Process	2-jet	3-jet	2-jet	≥3-jet	2-jet	≥3-jet
$Z+$hf	15.1 ± 1.4	33 ± 2.5	2.5 ± 0.2	2.1 ± 0.2	< 1	< 1
$W+ll$	2.1 ± 1.5	3.8 ± 2.6	–	–	–	–
$W+cl$	8.4 ± 4.1	13.5 ± 6.6	–	< 1	–	–
$W+$hf	498 ± 34	1044 ± 92	2.5 ± 0.3	8.4 ± 1.0	< 1	3.3 ± 0.4
Single top quark	23.8 ± 5.4	122 ± 23	189 ± 90	450 ± 210	22.4 ± 7.1	93 ± 27
$t\bar{t}$	68 ± 18	307 ± 77	3243 ± 98	8690 ± 210	107.3 ± 6.7	807 ± 37
Diboson	13.4 ± 3.7	22.6 ± 7.5	–	< 1	–	< 1
Multi-jet e sub-ch.	8.3 ± 8.5	3.6 ± 2.9	–	–	–	–
Multi-jet μ sub-ch.	6.9 ± 4.6	13 ± 13	–	–	–	–
Total bkg.	644 ± 23	1563 ± 39	3437 ± 58	9153 ± 95	130.1 ± 6.7	905 ± 27
Signal (post-fit)	< 1	2.3 ± 0.6	< 1	< 1	< 1	< 1
Data	642	1567	3450	9102	118	923

B.2 Results of the dijet-mass analysis

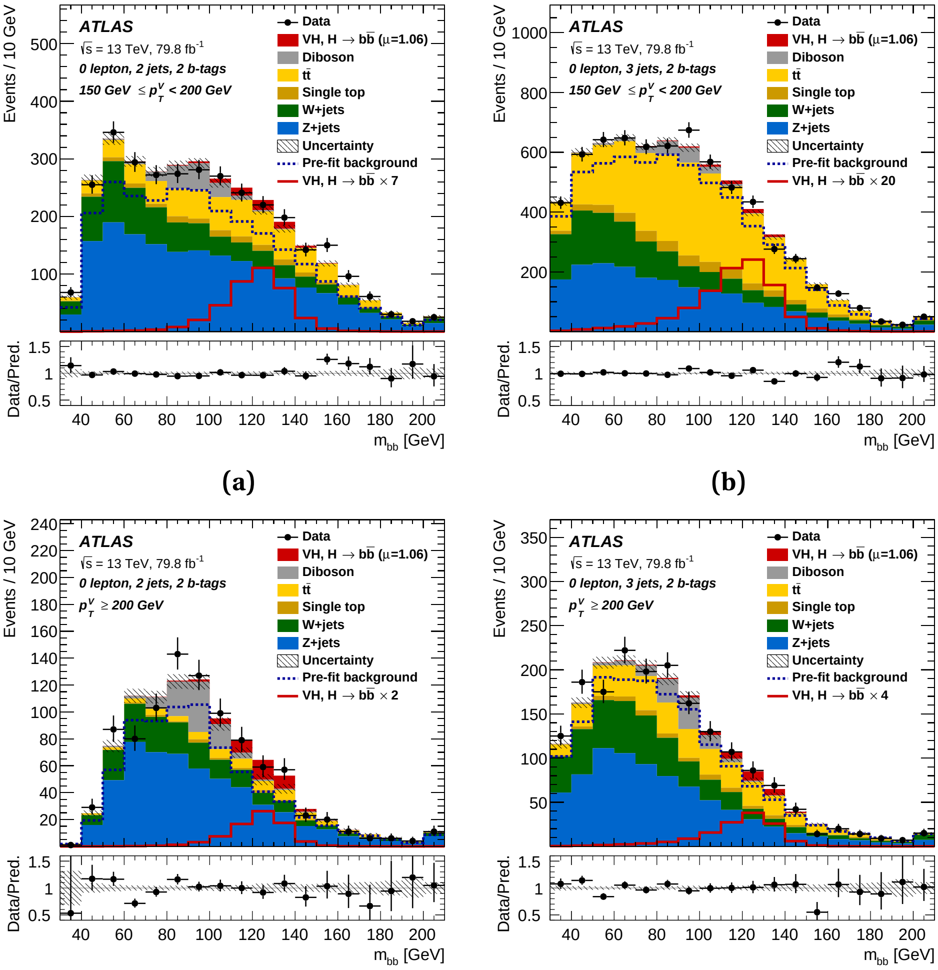

(a)

(b)

(c)

(d)

Figure B.3: Distributions of m_{bb} used as input to the global likelihood fit of the dijet-mass analysis. The distributions refer to the signal regions of the 0-lepton channel. Shown are the data (points with error bars) and expectation (histograms). The background contributions after the global likelihood fit are shown as filled histograms. The Higgs boson signal ($m_H = 125$ GeV) is shown as a filled histogram on top of the fitted backgrounds normalised to the signal yield extracted from data ($\mu = 1.06$), and unstacked as an unfilled histogram, scaled by the factor indicated in the legend. The dashed histogram shows the total pre-fit background. The entries in overflow are included in the last bin. The size of the combined statistical and systematic uncertainty for the sum of the signal and fitted background is indicated by the hatched band. The ratio of the data to the sum of the signal and fitted background is shown in the lower panel.

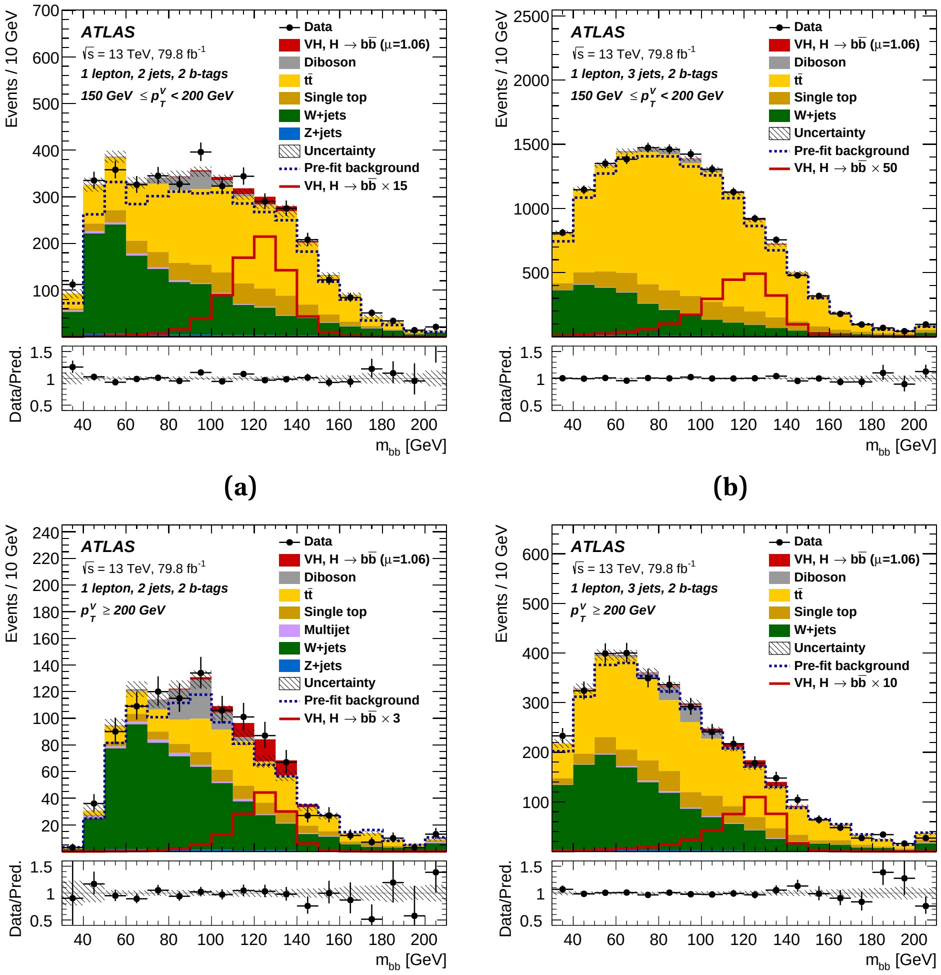

(a)

(b)

(c)

(d)

Figure B.4: Distributions of m_{bb} used as input to the global likelihood fit of the dijet-mass analysis. The distributions refer to the signal regions of the 1-lepton channel. Shown are the data (points with error bars) and expectation (histograms). The background contributions after the global likelihood fit are shown as filled histograms. The Higgs boson signal ($m_H = 125$ GeV) is shown as a filled histogram on top of the fitted backgrounds normalised to the signal yield extracted from data ($\mu = 1.06$), and unstacked as an unfilled histogram, scaled by the factor indicated in the legend. The dashed histogram shows the total pre-fit background. The entries in overflow are included in the last bin. The size of the combined statistical and systematic uncertainty for the sum of the signal and fitted background is indicated by the hatched band. The ratio of the data to the sum of the signal and fitted background is shown in the lower panel.

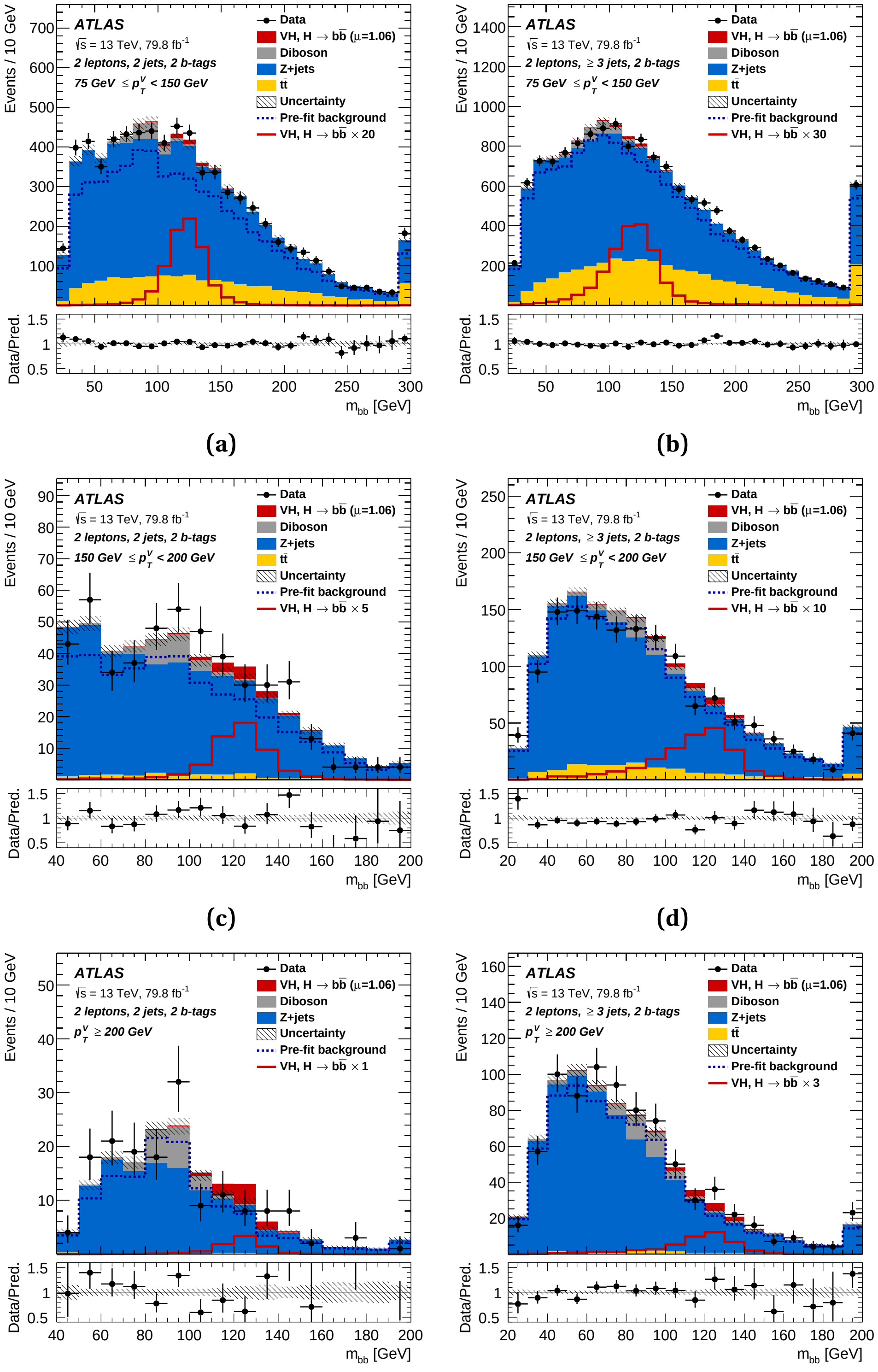

(a)

(b)

(c)

(d)

(e)

(f)

Figure B.5: Distributions of m_{bb} used as input to the global likelihood fit of the dijet-mass analysis. The distributions refer to the signal regions of the 2-lepton channel. Shown are the data (points with error bars) and expectation (histograms). The background contributions after the global likelihood fit are shown as filled histograms. The Higgs boson signal ($m_H = 125$ GeV) is shown as a filled histogram on top of the fitted backgrounds normalised to the signal yield extracted from data ($\mu = 1.06$), and unstacked as an unfilled histogram, scaled by the factor indicated in the legend. The dashed histogram shows the total pre-fit background. The entries in overflow are included in the last bin. The size of the combined statistical and systematic uncertainty for the sum of the signal and fitted background is indicated by the hatched band. The ratio of the data to the sum of the signal and fitted background is shown in the lower panel.

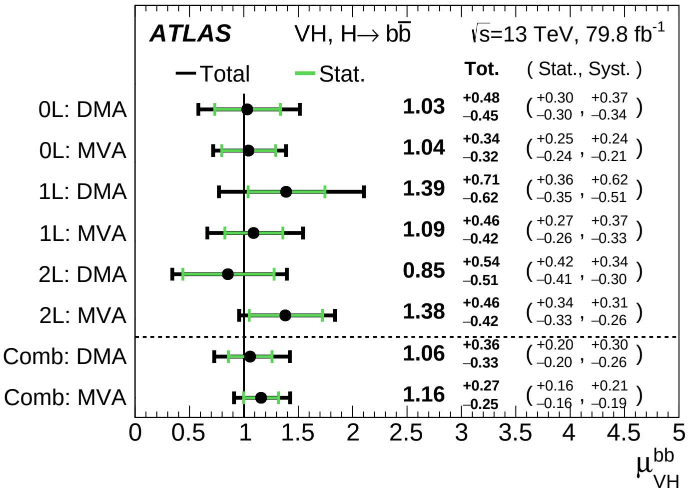

Figure B.6: The fitted values of the Higgs boson signal strength μ^{bb}_{VH} for m_H = 125 GeV for the 0-, 1- and 2-lepton channels and their combination, using the 13 TeV data. The results are shown both for the nominal multivariate analysis (MVA) and for the di-jet mass analysis (DMA). The individual μ^{bb}_{VH} values for the lepton channels are obtained from a simultaneous fit with the signal strength for each of the lepton channels floating independently.

B.3 Results of the diboson analysis

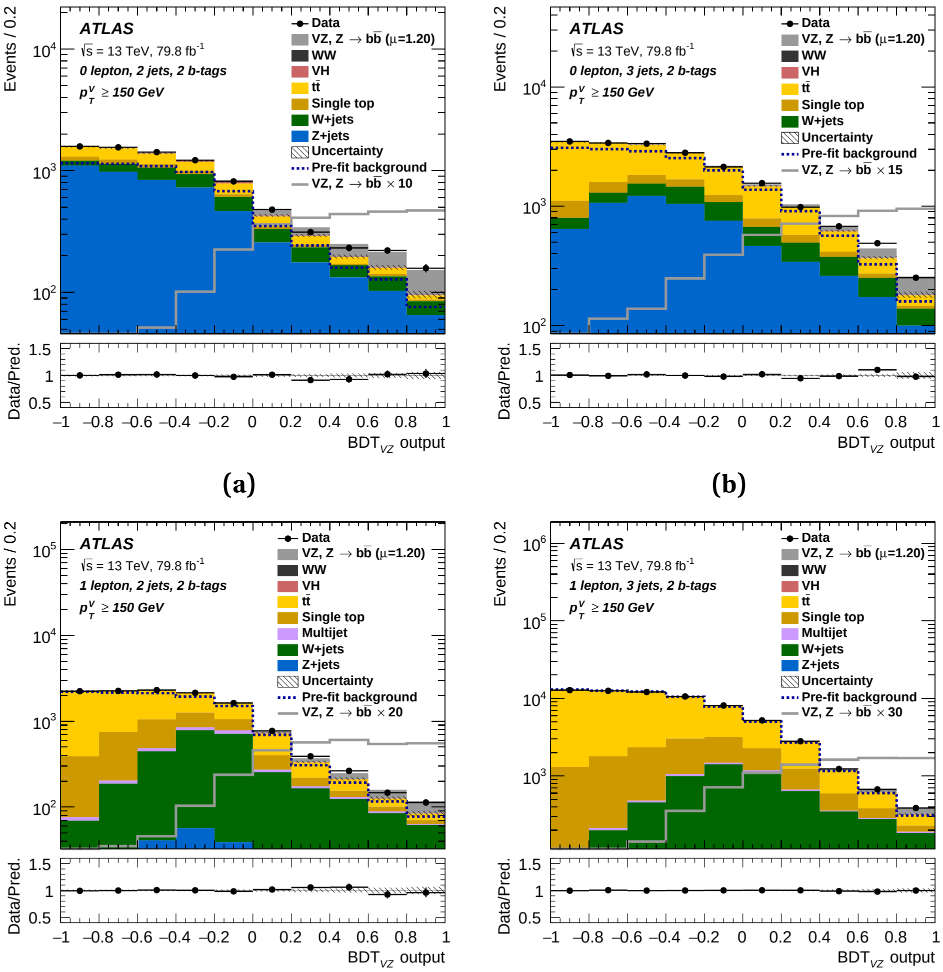

(a) (b)

(c) (d)

Figure B.7: The BDT$_{VZ}$ output post-fit distributions in the 0-lepton (top) and 1-lepton (bottom) channels for 2 b-tag events, for all jet-multiplicity categories and p_{T}^{V} regions used in the fit. Only the distributions in the signal regions are shown. The background contributions after the global likelihood fit are shown as filled histograms. The VZ diboson signal is shown as a filled histogram on top of the fitted backgrounds normalised to the signal yield extracted from data ($\mu = 1.20$), and unstacked as an unfilled histogram, scaled by the factor indicated in the legend. The dashed histogram shows the total pre-fit background. The size of the combined statistical and systematic uncertainty for the sum of the fitted signal and background is indicated by the hatched band. The ratio of the data to the sum of the fitted signal and background is shown in the lower panel.

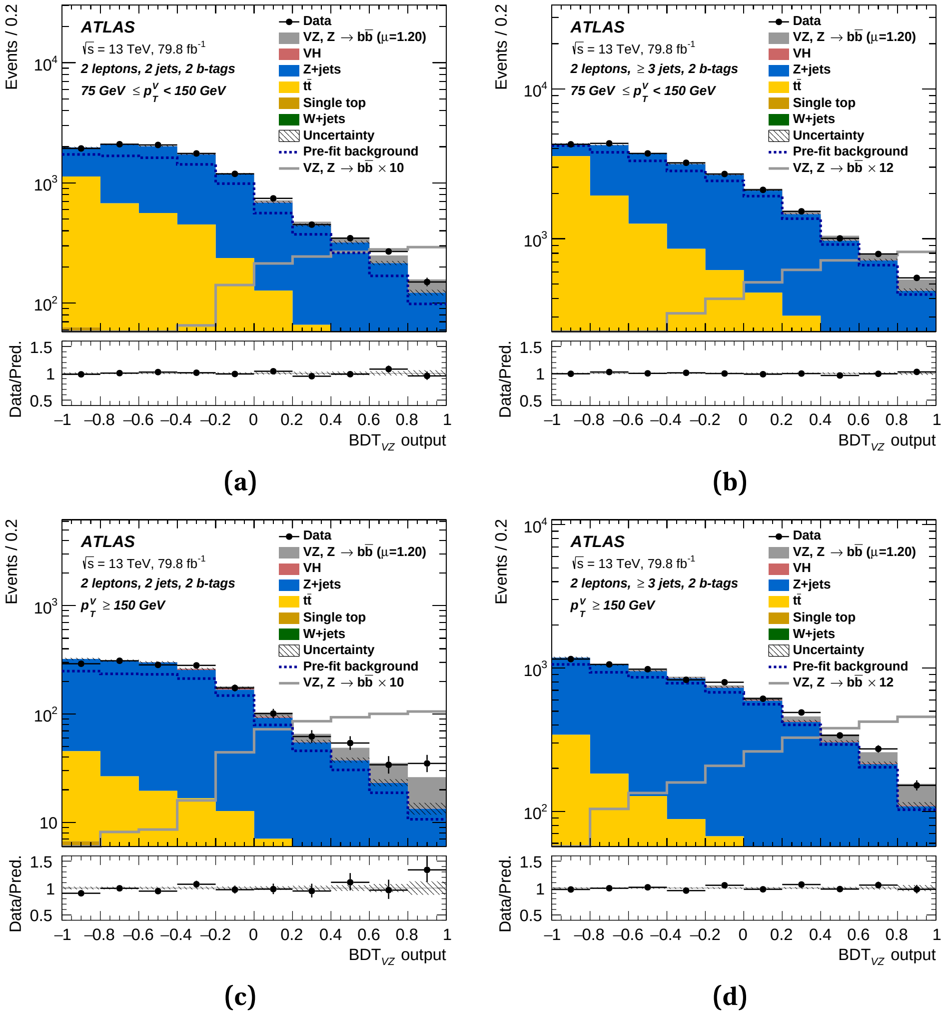

(a)

(b)

(c)

(d)

Figure B.8: The BDT$_{VZ}$ output post-fit distributions in the 2-lepton channel for 2 b-tag events, for all jet-multiplicity categories and p_{T}^{V} regions used in the fit. Only the distributions in the signal regions are shown. The background contributions after the global likelihood fit are shown as filled histograms. The VZ diboson signal is shown as a filled histogram on top of the fitted backgrounds normalised to the signal yield extracted from data ($\mu = 1.20$), and unstacked as an unfilled histogram, scaled by the factor indicated in the legend. The dashed histogram shows the total pre-fit background. The size of the combined statistical and systematic uncertainty for the sum of the fitted signal and background is indicated by the hatched band. The ratio of the data to the sum of the fitted signal and background is shown in the lower panel.

Titre: Le boson de Higgs et la beauté

Mots clés: LHC, ATLAS, Modèle Standard, Boson de Higgs, Production associée, quark b

Résumé: Suite à la découverte du boson de Higgs par les expériences ATLAS et CMS en 2012, un vaste programme de recherche s'est ouvert pour mesurer l'ensemble des propriétés de cette particule. La mise en évidence de son couplage aux quarks b a été un élément majeur du programme de physique du Run-2 du LHC. Ce document d'habilitation retrace l'observation par l'expérience ATLAS de ce couplage ainsi que de la production associée du boson de Higgs avec des bosons de jauge W ou Z (VH). L'analyse du canal VH, $H \rightarrow b\bar{b}$ est présentée, et les différents choix effectués dans l'analyse sont justifiés par des considérations physiques ou expérimentales. Le design général de l'analyse, la sélection des événements, et les études des incertitudes systématiques sont présentés. La délicate analyse statistique de ce processus est détaillée. Le résultat est un excès à 4.9 déviations standard au-dessus des bruits de fond. Les deux observations sont obtenues après combinaison des résultats du canal VH, $H \rightarrow b\bar{b}$ avec ceux d'autres analyses de recherche du boson de Higgs, et les taux d'événements mesurés sont en excellent accord avec les prédictions du modèle standard. Enfin, il est montré comment la mesure de section efficace différentielle du processus VH permet de poser des limites sur de la physique au-delà du modèle standard exprimée dans un Lagrangien effectif.

Title: Beautiful Higgs Boson

Keywords: LHC, ATLAS, Standard Model, Higgs Boson, Associated production, b-quark

Abstract: Following the discovery of the Higgs boson by the ATLAS and CMS experiments in 2012, a wide research program has opened in order to measure all its properties. The observation of its coupling to b-quarks has been a major research topic of the physics programme for the Run-2 of the LHC. This HDR document describes the observation by the ATLAS experiment of this coupling to b-quarks as well as the observation of the associated production of a Higgs boson with a W or Z gauge boson (VH). The analysis of the VH, $H \rightarrow b\bar{b}$ channel is presented, where the choices made on various analysis aspects are justified by physics or experimental considerations. The general design of the analysis, the event selection, the studies on systematic uncertainties are presented. The delicate statistical analysis of this process is discussed in details. The results show an excess of events with a significance of 4.9 standard deviations over the Standard Model backgrounds. The two observations are obtained after combination of the results in the VH, $H \rightarrow b\bar{b}$ channel with those of other Higgs boson searches, and the measured event rates are in excellent agreement with the Standard Model predictions. Finally, it is shown how the differential cross-section measurement of the VH process allows to set limits on beyond the Standard model physics expressed as an effective Lagrangian.

Université Paris-Saclay
Espace Technologique / Immeuble Discovery
Route de l'Orme aux Merisiers RD 128 / 91190 Saint-Aubin, France